INVESTIGATIONS TOWARD POWER RAMP-UP OF FRIB AND INCREASING SCIENTIFIC REACH

By

Alec Gonzalez

A DISSERTATION

Submitted to
Michigan State University
in partial fulfillment of the requirements
for the degree of

Physics — Doctor of Philosophy

2025

ABSTRACT

The Facility for Rare Isotope Beams (FRIB) is a state-of-the-art nuclear physics research facility. FRIB contains two superconducting radiofrequency (SRF) heavy-ion linear accelerators: the FRIB driver linac, and the FRIB Re-Accelerator (ReA). The ultimate purpose of the driver linac is to safely and reliably deliver beams with an unprecedented power of 400 kW to the target. This thesis presents studies that contribute to the goal of achieving this beam power as well as increasing the scientific capabilities of both SRF accelerators at FRIB. These studies include research and development of room-temperature RF cavities, code development, creating new simulation models, updating existing models, and validating with beam measurements.

A critical problem of the power ramp-up process is mitigating beam losses. In the past, the main criterion for a low-loss accelerator was low radio activation of the equipment and the possibility of hands-on maintenance, and the beam loss rate of 1 W/m has been a rule of thumb applicable for room-temperature accelerators up to 1 GeV proton energy. In a superconducting linac, a lost fraction of the beam can significantly degrade crucial components of the accelerator, such as SRF cavities, and more strict requirements for the beam loss rate should be adapted. This thesis explores ways to mitigate losses caused by changes in the calibration of SRF cavities and longitudinal beam halos from the liquid lithium charge stripper. It discusses dual-charge-state acceleration of heavy ion beams in the FRIB radiofrequency quadrupole (RFQ).

Studies presented in the thesis are ways to increase the scientific reach of both the FRIB driver linac and ReA. The design of a chopper system to allow for clean time-of-flight measurements in ReA is discussed. Also explored is the improvement of simulation models for simultaneous multi-charge state beam transport in the FRIB driver linac bending sections

and the beam measurements that validate these models.

The research discussed in this thesis has led to the complete multi-physics design of three room-temperature RF cavities. An application to quickly calculate synchronous phases of SRF cavities has been developed and implemented. Studies of the simulation models of the FRIB driver linac made them more accurate.

ACKNOWLEDGMENTS

I want to thank my advisor Peter Ostroumov for his guidance and pushing me to become a better scientist every day. I would also like to thank my mentor Sasha Plastun for his invaluable advice, discussions, and availability to answer all my questions. I am grateful to all the members of the FRIB accelerator physics department for their openness and willingness to help me in my studies. I have learned so much about how to be a professional accelerator physicist from working with you all every day. Thank you to the faculty in the ASET program, which has provided me unique educational and career opportunities.

Thank you Abby for your constant support and belief in me, it means so much and has given me strength to overcome all the adversities on this long journey. To my family, thank you for your encouragement throughout my whole life, I would not be here without you all.

This material is based upon work supported by the U.S. Department of Energy, Office of Science, Office of Nuclear Physics, and used resources of the FRIB Operations, which is a DOE Office of Science User Facility under Award Number DE-SC0023633 and Office of High Energy Physics, under Award Number DE-SC0018362.

TABLE OF CONTENTS

LIST OF TABLES

LIST OF FIGURES

Chapter 1. Introduction

1.1 Rare Isotope Facilities

1.1.1 Rare Isotope Science

Rare isotopes are short-lived isotopes not naturally found on Earth. Rare isotope science is about finding the different possible combinations of protons and neutrons that the strong force can bind. The study of rare isotopes allows us to better understand the limits of the atomic nucleus and the symmetries of nature. It can be applied to material science and energy studies. It also leads to advances in medical physics through the study of medical isotopes and particle therapy. Particle accelerators are necessary for rare isotope science because the rare isotopes are produced through collisions of other isotopes. As the technology of accelerators has developed and improved greatly over the past few decades, so has the field of rare isotope studies [1].

1.1.2 Facility for Rare Isotope Beams

The Facility for Rare Isotope Beams (FRIB) is a new U.S. Department of Energy (DOE) Office of Science user facility operated by Michigan State University since 2022. FRIB hosts the most powerful heavy-ion accelerator in the world. The beam from the accelerator collides with a fixed target, producing exotic isotopes. The amount of exotic isotopes produced on the target is proportional to the power of the accelerated primary isotope beam. In the last 100 years, about 2000 rare isotopes have been studied worldwide. With FRIB, that number will increase to around 5000 [2].

1.1.2.1 Driver Linac

The FRIB facility contains two superconducting radio-frequency (SRF) linear accelerators. The main accelerator is known as the driver linac, which can accelerate beams of any ion species between oxygen (atomic number Z = 8) and uranium (Z = 92) [3]. The ions of the primary beam are produced by an electron cyclotron resonance (ECR) ion source [4]. The beam is extracted from the source, accelerated to the energy of 12 keV/u, and transported through the low energy beam transport (LEBT) line, which starts above ground, then bends vertically to go into the linac tunnel. The layout of the accelerator in the tunnel is shown in Fig. 1.1.

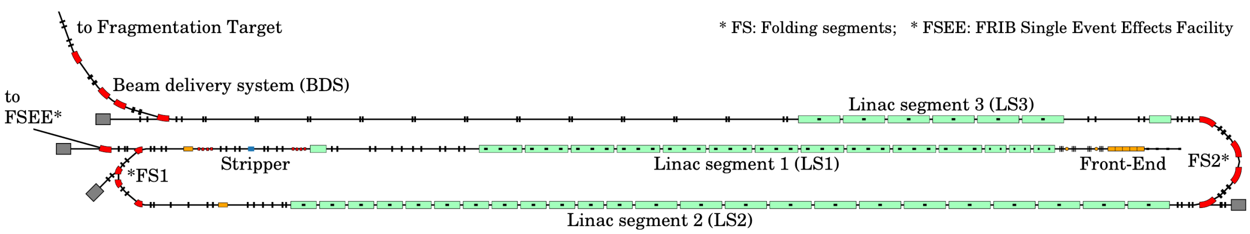

Figure 1.1: Layout of FRIB driver linac.

Once underground, the beam is bunched longitudinally by the multi-harmonic buncher (MHB) [5] then proceeds into the radiofrequency quadrupole (RFQ) [6], which accelerates it to an energy of 0.5 MeV/u. The medium energy beam transfer (MEBT) line is after the RFQ and takes the beam into the entrance of the first superconducting linear accelerating segment, known as LS1. LS1 contains one hundred 80.5 MHz SRF cavities in total. There are 3 cryomodules with four $\beta = 0.041$ quarter-wave resonator (QWR) cavities in each and 11 cryomodules with eight $\beta = 0.085$ QWR cavities in each. After LS1, the beam energy is either 17 or 20 MeV/u depending on the experiment.

Next, the beam passes through a charge stripper, which strips electrons off of the ions in the beam to allow for more efficient acceleration. A carbon foil stripper is used for low intensity beams and a liquid lithium stripper is used for high intensity beams. The stripper is discussed in more detail in Section 1.2.5. After being stripped, the beam passes through Folding Section 1 (FS1). FS1 is a 180-degree achromatic bending section with four 45-degree dipoles. Two multi-gap bunchers (MGBs) keep the beam bunched longitudinally as it passes through FS1 to the entrance of LS2, the second linac segment. All 168 cavities in LS2 are 322 MHz half-wave resonators (HWRs). There are 12 cryomodules each containing six $\beta = 0.29$ HWR cavities and 12 cryomodules each containing eight $\beta = 0.53$ HWR cavities. The average beam energy after LS2 is typically over 150 MeV/u. Next is Folding Segment 2 (FS2), the second achromatic 180-degree bending section. FS2 contains four 45-degree superconducting dipoles to bend the beam to the entrance of LS3, the final linac segment. LS3 is made up by six cryomodules each containing eight 322 MHz $\beta = 0.53$ HWR cavities. The final beam energy is over 200 MeV/u. After LS3, there is space reserved for 644 MHz elliptical cavities as part of a future energy upgrade. Finally, the beam passes through a 70-degree bending section known as the beam delivery system (BDS) consisting of four 17.5-degree dipoles. The BDS takes the beam to the target.

1.1.2.2 Re-Accelerator

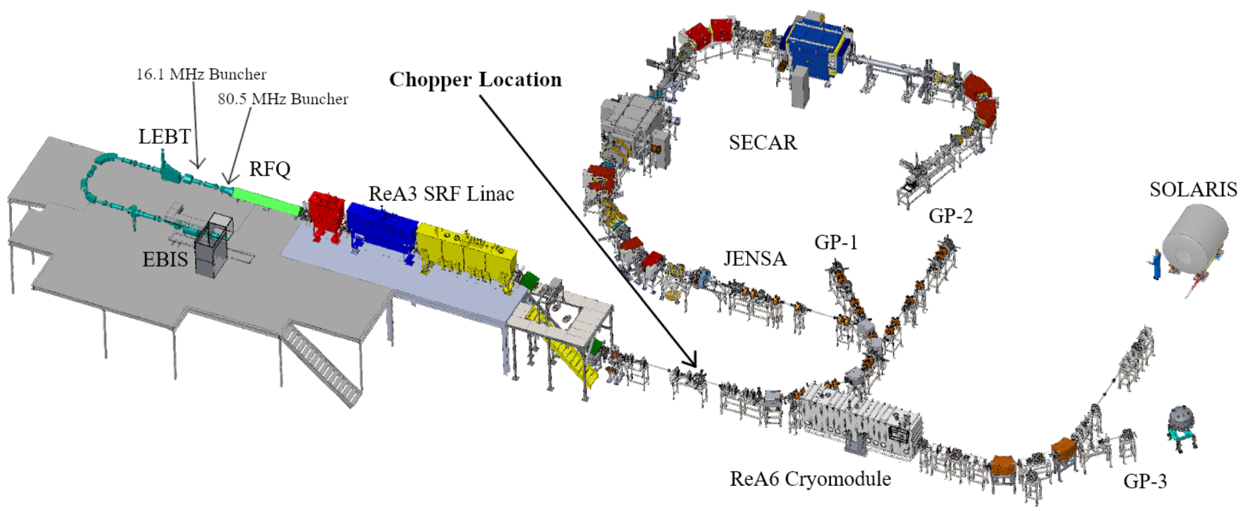

Figure 1.2: Layout of FRIB Re-Accelerator (ReA).

After the primary beam hits the target, the Advanced Rare Isotope Separator (ARIS) removes contaminants to select a beam of the rare isotopes of interest. This isotope beam is sent to the experimental area, which contains multiple beamlines to the experimental stations. One of these destinations is the Re-Accelerator.

The FRIB Re-Accelerator (ReA) is an SRF linac that "re-accelerates" rare isotopes produced in a batch mode ion source or the FRIB high power target [7]. Rare isotopes come into ReA with a charge state of 1+, then the Electron Beam Ion Trap converts them to a charge state acceptable for ReA [8]. ReA can accelerate ions with an A/Q ratio between 2 and 5. As seen in Fig. 1.2, ReA contains a 16.1 MHz and an 80.5 MHz multi-harmonic bunchers upstream of an 80.5 MHz RFQ. The first SRF accelerating segment, ReA3, was commissioned in 2015, and it can accelerate the beam to 3 MeV/u. In 2021, the ReA6 cryomodule was added to accelerate beams to reach an energy of 6 MeV/u. ReA is mainly used for astrophysics experiments and will be discussed in further detail in Chapter 6.

1.2 Accelerator Physics at FRIB

1.2.1 Goals and Challenges

The main goal of FRIB accelerator physics is to safely deliver 400 kW beam to the target. Since the beginning of operation in 2022, we have been slowly ramping up the beam power, with 20 kW being the highest power achieved so far. During this power ramp-up process, the primary challenge is mitigating beam losses. Beam losses can damage important and expensive components of the accelerator like cavities, heat up cryomodules, and produce high radiation, preventing hands-on maintenance. A major part of reducing beam losses is building models that can accurately simulate beam dynamics and allow us to optimally tune the accelerator.

1.2.2 Beam Dynamics

Beam dynamics refers to how charged particles of a beam move in the fields of accelerating and focusing devices. The motion of charged particles is guided by the Lorentz force:

$$\vec{F}_L = q(\vec{E} + \vec{v} \times \vec{B}) \tag{1.1}$$

where q is the charge of the particle, $\vec{E}$ is the electric field experienced by the particle, $\vec{B}$ is the magnetic field experienced by the particle, and $\vec{v}$ is the particle velocity. To accelerate particles, an electric field is necessary. Because the magnetic part of the Lorentz force is proportional to particle velocity, it is more efficient to use magnetic fields to steer and focus particles in a beam although electric fields can also be used at low beam energies. This chapter will describe two categories of beam dynamics: longitudinal dynamics and transverse dynamics.

1.2.2.1 Transverse Beam Dynamics (no acceleration)

Transverse directions refer to the directions perpendicular to the direction of beam propagation, usually written as s or z. Transverse beam dynamics of a particle can be described by a differential equation known as Hill's Equation [9]:

$$x'' + K(s)x = 0 \tag{1.2}$$

In this equation, x is the chosen transverse direction (could be either horizontal or vertical), $x'' = \frac{d^2x}{ds^2}$, and $K(s)$ is the focusing strength. Because Eqn. 1.2 is a linear second-order differential equation, the solutions can be written for x and x' (where $x' = \frac{dx}{ds}$) in the form of a matrix, called the transfer matrix:

$$\begin{bmatrix} x \\ x' \end{bmatrix} = \begin{bmatrix} R_{11} & R_{12} \\ R_{21} & R_{22} \end{bmatrix} \begin{bmatrix} x_0 \\ x'_0 \end{bmatrix} \tag{1.3}$$

where x and x' are the final displacement and divergence and x_0 and x'_0 are the initial values. Common transfer matrices of optical elements are described in Table 1.1 [9].

Table 1.1: Transfer Matrices

Element	2D Transfer Matrix
Drift space of length L	$R = \begin{bmatrix} 1 & L \\ 0 & 1 \end{bmatrix}$
Thin lens quadrupole with focal length $f = \lim_{L \to 2} \left(\frac{1}{KL} \right)$	$R = \begin{bmatrix} 1 & 0 \\ \mp\frac{1}{f} & 1 \end{bmatrix}$
Thick focusing quadrupole with strength K and length L	$R = \begin{bmatrix} \cos\sqrt{K}L & \frac{\sin\sqrt{K}L}{\sqrt{K}} \\ -\sqrt{K}\sin\sqrt{K}L & \cos\sqrt{K}L \end{bmatrix}$
Thick de-focusing quadrupole with strength K and length L	$R = \begin{bmatrix} \cosh\sqrt{\lvert K\rvert}L & \frac{\sinh\sqrt{\lvert K\rvert}L}{\sqrt{\lvert K\rvert}} \\ \sqrt{\lvert K\rvert}\sinh\sqrt{\lvert K\rvert}L & \cosh\sqrt{\lvert K\rvert}L \end{bmatrix}$

When horizontal and vertical motion is coupled, a 4×4 transfer matrix is needed to describe the motion. Equation 1.4 defines the transfer matrix for a solenoid magnet.

$$R = \begin{bmatrix} \cos^2(kL) & \frac{\sin(kL)\cos(kL)}{k} & \sin(kL)\cos(kL) & \frac{\sin^2(kL)}{k} \\ -k\sin(kL)\cos(kL) & \cos^2(kL) & -k\sin^2(kL) & \sin(kL)\cos(kL) \\ -\sin(kL)\cos(kL) & \frac{-\sin^2(kL)}{k} & \cos^2(kL) & \frac{\sin(kL)\cos(kL)}{k} \\ k\sin^2(kL) & -\sin(kL)\cos(kL) & -k\sin(kL)\cos(kL) & \cos^2(kL) \end{bmatrix} \tag{1.4}$$

L is the length of the solenoid and $k = \frac{B}{2(B\rho)}$ where B is the magnetic field strength of the solenoid and $(B\rho)$ is the beam rigidity.

The total transfer matrix through a series of elements can be found by multiplying individual matrices together.

$$R_{tot} = R_N R_{N-1} ... R_0 \tag{1.5}$$

The phase space occupied by the particles of a beam is represented by an ellipse defined by this equation:

$$\gamma x^2 + 2\alpha x x' + \beta x'^2 = \epsilon \tag{1.6}$$

where α, β, and γ are known as Courant-Snyder (CS) parameters [10] (often called Twiss parameters) and $\pi \cdot \epsilon$ is the area of the phase space ellipse, known as the beam emittance. As the beam moves, the particle coordinates change according to the transfer matrices, meaning the CS parameters also change. However, by Liouville's Theorem, the beam emittance stays constant when the beam is affected by linear forces. Because the emittance is constant and x and x' are the only independent variables in Eq. 1.6, only two CS parameters are independent. Therefore, the relation between them is given by:

$$\beta\gamma - \alpha^2 = 1 \tag{1.7}$$

As shown in Fig. 1.3, the CS parameters are related to the beam size by:

$$\begin{aligned} x_{max} &= \sqrt{\beta\epsilon} \\ x'_{max} &= \sqrt{\gamma\epsilon} \end{aligned} \tag{1.8}$$

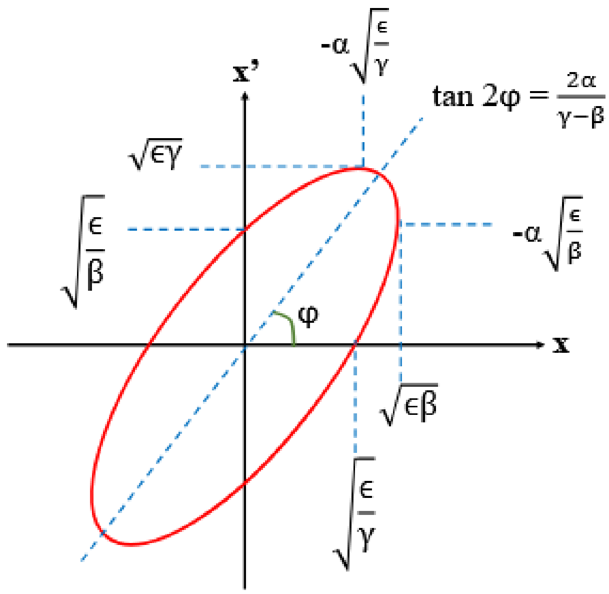

Figure 1.3: Graphical representation of CS parameters [11].

Transfer matrices of CS parameters can be calculated from particle transfer matrices and a σ matrix defined by:

$$\sigma = \epsilon \begin{bmatrix} \beta & -\alpha \\ -\alpha & \gamma \end{bmatrix} \tag{1.9}$$

CS parameters at location 1 are related to the CS parameters at location 0 by:

$$\sigma_1 = R\sigma_0 R^T \tag{1.10}$$

where R is the 2×2 particle transfer matrix from location 0 to location 1. After carrying out the matrix multiplication, Eq. 1.10 can be rewritten to:

$$\begin{bmatrix} \beta_1 \\ \alpha_1 \\ \gamma_1 \end{bmatrix} = \begin{bmatrix} R_{11}^2 & -2R_{11}R_{12} & R_{12}^2 \\ -R_{11}R_{21} & 1 + 2R_{12}R_{21} & -R_{12}R_{22} \\ R_{21}^2 & -2R_{21}R_{22} & R_{22}^2 \end{bmatrix} \begin{bmatrix} \beta_0 \\ \alpha_0 \\ \gamma_0 \end{bmatrix} \tag{1.11}$$

It is easier to use Eqn. 1.11 to track the overall evolution of the beam rather than tracking each individual particle and calculating the CS parameters of the beam at each location. An optical system with symmetry, for example, a periodic lattice, has what is known as a “matched condition”. This refers to specific initial CS parameters that will result in the same CS parameters at the end of the period. If a beam is not matched to the lattice, there will be increased beam size oscillations, leading to a smaller beam size at some locations and a larger beam size at others, which could lead to beam losses in unexpected places along the accelerator. A mismatched beam can also lead to emittance growth due to space-charge and non-linearities.

When the beam is accelerated, Louville’s Theorem is broken, but emittance can still be invariant if it is scaled by the beam energy. For this, a quantity known as normalized emittance is used, which is the geometrical emittance ϵ mulitplied by the relativistic factors $\beta\gamma$.

1.2.2.2 Longitudinal Beam Dynamics

The longitudinal direction refers to the direction of beam propagation through the accelerator. In the FRIB linac, the main devices that contribute to longitudinal beam dynamics are RF cavities. For a reference particle, known as the synchronous particle, the kinetic energy gain of each cavity can be calculated by using Eqn. 1.12:

$$\Delta W = qV_0 T \cos(\phi_s) \tag{1.12}$$

where q is the charge of the particle, V_0 is the voltage of the cavity, and ϕ_s is the synchronous phase of the cavity, which is the phase of the electric field in the cavity seen by the synchronous particle. T is known as the transit time factor (TTF), a factor that takes into account the time variation of the field as a particle travels through an RF gap. The TTF is defined as:

$$T = \frac{\int_{-L/2}^{L/2} E(0,z)\cos(\omega t(z))dz}{\int_{-L/2}^{L/2} E(0,z)dz} - \tan\phi_s \frac{\int_{-L/2}^{L/2} E(0,z)\sin(\omega t(z))dz}{\int_{-L/2}^{L/2} E(0,z)dz} \tag{1.13}$$

where z is the longitudinal coordinate relative to the center of the cavity, $t(z) = \int_0^z \frac{dz}{v(z)}$ with $v(z)$ as the velocity of the beam, and ω is the cavity frequency multiplied by 2π. L is the length of the cavity and $E(0,z)$ is the longitudinal electric field on axis [9].

If the synchronous phase is negative, particles that arrive to the accelerating cavity earlier than the synchronous particle gain less energy and particles that arrive later gain more energy. This ensures stable motion, as all particles oscillate around the synchronous particle in longitudinal phase space, known as synchrotron oscillation. On the other hand, if the synchronous phase is positive, particles that arrive earlier than the synchronous particle gain more energy, and particles that arrive later gain less energy. This motion is unstable, as the particles move further away in phase from the synchronous particle and eventually stop experiencing acceleration. The area of stable motion is called the RF bucket or the longitudinal acceptance and it is defined by the separatrix. Figure 1.4 shows the separatrix and some longitudinal phase space trajectories when ϕ_s is some number between 0° and -90°. The size of the bucket is maximum at $\phi_s = -90°$ [9], which is depicted in Fig. 1.5. In this case, over many phase space oscillations, the synchronous particle experiences no acceleration according to Eqn. 1.12.

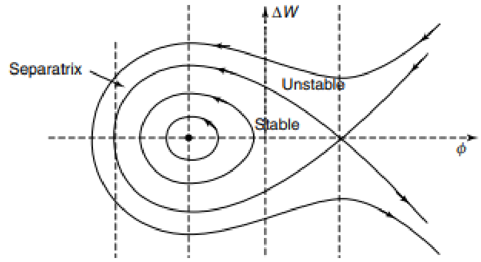

Figure 1.4: Example of longitudinal phase space trajectories when ϕ_s is between 0° and -90° [9].

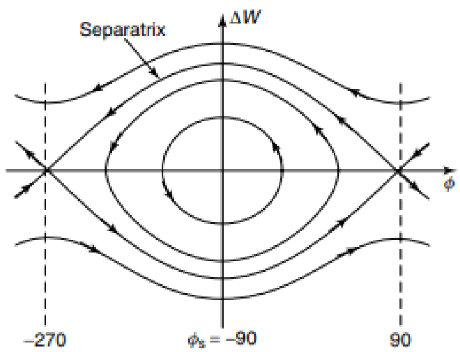

Figure 1.5: Longitudinal phase space trajectories when $\phi_s = -90°$ [9].

For small oscillations inside the separatrix, the beam can be described as an ellipse in longitudinal phase space. The beam can be represented by CS parameters in longitudinal phase space, similar to transverse dynamics. It is important to match the longitudinal CS parameters of the beam to the CS parameters of the accelerating segments to prevent large oscillations in longitudinal beam size due to mismatch and longitudinal emittance growth due to non-linearities. Longitudinal beam dynamics in the FRIB linear accelerator are discussed in detail in Chapter 2.

1.2.3 Simulation Codes

In the projects described in this thesis, two main codes are used to simulate beam dynamics. The first is known as TRACK [12]. TRACK is a three-dimensional particle tracking code. It accepts 3D field maps for any element of the accelerator and tracks a given number of macroparticles through these elements. For intense beams, TRACK can calculate 2D or 3D space charge forces. The second code is called FLAME (Fast Linear Accelerator Model Engine) [13]. FLAME is a high-speed envelope tracking code developed for the FRIB linear accelerator. FLAME works by tracking the beam centroid and CS parameters using transfer matrices. Therefore, FLAME is much faster than TRACK. For this reason, FLAME is commonly used for optimization problems, such as the development of tunes for the FRIB linac. While FLAME is a linear first-order accelerator optics code that supports multi-charge-state transport calculation, to include high-order effects and simulate beam losses, we use the macroparticle TRACK code.

1.2.4 Physics of Multiple Charge State Beams

Charge stripping is essential for efficient acceleration of heavy-ion beams. When a heavy-ion beam is stripped, the resulting charge distribution is a Gaussian function centered on the mean charge state. The mean and standard deviation of this Gaussian depends on many factors like beam velocity, atomic mass of ions in the beam, stripper material and stripper thickness. However, stripping of a 17 MeV/u uranium beam with the liquid lithium stripper produces a mean charge state of 75+ with just 21% of initial beam intensity in the charge state 75+. Therefore, the post-stripper segments of the FRIB driver linac were designed to accept and simultaneously accelerate multiple charge states and deliver them to the target. For example, a year-and-a-half ago, three charge states of the stripped uranium beam were accelerated and delivered a record power of 10.4 kW to the isotope production target [14]. In March 2025, we developed the linac tune to produce 20 kW of uranium beam on the target by accelerating five charge states after the stripper.

1.2.4.1 Transport Through Bending Sections

Each charge state exits the stripper with almost equal average energy. In FS1, the beam is bent 180 degrees in the horizontal direction by four 45-degree dipoles. In a given magnetic field, the bending radius of a particle depends on its rigidity, which is defined as:

$$(B\rho) = \frac{p}{q} \tag{1.14}$$

where p is the momentum of the particle and q is the particle's charge. In a multi-charge-state beam, each charge state has a different rigidity, thus they have a different bending radius and path length through a dipole magnet. The equation of motion for the horizontal direction in a dipole magnet is:

$$x'' + K(s)x = \frac{\delta}{\rho(s)} \tag{1.15}$$

where $\rho(s)$ is the bend radius and $\delta = \frac{\Delta p}{p} = \frac{-\Delta q}{q}$ [15]. The solution to Eqn. 1.15 can be split into two parts, a general solution that solves Eqn. 1.2, and a particular solution, corresponding to:

$$x_p(s) = \delta \cdot D(s) \tag{1.16}$$

$$D''(s) + K(s)D(s) = \frac{1}{\rho(s)} \tag{1.17}$$

where D is the dispersion function. Equation 1.16 corresponds to the offset in the horizontal direction compared to the design trajectory. The solution to Eqn. 1.17 can be written as a

3×3 transfer matrix.

$$\begin{bmatrix} D_1 \\ D'_1 \\ 1 \end{bmatrix} = M_3 \begin{bmatrix} D_0 \\ D'_0 \\ 1 \end{bmatrix} \tag{1.18}$$

For a dipole bend with horizontal focusing, bending angle θ and bending radius ρ, the M_3 matrix can be written as:

$$M_3 = \begin{bmatrix} \cos\theta & \rho\sin\theta & \rho(1-\cos\theta) \\ \frac{-\sin\theta}{\rho} & \cos\theta & \sin\theta \\ 0 & 0 & 1 \end{bmatrix} \tag{1.19}$$

For non-dispersive elements described in Table 1.1, the M_3 matrix can be written as:

$$M_3 = \begin{bmatrix} R_{11} & R_{12} & 0 \\ R_{21} & R_{22} & 0 \\ 0 & 0 & 1 \end{bmatrix} \tag{1.20}$$

where R is the 2×2 transfer matrix of the corresponding element in Table 1.1.

The FRIB bending sections are designed to be achromatic, meaning at the beginning and end of each bending section $D = 0$ and $D' = 0$. The dispersion function in Folding Segment 1 (FS1), the first bending section, is shown in Fig. 1.6.

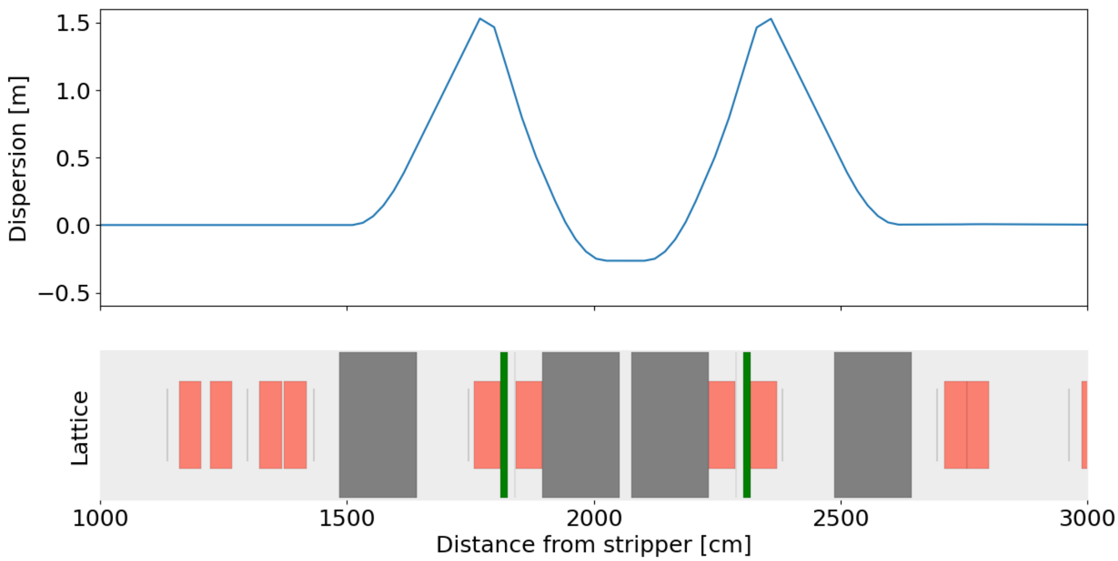

Figure 1.6: Dispersion function in FS1 of the FRIB linac calculated by FLAME. Thick grey boxes correspond to dipoles, red boxes are quadrupoles, green boxes are sextupoles.

For a multi-charge-state beam, we want each charge state to have the same transverse phase-space configuration at the output of the bending section as they do at the input of the bending section. Therefore, the bending sections need to be second-order achromatic to cancel out the non-linear aberrations caused by the difference in charge. Motion through the bending section can be represented with a 6×6 transfer matrix R and particle coordinates $\vec{X}(x, x', y, y', l, \delta)$, where l is the particle's longitudinal position with respect to the reference particle. The coordinates evolve by:

$$X(1)_i = \sum_i R_{ij} X_j(0) \tag{1.21}$$

For the second order, the second-order matrix T is introduced, and the coordinates evolve by:

$$X(1)_i = \sum_i R_{ij} X_j(0) + \sum_{j,k} T_{ijk} X_j(0) X_k(0) \tag{1.22}$$

Due to symmetry of the bending section and settings of the quadrupoles in the bending section, $R_{51} = R_{52} = R_{53} = R_{54} = R_{56} = 0$. This means the path length of a particle through the bending section in the first order does not depend on the charge state. This is known as the isopath condition. Because of second-order effects depending on the difference in charge, each charge state arrives at a different location in horizontal and longitudinal phase space at the end of the bending section. This essentially means the effective emittance of the multi-charge state beam has increased. To cancel this effect in the horizontal plane, sextupole magnets are used with fields set to make $T_{166} = T_{266} = 0$. As shown in the top plot of Fig. 1.7, for a five charge state uranium beam, the horizontal centroids separate by $\pm$ 25 mm in the FS1 bending section, then are recombined to less than $\pm$ 0.5 mm of separation after the bend. The sextupoles are also used to reduce T_{566} which is proportional to $\left(\frac{\Delta q}{q}\right)^2$ and affects the arrival time of different charge states compared to the reference. Even though this term is not zero, this difference in arrival time can be reduced at the entrance to the next accelerating section by using rebuncher cavities, as shown in the longitudinal centroid plot in Fig. 1.7. Trajectories and envelopes of multi-charge state beams in FS1 are discussed in more detail in Chapter 3.

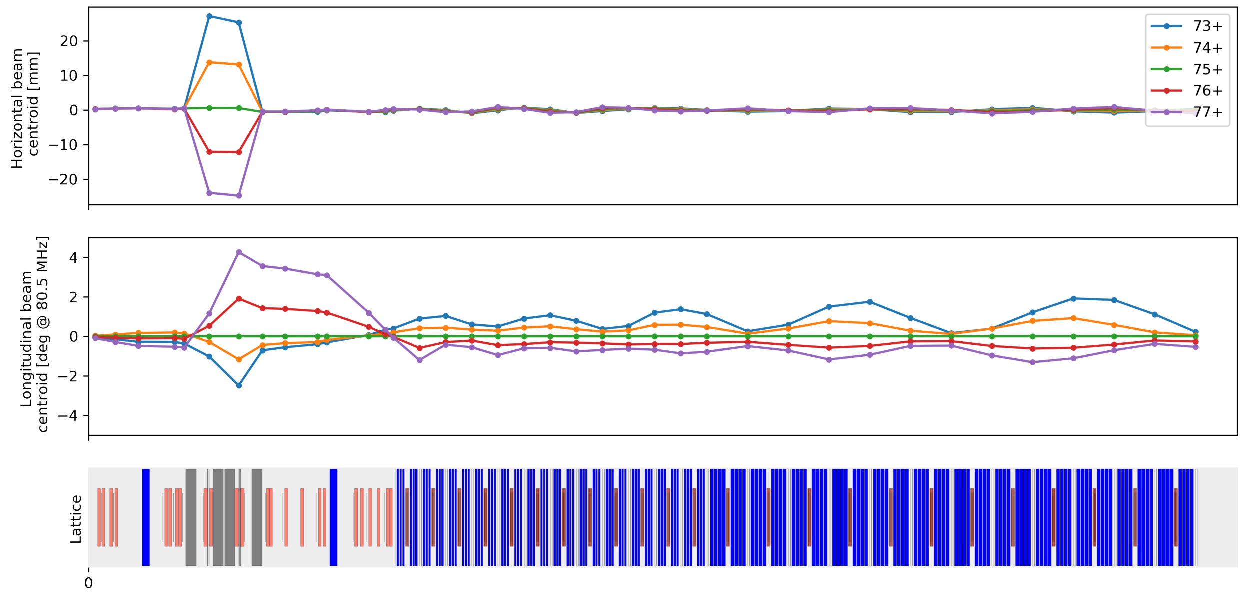

Figure 1.7: Measured horizontal and longitudinal centroid trajectories of a five charge state uranium beam from the stripper to the end of LS2 (blue boxes represent RF cavities).

1.2.4.2 Acceleration of Multiple Charge States

The accelerating segments of the FRIB linac are designed to accelerate multiple charge states simultaneously. Each charge state q_i can have the same velocity profile across the linac, if this condition is met [16]:

$$\left(\frac{q_i}{A}\right)\cos\phi_{s,i} = \left(\frac{q_0}{A}\right)\cos\phi_{s,0} \tag{1.23}$$

where A is the mass of the beam, q_0 is the reference charge state, and $\phi_{s,0}$ is the synchronous phase of the reference charge state. The synchronous phase of each charge state $\phi_{s,i}$ can be calculated by rearranging Eqn. 1.23 into:

$$\phi_{s,i} = -\arccos\left(\frac{q_0}{q_i}\cos\phi_{s,0}\right) \tag{1.24}$$

The second rebuncher cavity in FS1 (MGB02) changes the phase mismatch produced in FS1 to the energy plane for LS2 injection. As seen in Fig. 1.7, for a five charge state uranium beam, in LS2, the other charge states oscillate near the central charge state with an amplitude of up to $\pm$ 2 degrees. The accelerating cavities are phased to maximize the acceptance of all charge states.

1.2.5 Charge Stripper

A charge stripper is necessary for more efficient acceleration. In the FRIB linac, the charge stripper is located after the first accelerating section (LS1), where the beam energy is between 16.5 and 20.0 MeV/u. There are two options for charge stripping at FRIB. For low-intensity beams, a traditional carbon foil stripper is used. However, the carbon foil is damaged at high power densities, which means a different type of stripper is needed for high-intensity beams, which are the majority of the beams. In this case, a unique liquid lithium stripper is used, the first in the world of this kind [17]. As shown in Fig. 1.8, the nozzle shoots a jet of liquid lithium at the deflector, producing a thin film for the beam to pass through.

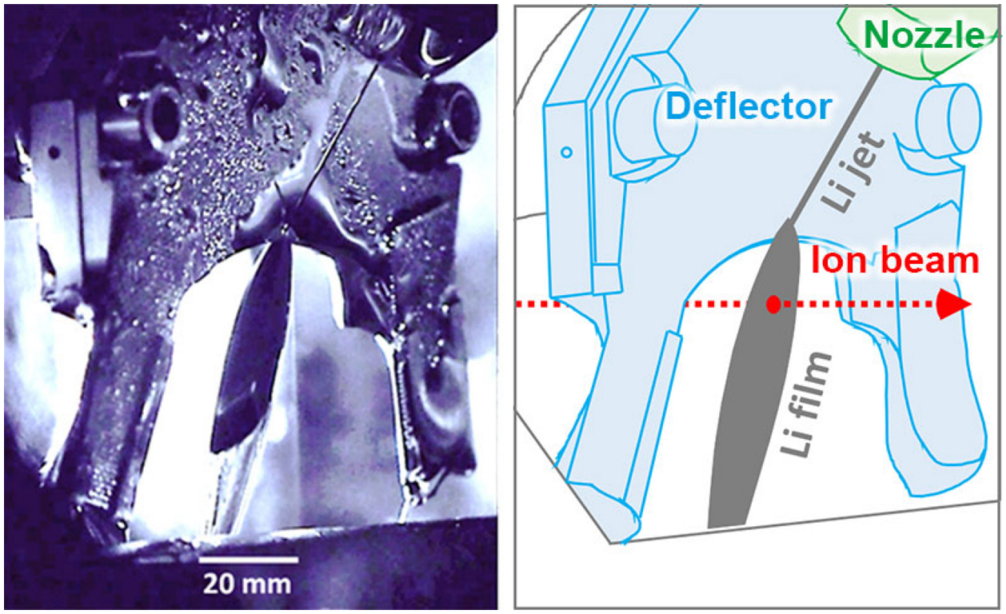

Figure 1.8: Liquid lithium charge stripper photo (left) and diagram (right) [18].

While traveling through the stripper, the transverse phase space of the beam is affected by scattering and the longitudinal phase space is affected by energy loss and straggling.

Scattering is when the angle of a beam particle's trajectory changes due to Coulomb interactions between the particle and the lithium atoms in the stripper. The deflection depends on the number of nuclei per unit volume (N) and thickness (x) of the stripper, the charge (z), momentum (p), and velocity (v) of the beam particles, the charge of the stripper atoms (Z), the elementary charge (e), and the impact parameter (b), which is defined as the perpendicular distance between the initial trajectory path and the center of the nucleus of the lithium atom the beam is approaching. The mean square deflection angle Θ of a particle is defined by:

$$\left\langle \Theta^2 \right\rangle = \frac{8\pi N x Z^2 z^2 e^4}{v^2 p^2} \log\left(\frac{b_{max}}{b_{min}}\right) \tag{1.25}$$

with:

$$
\begin{aligned}
b_{max} &= \frac{a_0}{Z^{\frac{1}{3}}} \\
b_{min} &= \frac{2Zze^2}{vp}
\end{aligned}
\tag{1.26}
$$

where a_0 is the Bohr radius [19].

The beam particles lose energy due to collisions with electrons in the stripper. The average energy loss dE per path length dx is calculated by the Bethe formula:

$$
-\left\langle \frac{dE}{dx} \right\rangle = \frac{4\pi z^2 e^4 n}{mv^2} \left(\log\left[\frac{2mv^2}{I(1-\beta^2)} \right] - \beta^2 \right) \tag{1.27}
$$

where I is the mean excitation energy of the stripper which is approximately proportional to Z, and n is the electron number density of the stripper.

The statistical variation in energy loss is known as straggling. To calculate mean square difference in energy loss through a finite thickness x, let E_0 represent the average energy loss and E represent the energy loss of a specific particle, then:

$$
\left\langle (E - E_0)^2 \right\rangle \approx 4\pi z^2 e^4 NZx \tag{1.28}
$$

The energy loss distribution of a beam has a cutoff at a minimum energy loss and a long tail with values higher than the average energy loss. This is due to the Coulomb scattering of beam particles on the stripper nuclei [20]. This is shown in the plot in Fig. 1.9. Some of the particles in the tail may not be contained within the longitudinal acceptance of the post-stripper part of the accelerator.

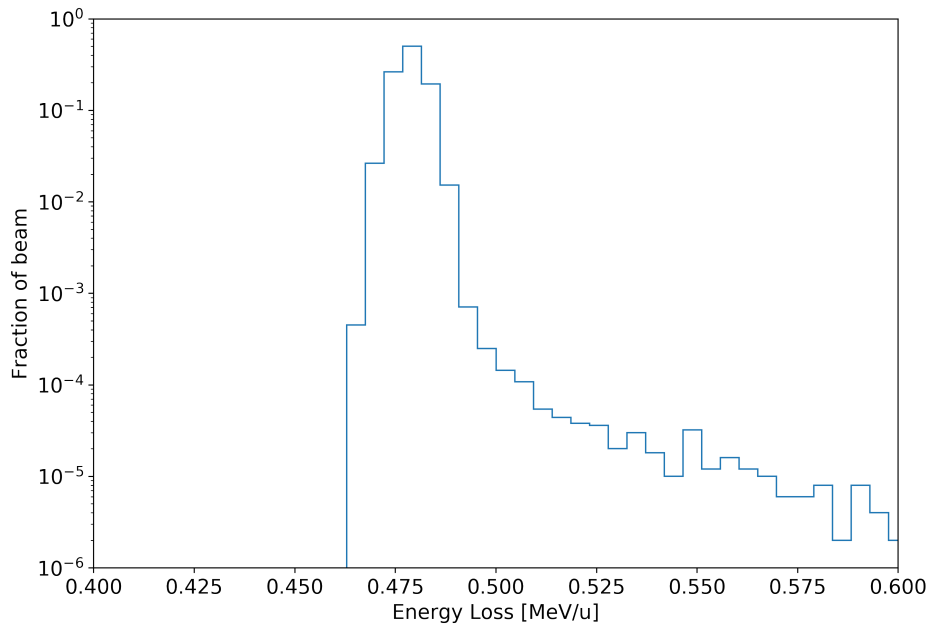

Figure 1.9: Energy loss distribution of 17 MeV/u uranium beam stripped in liquid lithium film with uniform thickness simulated by SRIM.

A code called SRIM [21], which stands for Stopping and Range of Ions in Matter, is used to simulate energy loss, straggling and scattering effects of the stripper. Particle distribution through LS1 up to the location of the stripper is simulated using TRACK then that distribution is imported into SRIM. In SRIM, the materials and thickness of a target for the input particles to pass through can be customized. The code uses semi-empirical models to calculate the effects of the target on the input particles and creates an output distribution. Then this output distribution is exported and used in TRACK simulations of the post-stripper part of the accelerator. Figure 1.10 shows the results of SRIM simulations of different 17 MeV/u beams going through the lithium stripper of different thicknesses. It shows a correlation between output energies and scattering angle following the Coulomb scattering kinematics. Particles in these tails are lost on the designated collimators in the post-stripper sections of the accelerator.

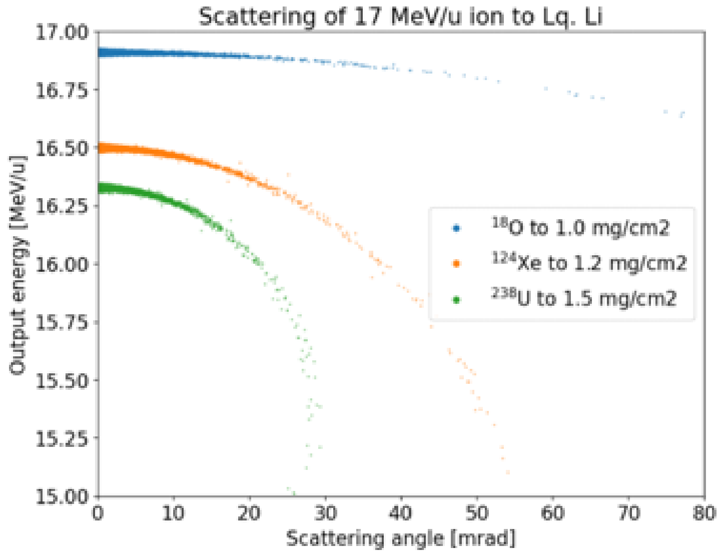

Figure 1.10: Simulation of scattering angle versus output energy for different 17.0 MeV/u beams passing through different thicknesses of the lithium stripper.

The FRIB lithium stripper has inherent non-uniformities in the thickness of the film, as seen in Fig. 1.11, which shows the measured thickness distribution. Even in a small beam spot area, these non-uniformities are present. The area at the top of the plot with the highest thickness is closest to the nozzle. The thickness variation in the horizontal direction can be modeled with a Gaussian function, and the vertical direction can be modeled with an exponential function. The beam energy loss measurements show that the lithium film has several equilibrium states, resulting in a thickness change of up to $\pm$ 20%. Consequently, the average beam energy and beam halo fluctuate over time.

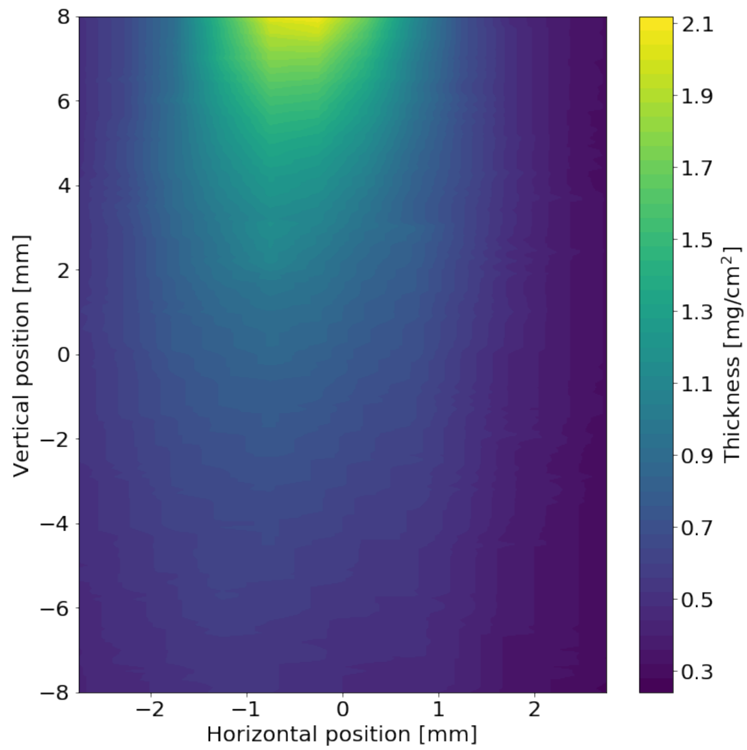

Figure 1.11: Measured FRIB liquid lithium stripper film thickness distribution.

These non-uniformities cause extra variation in the energy spread and scattering angle of the beam after passing through the stripper. This can lead to increased beam losses in the post-stripper part of the accelerator, which will be discussed in Chapter 4.

Chapter 2. Longitudinal Beam Dynamics in the FRIB Linac

2.1 Forming of Small Longitudinal Emittance

2.1.1 Multi-Harmonic Buncher

The beam leaves the ECR ion source as a dc beam with an energy of 12 keV/u. It is accelerated by an 80.5 MHz RFQ to 500 keV/u before injection into the first linac section. A cavity known as the Multi-Harmonic Buncher (MHB) is located upstream of the RFQ. The purpose of the MHB is to produce small longitudinal emittance, bunch the beam, and match the beam to the RFQ acceptance [22]. The MHB is a single gap cavity with three harmonics, 40.25 MHz, 80.5 MHz, and 120.75 MHz. The amplitudes of the harmonics are tuned to achieve maximum beam transmission through the RFQ. The longitudinal phase space of the beam and the RFQ acceptance produced by TRACK simulations are shown in Fig. 2.1.

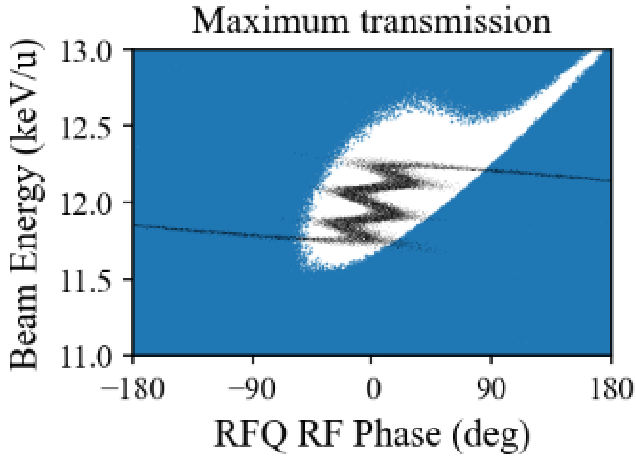

Figure 2.1: TRACK simulated RFQ acceptance and longitudinal beam profile when MHB is tuned for maximum transmission [22].

2.1.2 RFQ

Radio Frequency Quadrupoles (RFQs) are used to bunch and accelerate low-energy ion beams. Adiabatic bunching is typically over about 2/3 of the RFQ length, but the the FRIB RFQ was made much shorter by using an MHB that produces significantly smaller longitudinal emittance than achievable with adiabatic bunching. Minimization of longitudinal emittance was a design goal of the FRIB RFQ. The initial synchronous phase is -35 degrees [23], which is different from the conventional RFQ initial synchronous phase of -90 degrees. This means the FRIB RFQ also has a smaller longitudinal acceptance. Therefore, as seen in Fig. 2.1, the particles in the tails of the bunch are not accepted by the RFQ, leading to a small output longitudinal emittance. According to the same simulations as Fig. 2.1, the normalized rms longitudinal emittance after the RFQ is 0.14 π·ns·keV/u.

2.2 Instant Phase Setting

Instant Phase Setting (IPS) is a code developed at FRIB [24] that simulates longitudinal particle motion using one-dimensional numerical integration. The user inputs a lattice file with positions of cavities and BPMs and a velocity profile containing synchronous phases and field settings of the cavities. IPS simulates the phase trajectory and energy gain of a particle through the lattice by solving this system of differential equations:

$$\frac{dW}{dz} = qE_z(z,t) \tag{2.1}$$

$$\frac{dt}{dz} = \frac{1}{v_z} \tag{2.2}$$

W is the kinetic energy of the particle, q is the charge of the particle, $E_z(z,t)$ is the longitudinal component of the electric field inside the accelerator at time t and position z, and v_z is the longitudinal velocity of the particle. Longitudinal velocity is related to kinetic energy by:

$$v_z = c\frac{\sqrt{(1+\frac{W}{mc^2})^2 - 1}}{1+\frac{W}{mc^2}} \tag{2.3}$$

where c is the speed of light and m is the mass of the particle.

The electric field inside a cavity is modeled as:

$$E_z(z,t) = K \cdot A \cdot E_z(z) \cos\left(\omega t + \Delta\phi + \phi_{cavity}\right) \tag{2.4}$$

The field distribution $E_z(z)$ comes from a CST Studio simulation, K is a field scaling coefficient, and A is the field setpoint. The angular frequency of the cavity is ω, the driven phase of the cavity is ϕ_{cavity}, and $\Delta\phi$ is the total phase offset relative to the RF reference line. For FRIB cavities, the phase offset and field scaling coefficient are calculated by fitting the results of IPS simulations to phase scan measurements, this is known as the RF calibration procedure.

The main purpose of IPS is to reduce longitudinal beam tuning time by quickly calculating cavity driven phases based on a given velocity profile. Before IPS, we established cavity phases by performing phase scan measurements ("manual phasing") on all 328 cavities in the accelerator every time a different beam is set up. This takes about 24 hours for each beam. With IPS, the first 12-16 cavities are manually phased then IPS is used to set the phases of the rest, which takes about 30 minutes total. Figure 2.2 shows the IPS GUI used while tuning the accelerator. IPS is a massive time-saver in the beam-tuning process.

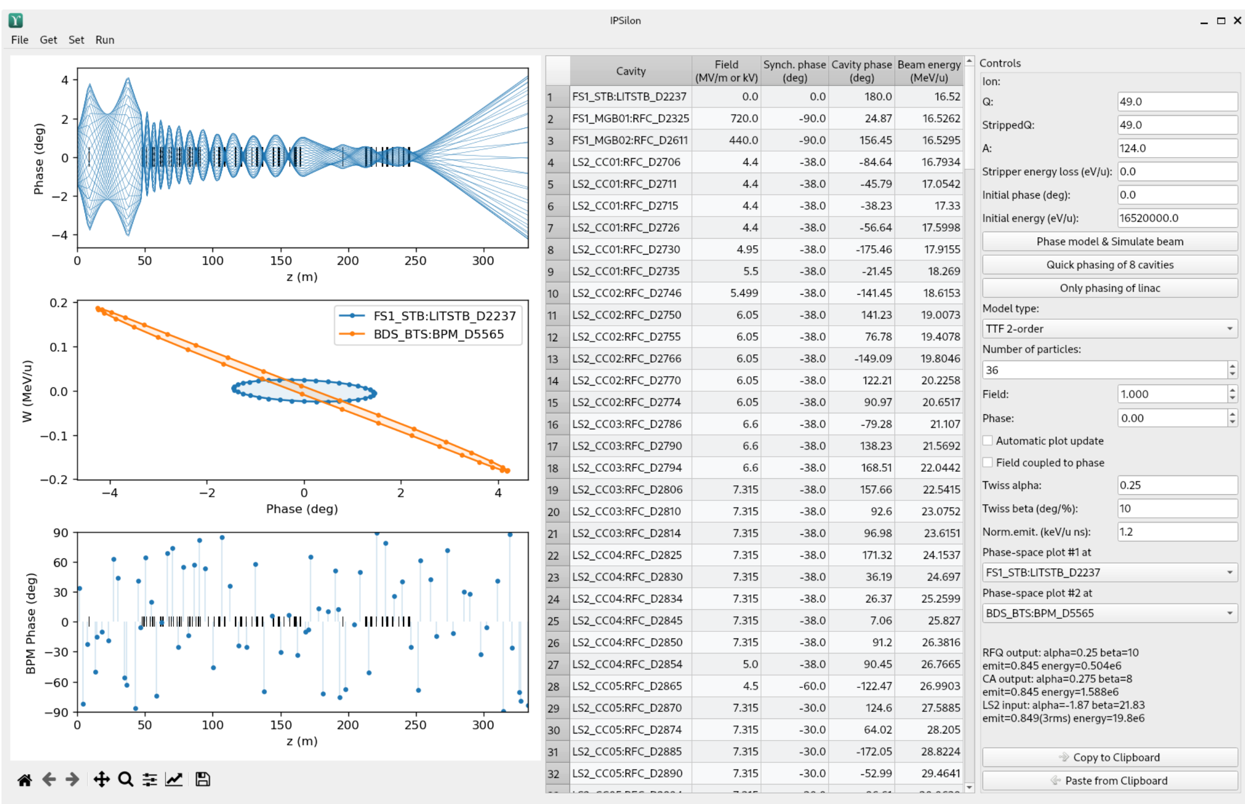

Figure 2.2: IPS graphical user interface (GUI).

2.3 Debugging RF Calibration

To produce accurate simulations, IPS relies on accurate phase offset and field scaling coefficients. If the phase offset of a cavity suddenly changes from something like a cable connector coming loose, IPS will provide inaccurate results, and the cavities will not be phased correctly. A way to identify RF calibration changes was needed so IPS can be updated.

First, we checked if IPS can accurately simulate BPM phase measurements when a cavity phase is changed. Next, the BPMs response from various cavities were investigated. Some BPMs in LS1 have 3 cavities in between them and we also wanted to check if the BPM phase response would be different depending on which of the three cavities had its phase changed. For this study, a $^{40}Ar^{11+}$ beam was accelerated to 20 MeV/u in LS1. The phase of one cavity was changed by 10 degrees and BPM results were saved, then the cavity phase was changed back and the phase of the cavity next to it was changed by the same amount and the results were saved. The results were compared to the reference BPM phases and then compared to IPS simulations, shown in Fig. 2.3.

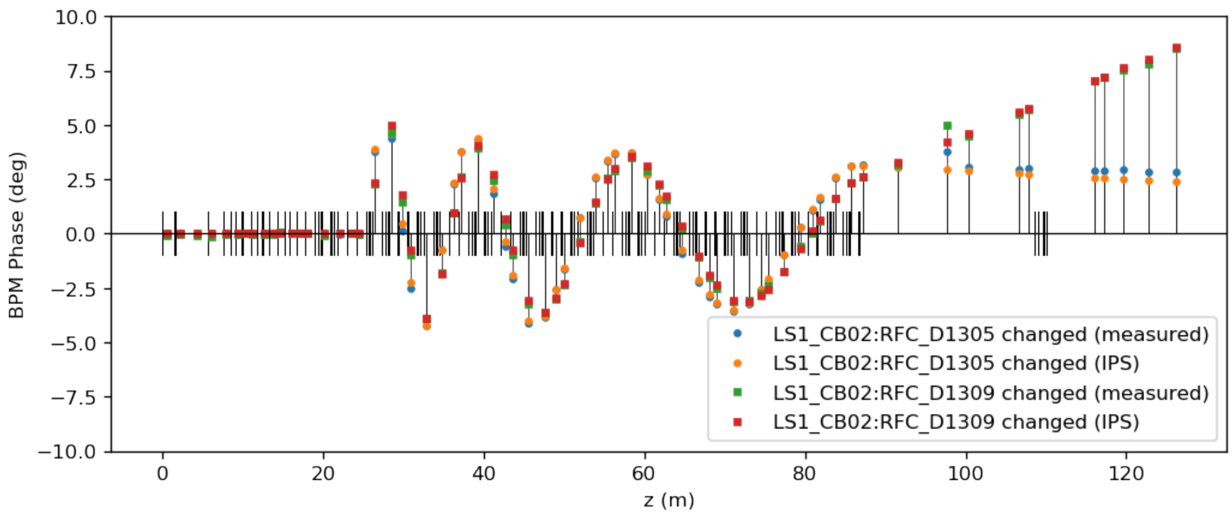

Figure 2.3: BPM phase response when the phases of two cavities in the fifth LS1 cryomodule are changed by 10 degrees. Black bars are SRF cavities.

It is clear from Fig. 2.3 that IPS simulations match measured BPM data when a cavity's phase is changed. There is a different pattern in the BPM phase response for the different cavities (circles and squares in the plot). Therefore, it is possible to use BPM phase response to identify phase changes in cavities.

2.3.1 Development of Application to Evaluate Synchronous Phases

To quickly verify the synchronous phase of a cavity, a Python-based application was developed. The application uses BPM phase response to the cavity driven phase changes to calculate the synchronous phase of the cavity. The application can perform this task in as little as one minute per cavity which is three to five times faster than the "manual" phasing procedure.

The application works first by having the user select the cavity or cavities to scan, the number of BPMs to use for the calculation and the step length in degrees for the phase scan. It will then save the initial BPM phases and begin the phase scan, saving BPM phases at each step. The phase scan will stop once the BPM phases are equal or close to equal to the initial BPM phases, which means the energy gain of the cavity at the new phase is similar to the energy gain at the initially set driven phase. As seen in Eqn. 1.12, the energy gain depends on $\cos(\phi_s)$, so it should be equal at ϕ_s and $-\phi_s$ as shown in Fig. 2.4.

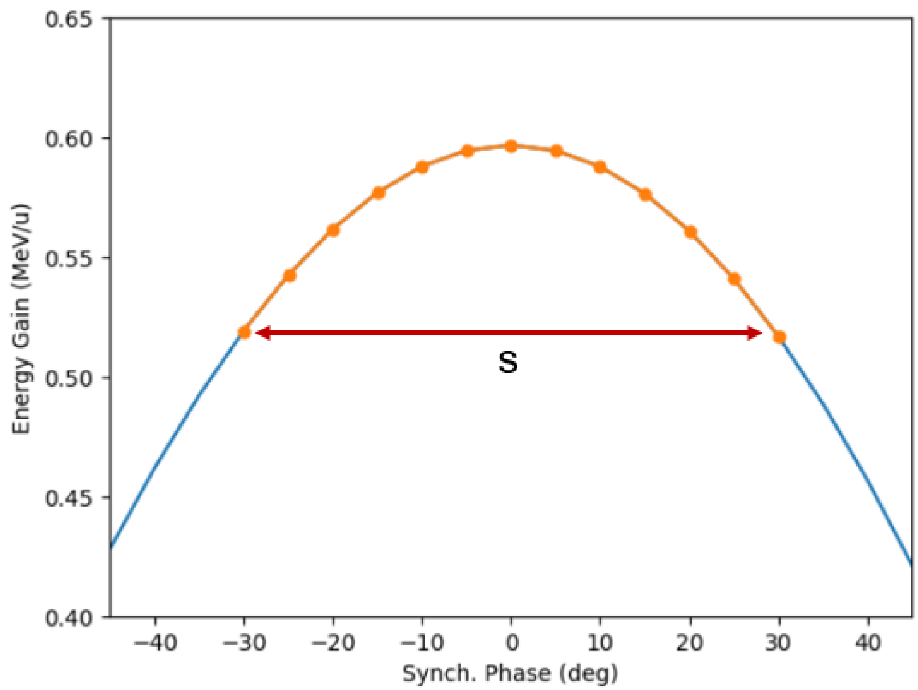

Figure 2.4: Synchronous phase versus energy gain for a single cavity.

The basic principle of the application is to change the cavity phase until the initial energy gain is matched. The distance between the initial cavity phase and the new phase with equivalent energy gain is represented by s in Fig. 2.4. Once s is found, the synchronous phase of the cavity can be calculated using:

$$\phi_s = -\frac{1}{2}s \tag{2.5}$$

While energy gain depends on $\cos\phi_s$, longitudinal focusing depends on $\sin\phi_s$, so changing a cavity's synchronous phase to positive leads to that cavity having a de-bunching effect on the beam. Before proceeding with development of the application, IPS simulations were used to check how changing the synchronous phase of different cavities along the accelerator affects the longitudinal envelope of the beam. Figures 2.5 to 2.8 show four results from this study, where the design synchronous phase of the given cavity was changed from negative to positive.

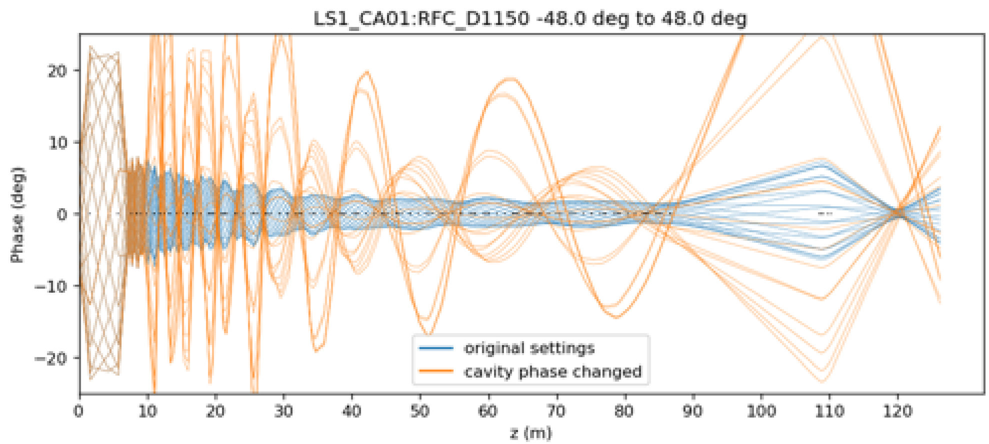

Figure 2.5: IPS simulated longitudinal beam envelopes in LS1 of design tune and when a cavity phase in the first cryomodule is changed by 96 degrees. Beam energy at this cavity is 0.7 MeV/u.

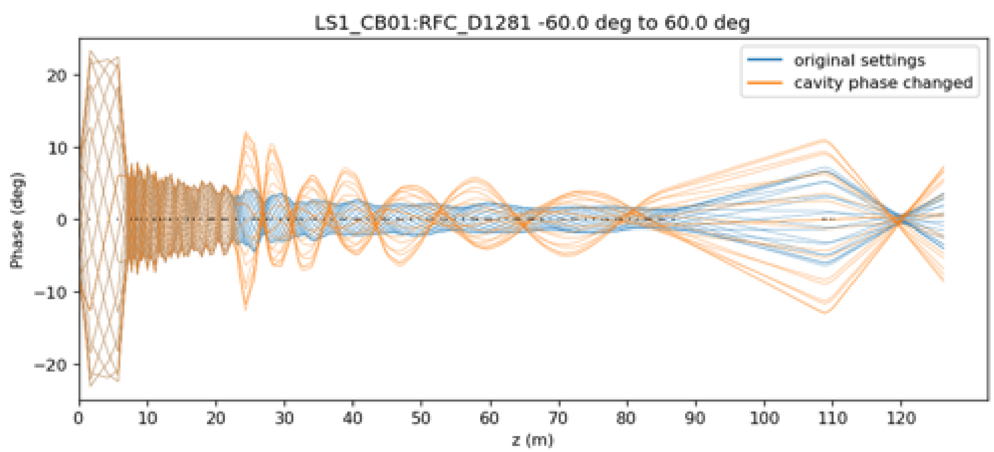

Figure 2.6: IPS simulated longitudinal beam envelopes in LS1 of design tune and when a cavity phase in the fourth cryomodule is changed by 120 degrees. Beam energy at this cavity is 2.5 MeV/u.

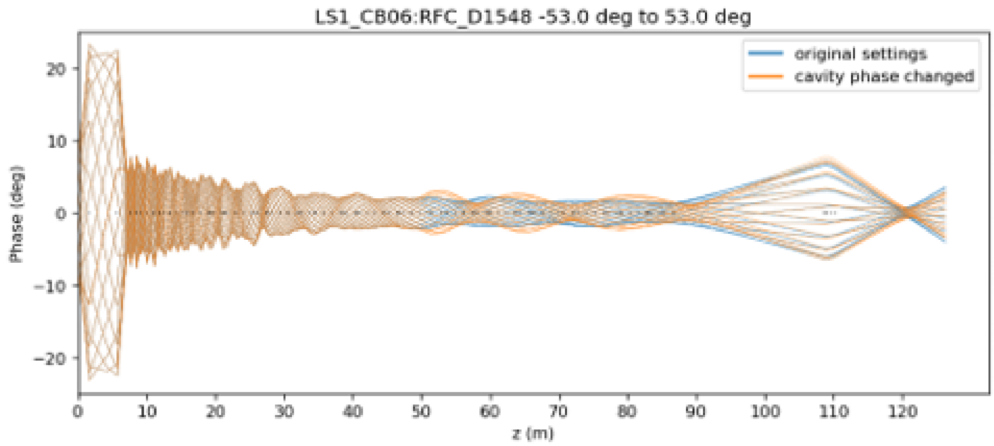

Figure 2.7: IPS simulated longitudinal beam envelopes in LS1 of design tune and when a cavity phase in the ninth cryomodule is changed by 106 degrees. Beam energy at this cavity is 10.5 MeV/u.

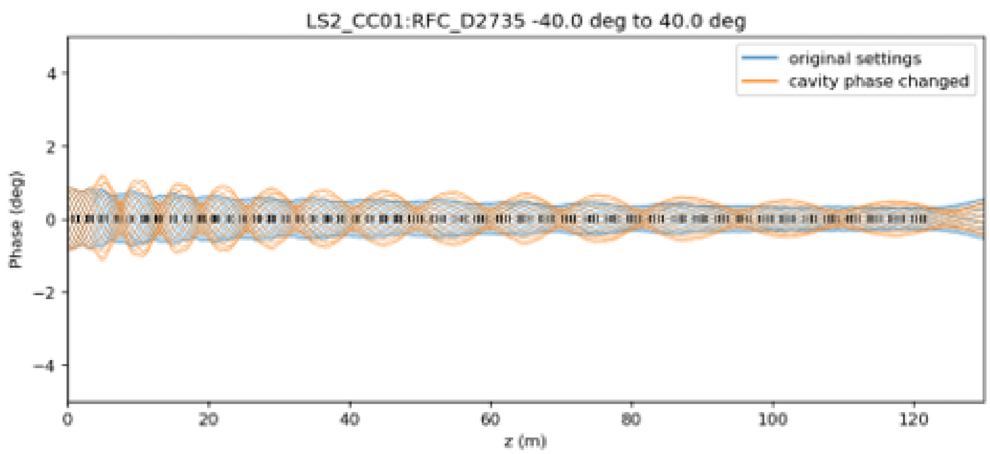

Figure 2.8: IPS simulated longitudinal beam envelopes in LS2 of design tune and when a cavity phase in the first cryomodule is changed by 120 degrees. Beam energy at this cavity is 21.7 MeV/u.

It is obvious from these figures that the effect of cavity phase change on beam size is much stronger at lower beam energies. Even in Fig. 2.7, where the beam energy is a relatively low 10.5 MeV/u at the changed cavity, the size of the beam that experiences the cavity phase change is only about 1 degree greater than the design beam. In Fig. 2.8, the difference is even less when the first LS2 cavity is changed. From these results, it is apparent that, besides the first few cryomodules, the phase changes induced by this application should not have a large effect on the longitudinal beam envelope.

The difference in energy gain is measured by looking at the difference in BPM phases between the new cavity phase and the initial cavity phase. Figure 2.9 shows the difference in BPM phases when a cavity in LS1 is changed by 30.0 degrees. The black bars represent the cavity positions in the lattice and the red bar represents the cavity currently being scanned. The application is using 10 BPMs for the measurement, represented by the blue dots. The period of the oscillation pattern shown in Fig. 2.9 depends on the beam energy. In the first four cryomodules of LS1 (CA to CB01), the period is short, so using between one and three BPMs for the calculation provides the most accurate results, according to tests and simulations. After CB01, when the beam energy is above 2 or 3 MeV/u, 10 BPMs provide the most accurate synchronous phase calculations.

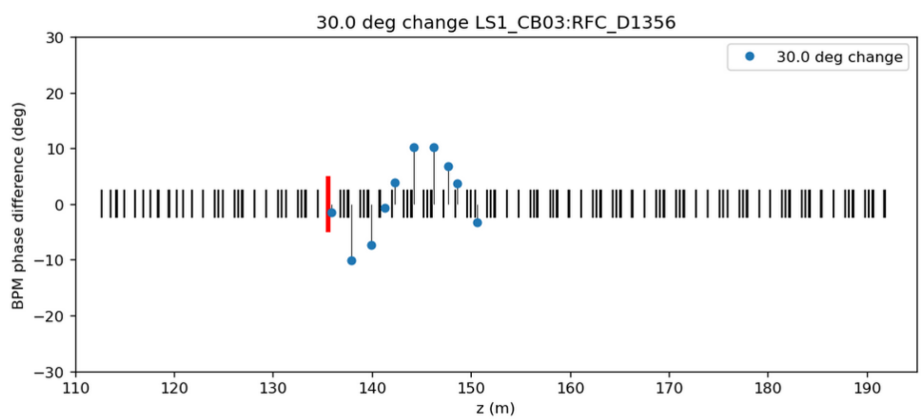

Figure 2.9: BPM phase difference when the phase of cavity D1356 in LS1 is changed by 30.0 degrees.

At each step of the phase scan, the phase difference in all BPMs used is squared and summed up. Then, the cavity phase change versus these sums of squared BPM phase differences is plotted as shown by the blue curve in Fig. 2.10. Next, the curve_fit function from the SciPy Python library is used to fit a cosine curve to this data, represented by the orange curve in Fig. 2.10. The synchronous phase of the cavity is half of the period of the fit cosine function. For the example in Fig. 2.10, the application calculated -39.96 degrees for the synchronous phase, while the actual setting was -40 degrees.

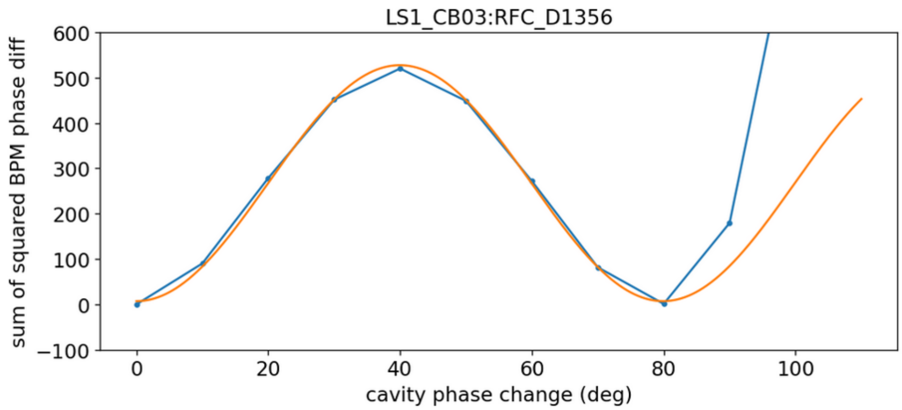

Figure 2.10: Sum of squared BPM phase differences from phase scan of cavity D1356 in LS1.

To develop this application, the algorithms were initially tested and verified with IPS simulations. Then, the application was tested on the FRIB linac as a Jupyter notebook. Next, a GUI was created using PyQt and features were added based on feedback from potential users. This GUI is shown in Fig. 2.11. The GUI contains three plots, the top showing the calculated synchronous phases as dots and the set synchronous phases as a dashed line. The middle plot is the same as Fig. 2.10, showing the sum of squared BPM phase differences and the cosine fit. The bottom plot shows the difference between the calculated synchronous phase and the set synchronous phase. Similar to the IPS GUI, the table shows cavities, set field amplitudes, set driven phases, and set synchronous phases. The table also shows live driven phase, the difference between live and set driven phases, calculated synchronous phases, and the difference between calculated and set driven phases. Users can choose the step size of the phase scan, the number of BPMs used in the measurements, and the time for each BPM measurement in the phase scan. The user can select multiple cavities in the table and the application will automatically scan all cavities selected. There is also a button which will scan all cavities in the same cryomodule as the cavity selected by the user.

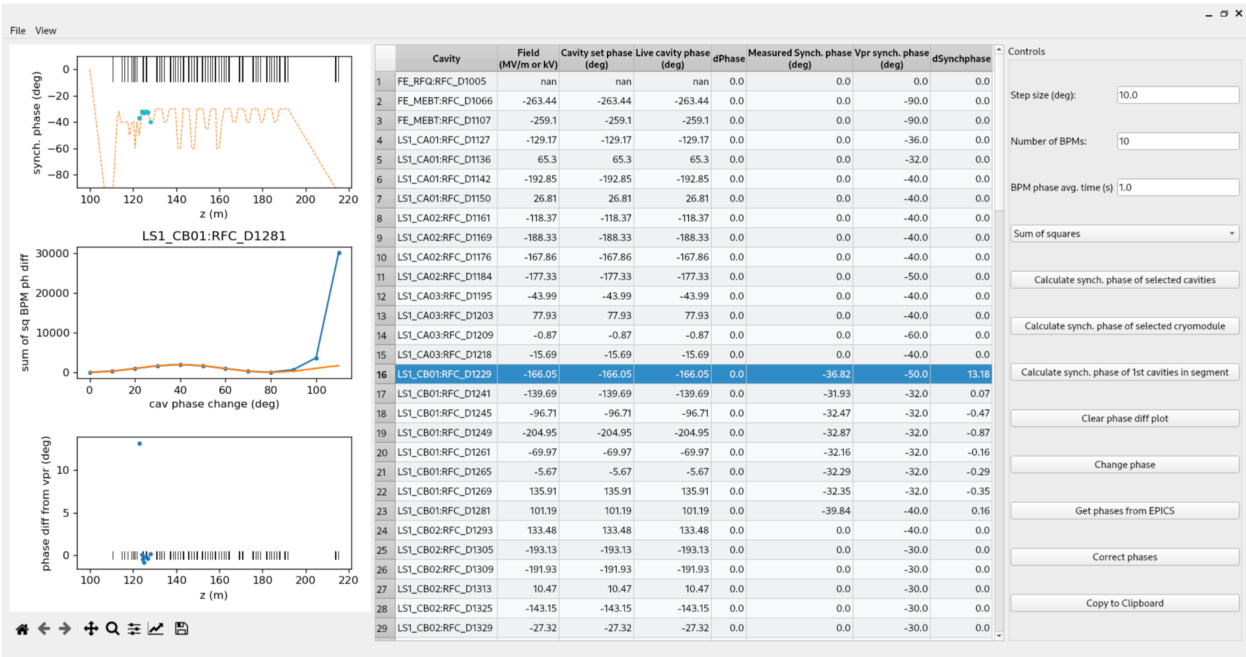

Figure 2.11: Graphical user interface (GUI) of synchronous phase calculation application.

From the final test of the application on the FRIB linac, the difference between the synchronous phase calculated by the application and the synchronous phase set by IPS is shown by the blue dots in Fig. 2.12.

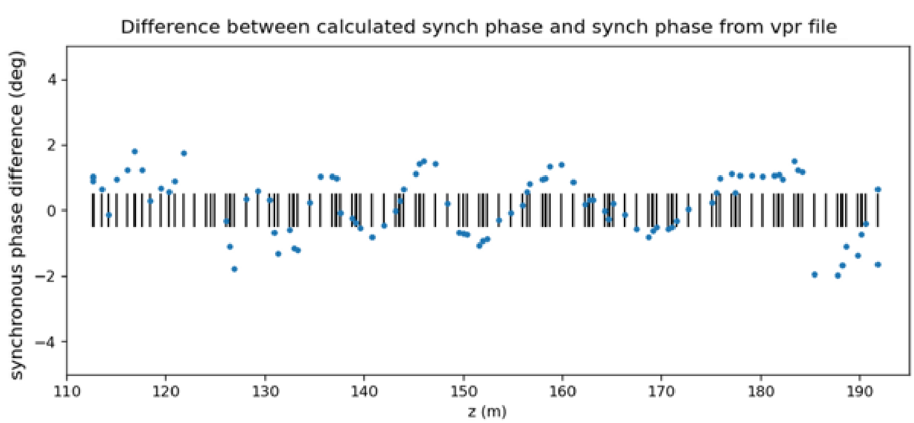

Figure 2.12: Difference between application calculated synchronous phase and synchronous phase from velocity profile. The black bars show the position of the accelerating cavities in LS1.

In this test, the correct synchronous phases of every cavity tested was able to be identified within $\pm$ 2 degrees. This accuracy can be improved by decreasing the step size of the phase scan, but this adds more time to the calculation. The $\pm$ 2 degree accuracy is good enough for us to identify which cavity has a calibration issue. The cavity can then be manually phased to more accurately determine the phase offset error and fix it.

Chapter 3. Multiple Charge State Beam Transport in Driver Linac

3.1 FLAME and TRACK Models

To support the beam dynamics optimization and simulations in FRIB linac, two code are used: TRACK [12] and FLAME [13]. TRACK is a 3-dimensional particle tracking code developed at Argonne National Laboratory to simulate the dynamics of multi-charge-state heavy ion beams. FLAME, which stands for Fast Linear Accelerator Model Engine, uses matrices to simulate trajectories and beam envelopes, which makes it very useful for various optimization problems, such as the development of the settings and fitting of the measurement data. FLAME is a linear optics code. After applying the FLAME-created settings to the machine, the CS parameters measured with profile monitors often do not match those in simulations.

In the FRIB linac, wire scanner profile monitors are used to measure the profile of a beam. To find the CS parameters, a technique known as a quadrupole scan is used. A set of 7-10 different currents in two quadrupoles close to the desired profile monitor are used and the horizontal, vertical, and diagonal beam sizes are measured at every step. Then horizontal emittance, vertical emittance, and CS parameters are optimized in FLAME until the FLAME simulation best fits the measurements at each step of the quadrupole scan. An example of the quadrupole scan fitting for a $^{238}U^{75+}$ beam is shown in Fig. 3.1. The x-axis represents each step of the quadrupole scan, the dots are the measurements, and the lines are the results of the FLAME simulation with the optimal CS parameters and emittances.

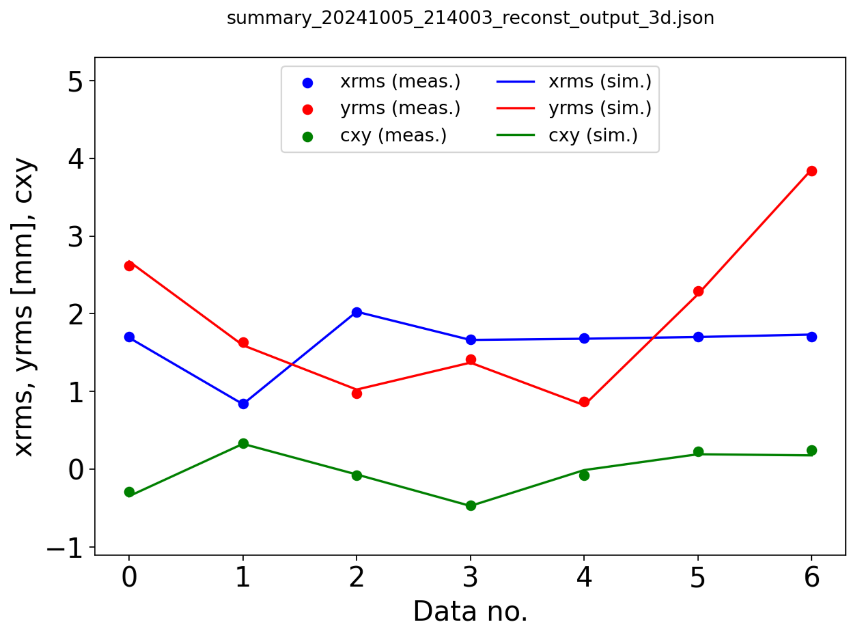

Figure 3.1: Fitting of a quadrupole scan of a $^{238}U^{75+}$ beam at a wire scanner profile monitor in FS1.

Each step of the quadrupole scan takes about two to three minutes, meaning one complete scan can take around 15 to 30 minutes. For a five-charge-state uranium beam, measuring all five charge states can take over two hours.

During primary beam development, we perform quadrupole scans in the MEBT, before the stripper, at the LS2 entrance, at the LS3 entrance, and in the BDS. Better simulation accuracy will reduce the amount of measurements needed, greatly reducing beam tuning time, and improve the quality of beam matching, which in turn will mitigate the beam loss. These two reasons provided motivation to investigate the simulation models and try to improve their accuracy [25].

3.1.1 Effective Lengths of Quadrupole Lenses

The studies presented in this chapter focus on FS1, more specifically the area between the stripper and the second multi-gap buncher (MGB02), which includes profile monitor PM D2602 to measure beam properties in FS1. The first task was to evaluate the effective length of quadrupoles using the 3D computer model. In FS1, there are two types of quadrupoles, Q1 quadrupoles are used in the straight sections and Q6 quadrupoles are used in the bending section. FLAME uses what is known as a "hard-edge" model, which ignores fringe fields by definition and models the magnetic field gradient as constant for a certain effective length in the longitudinal direction. The effective length is defined by:

$$L_{eff} = \frac{\int_{-\infty}^{\infty} G\,dl}{G_0} \tag{3.1}$$

where G_0 is the magnetic field gradient in the center of the magnet and $\int G(l)\,dl$ is the integral of the gradient in the longitudinal direction of the magnet. Due to the lack of 3D models of the quadrupole magnets, initially we set the effective lengths equal to their geometrical lengths, and used them until recently. The 3D models of quadrupoles were created in CST Studio based on their final drawings and their magnetic fields were simulated. Equation 3.1 was used to calculate the effective lengths displayed in Table 3.1. Figure 3.2 shows a profile of the magnetic field in a Q6 quadrupole magnet calculated by CST Studio compared with a hard-edge model with effective length calculated using Eqn. 3.1.

Table 3.1: Quadrupole Effective Lengths Calculated by CST Simulations

Quad Type	Effective Length (cm)	Geometric Length (cm)
Q1	26.1	25.0
Q4	38.1	33.5
Q5	45.1	40.5
Q6	28.9	25.0

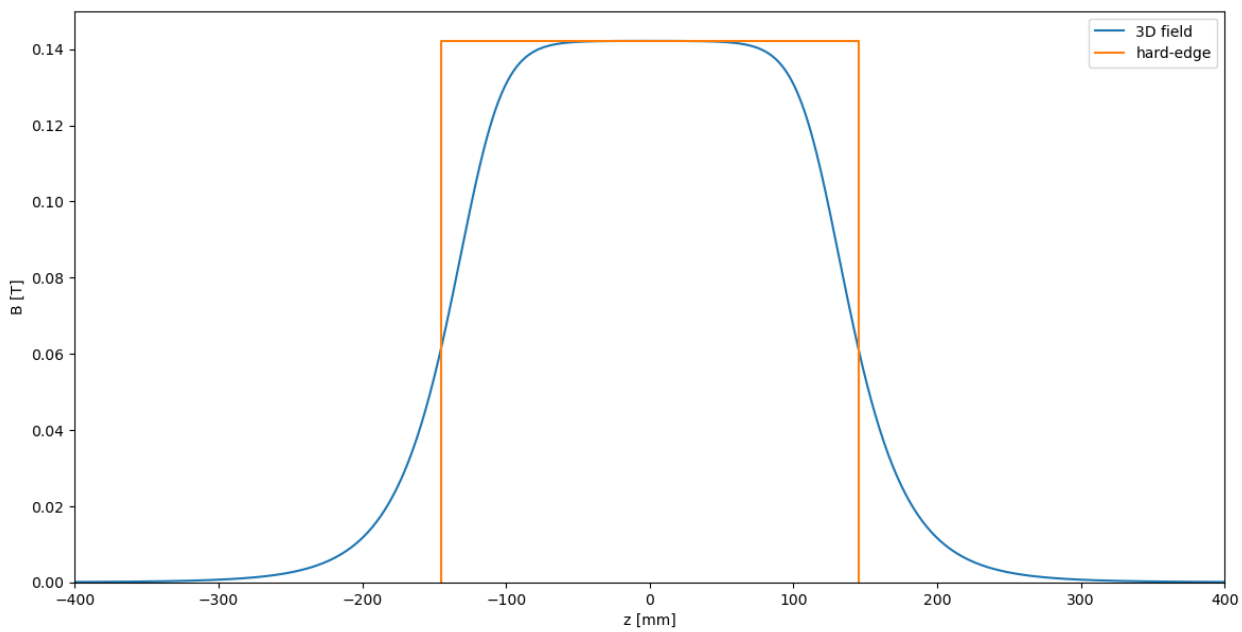

Figure 3.2: Comparison of magnetic field distribution at x = 0 mm, y = 30 mm (half of the aperture radius) in Q6 quadrupole magnet between CST simulation (“3D field”) and hard-edge model.

The TRACK model supports 3D field maps in dipoles and quadrupoles. The field maps have been generated using CST simulations. In the FLAME model, we had already been using the correct effective length for Q1 quadrupoles, so those were kept the same, while the effective lengths for the other quadrupole types were updated to their corresponding values in Table 3.1.

3.1.2 3D TRACK Model Validation

To validate the 3D TRACK model, two dipole correctors upstream of the first 45-degree FS1 bending dipole were used to kick the central trajectory of each charge state of a five-charge-state uranium beam by $\pm$ 2 mm in the vertical direction and $\pm$ 1 mm in the horizontal direction. The trajectories of the beam charge states throughout FS1 were measured with BPMs in all four cases and compared with the reference trajectory. The measured results from the stripper to the entrance of LS2 are shown as dots in Figs. 3.3 and 3.4. The lines show the centroid trajectories simulated with the TRACK 3D model. Inside the bending section, the BPM measurements did not match the simulations well because the BPM geometry is different from that in the straight sections, and the BPMs had not been properly calibrated for precise trajectory measurements. At all other BPMs, the simulated trajectories match the BPM measurements well, thus validating the updated model.

3.2 Transverse Beam Matching in Bending Sections of Driver Linac

In FS1, for a multi-charge-state beam, we do a quadrupole scan with PM D2602 and reconstruct the beam envelopes with FLAME for each individual charge state. Based on these reconstructed envelopes, the quadrupole fields between MGB02 and the entrance to LS2 are adjusted to match the beam to LS2. At the location of the stripper, the transverse beam size of each charge state should be equal. However, in the reconstructions, the rms beam

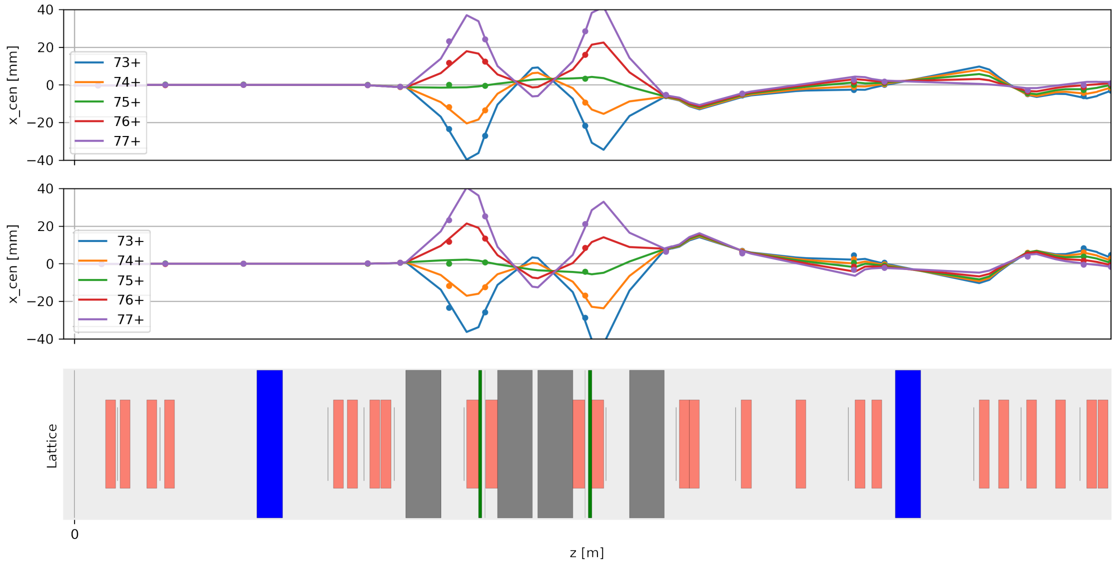

Figure 3.3: Comparison of horizontal central trajectory measurements (dots) and TRACK simulations (lines) for a five-charge-state uranium beam when each charge state enters the FS1 bending section with an offset of +1 mm (top) and -1 mm (middle). The FS1 lattice is shown in the bottom plot with red boxes as quadrupoles, blue as RF cavities, grey as dipoles, green as sextupoles and thin lines as correctors.

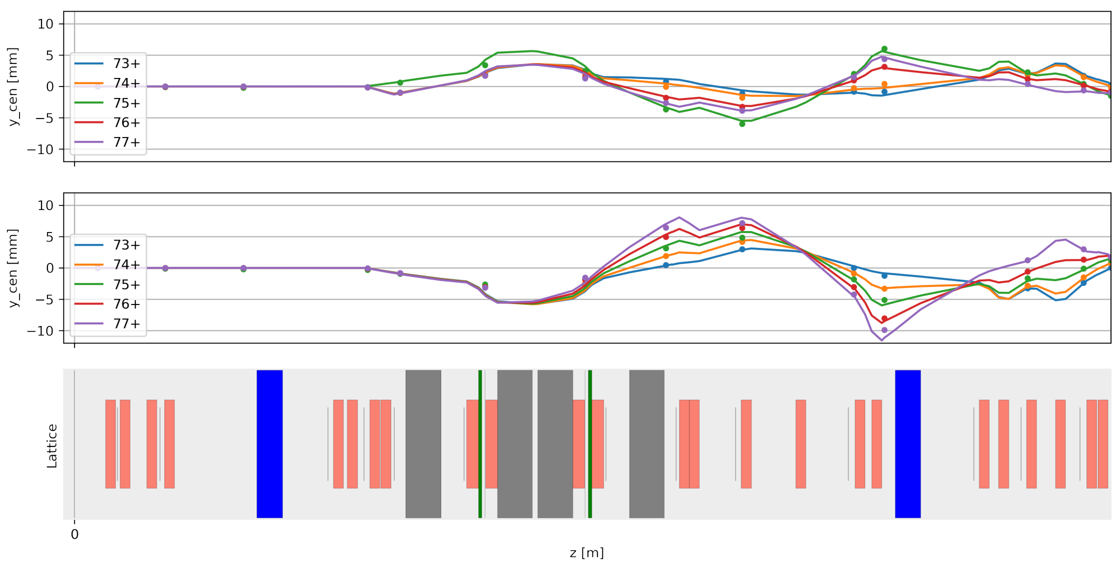

Figure 3.4: Comparison of vertical central trajectory measurements (dots) and TRACK simulations (lines) for a five-charge-state uranium beam when each charge state enters the FS1 bending section with an offset of +2 mm (top) and -2 mm (middle). The FS1 lattice is shown in the bottom plot with red boxes as quadrupoles, blue as RF cavities, grey as dipoles, green as sextupoles and thin lines as correctors.

size of each charge state at the stripper is different, especially in the vertical plane, meaning there is something wrong with the FLAME simulations. This can be seen in Table 3.2. Using a five-charge-state uranium beam with an energy of 16.5 MeV/u, measurements and simulation results were compared with the goal of improving the FLAME model, specifically in FS1.

The FLAME reconstruction at the profile monitor was used to generate a particle distribution for TRACK. Then, using TRACK, this distribution was simulated backwards from the profile monitor to the stripper and compared the beam sizes at the stripper for each charge state. A comparison of the rms beam sizes for each charge state at the stripper between this backwards TRACK simulation and the FLAME reconstruction is shown in Table 3.2.

Table 3.2: Comparison of ^{238}U Beam Sizes at Lithium Stripper

Charge State	x_{rms} TRACK (mm)	x_{rms} FLAME (mm)	y_{rms} TRACK (mm)	y_{rms} FLAME (mm)
73+	0.27	0.27	0.37	1.50
74+	0.27	0.31	0.29	0.97
75+	0.27	0.35	0.29	0.62
76+	0.26	0.32	0.27	0.42
77+	0.27	0.31	0.27	0.34

Next, the beam envelopes and trajectories in TRACK and FLAME were compared. The differences between the models originate in the bending section, which contains four 45-degree dipoles, four Q6 quadrupoles and two sextupoles. In both models, the sextupoles are hard-edge, so they cannot be responsible for the difference. After updating the effective length of the Q6 quadrupoles as described in the previous section, Fig. 3.5 compares the rms beam envelopes in FS1 between the forward FLAME simulation and the backwards TRACK 3D simulation. There is still a significant difference between the TRACK and FLAME simulations beginning in the bending section and propagating upstream to the stripper. Therefore, there must be a difference in the dipole models.

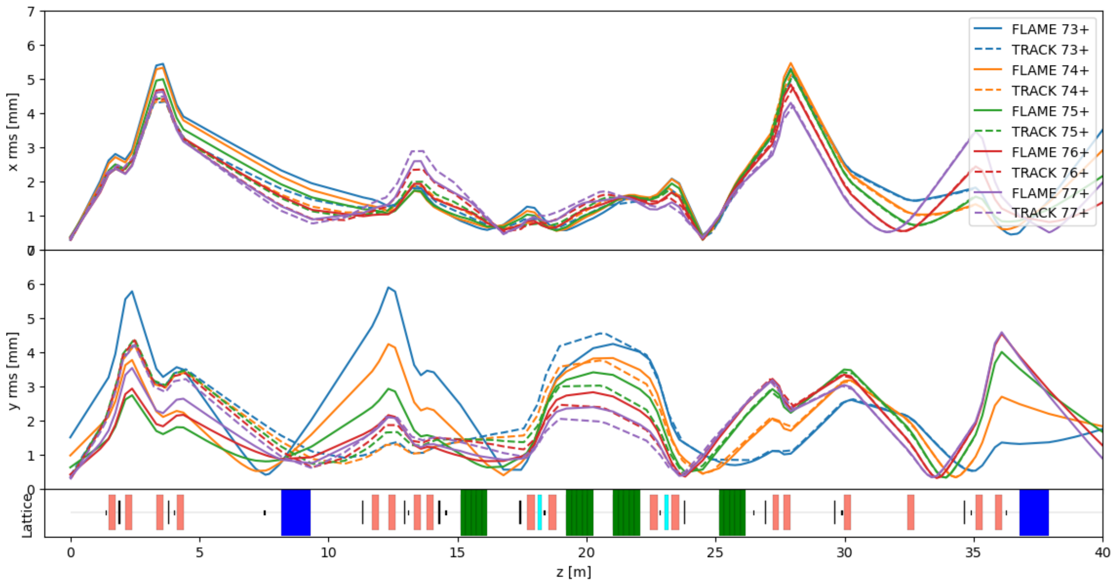

Figure 3.5: Comparison of rms beam envelopes beginning at the stripper between the backward TRACK simulation (dashed lines) and the forward FLAME simulation (solid lines) with updated Q6 quadrupole effective lengths.

3.2.1 Linear Dipole Corrections

FLAME uses a hard-edge dipole model, whereas the 3D field model has an extended length to include fringing fields. Similar to the previous section, the effective length of the D2 magnet, the 45-degree bending dipole used in FS1, was calculated in CST Studio. Those calculations showed an effective length 5% higher than the geometrical length used in the FLAME model. The FS1 dipoles in the FLAME model were updated to this higher effective length.

Simulations through a short drift space and one dipole magnet were performed with the goal of matching FLAME results to the TRACK 3D dipole results. When comparing vertical trajectories in FLAME, the dipole fringe field focused all charge states by the same amount. The FLAME source code was then changed to account for the difference in charge states. After this update, the FLAME simulations still did not match the TRACK simulations.

FRIB dipoles bend the beam in the horizontal plane. The fringe magnetic fields of the dipole also provide linear quadrupole-like focusing in both the horizontal and vertical directions, which depend on the pole face angle of the dipole. This report on a linear code called TRANSPORT [26, 27] provides the 4×4 transfer matrix of these dipole fringing fields:

$$\begin{bmatrix} 1 & 0 & 0 & 0 \\ \frac{\tan(\psi)}{\rho} & 1 & 0 & 0 \\ 0 & 0 & 1 & 0 \\ 0 & 0 & \frac{-\tan(\psi-\beta)}{\rho} & 1 \end{bmatrix} \tag{3.2}$$

where ρ is the bending radius, ψ is the pole face angle, and β is a correction to the pole face angle in the vertical direction. The correction angle is responsible for the variation of the pole gap height [28]. Previously, the FLAME code did not include this β term and a charge state dependence term, so the source code was updated to add them. After the source code updates, the FLAME transverse 4×4 dipole fringe transfer matrix looks like:

$$\begin{bmatrix} 1 & 0 & 0 & 0 \\ \frac{\tan(\psi)}{\rho}\frac{q}{q_{ref}} & 1 & 0 & 0 \\ 0 & 0 & 1 & 0 \\ 0 & 0 & \frac{-\tan(\psi-\beta)}{\rho}\frac{q}{q_{ref}} & 1 \end{bmatrix} \tag{3.3}$$

where q is the ion charge state and q_{ref} is the charge state of the central or reference ion (75+ for this five-charge-state uranium study). Using a simulation with sextupoles turned off, ψ and β were optimized to best fit FLAME envelopes and trajectories of all five charge states to those from the TRACK 3D model simulations using a Nelder-Mead optimization algorithm. While the geometrical pole face angle is -7.0°, this optimization produced values of -6.66° for the horizontal plane and -6.15° for the vertical plane. Figure 3.6 shows a comparison of the rms beam envelopes between this updated FLAME model and the TRACK 3D model when both simulations are given the same initial CS parameters at the stripper. As can be seen in the figure, all charge states still do not perfectly match, especially 73+ and 77+, the "outer" charge states. There must be non-linear effects responsible for the residual mismatch.

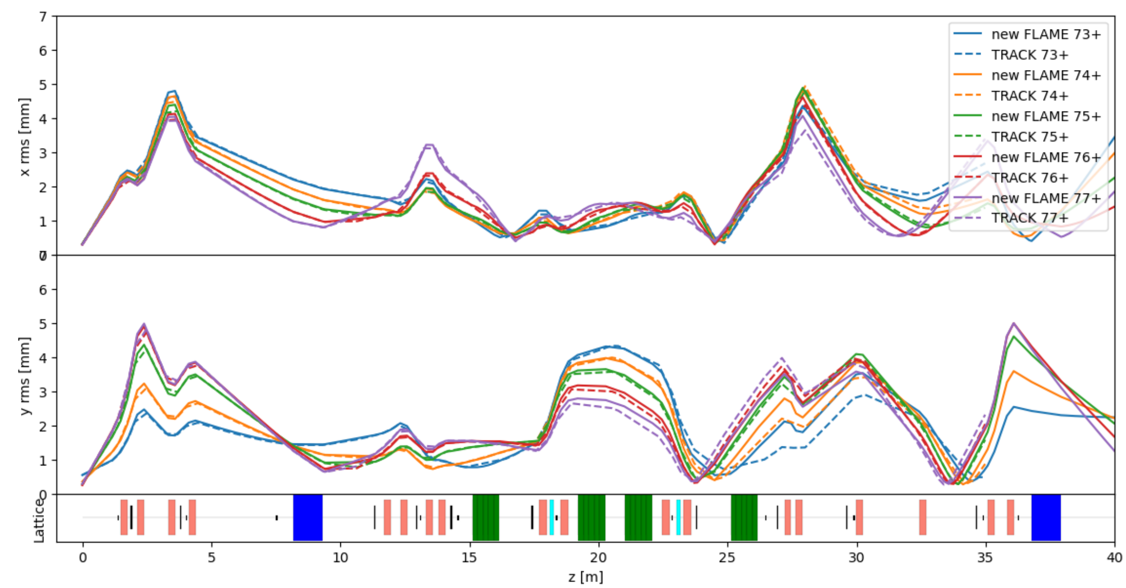

Figure 3.6: Comparison of rms beam envelopes beginning at the stripper between the updated FLAME simulation (solid lines) and a TRACK simulation (dashed lines) with the same initial conditions.

3.2.2 Non-Linear Dipole Corrections

Despite being a linear optics code, FLAME contains a sextupole element that approximates the non-linear effects of a sextupole magnet on a beam. To reproduce the sextupole component present in the magnetic field of the 3D dipole, a few very thin sextupole elements were distributed inside the FLAME dipole. The strength of these sextupoles was then scaled to best fit the TRACK 3D envelopes and trajectories for a five-charge-state uranium beam.

After this fitting, the new FLAME model was used to optimize the parameters of the sigma matrix for each charge state at the stripper to best fit the measurements of the quadrupole scan. This is similar to the procedure used while performing beam reconstruction for matching. The results are shown in Table 3.3. It is obvious when compared to the results of Table 3.2, that this new model produces nearly equal beam sizes at the stripper for each charge state, which is expected. The results from this new model are close to what was produced in the TRACK 3D backwards simulations. Using the new FLAME settings and scaling the fields in the thin sextupoles by beam rigidity, results between FLAME and TRACK were compared for a two-charge-state selenium beam and a two-charge-state calcium beam, which are other multi-charge-state beams commonly accelerated in the FRIB linac. The envelopes produced by the new FLAME model show definite improvement from the original FLAME model. To match perfectly, the distribution and field strength of the FLAME sextupole elements can be further optimized and higher order multipoles could be added.

Table 3.3: Comparison of ^{238}U Beam Sizes at Lithium Stripper using the new FLAME model

Charge State	x_{rms} TRACK (mm)	x_{rms} FLAME (mm)	y_{rms} TRACK (mm)	y_{rms} FLAME (mm)
73+	0.27	0.26	0.37	0.36
74+	0.27	0.29	0.29	0.30
75+	0.27	0.32	0.29	0.31
76+	0.26	0.30	0.27	0.30
77+	0.27	0.30	0.27	0.30

Chapter 4. Beam Power Ramp-up and Mitigation of Beam Losses

4.1 High Intensity Beam Dynamics at the Front End

Front End is the section of the linac where the beam is produced and transported for the following acceleration. Production of high-intensity heavy-ion beams is always a challenging problem from ion sources. Transport of intense beams is a difficult problem as well. Coulomb repulsion between ions in the beam effectively causes its defocusing. Transport of the beam considering the space charge effects is a common problem in accelerator physics and is briefly described below.

For a simplified approximation of transverse beam dynamics affected by space charge, the beam is assumed to be circular in x-y space with radius r_b and has a uniform, constant charge density $\rho = \frac{\lambda}{\pi r_b^2}$ where λ is a constant line charge. After applying Gauss' Law to calculate the electric field inside the beam (for $r \leq r_b$):

$$\vec{E_r} = \frac{\lambda r}{2\pi\epsilon_0 r_b^2}\hat{r} \tag{4.1}$$

This shows the field inside the beam is linear. Now let us apply the transverse equations of motion. First, after changing Eqn. 4.1 to x and y coordinates, using $r = \sqrt{x^2 + y^2}$ for the electric field inside the beam:

$$\begin{aligned} E_x &= E_r \frac{x}{r} \\ E_y &= E_r \frac{y}{r} \end{aligned} \tag{4.2}$$

Therefore, assuming $k_x = k_y = k_0^2 =$ constant, the equations of motion are:

$$\begin{aligned} x'' + k_0^2 x &= \frac{-q}{m\gamma_b^3\beta_b^2c^2}E_x = \frac{-q\lambda}{2\pi\epsilon_0 m\gamma_b^3\beta_b^2c^2}\frac{x}{r_b^2} \\ y'' + k_0^2 y &= \frac{-q}{m\gamma_b^3\beta_b^2c^2}E_y = \frac{-q\lambda}{2\pi\epsilon_0 m\gamma_b^3\beta_b^2c^2}\frac{y}{r_b^2} \end{aligned} \tag{4.3}$$

Next, define a constant quantity Q, known as the dimensionless perveance, as:

$$Q = \frac{q\lambda}{2\pi\epsilon_0 m\gamma_b^3\beta_b^2c^2} \tag{4.4}$$

Then, for the equations of motion:

$$\begin{aligned} x'' + \left(k_0^2 - \frac{Q}{r_b^2}\right)x = 0 \\ y'' + \left(k_0^2 - \frac{Q}{r_b^2}\right)y = 0 \end{aligned} \tag{4.5}$$

It is apparent from this equation, that the space charge term works against k_0^2, the focusing term from the lattice. Space charge reduces or "depresses" phase advance provided by the lattice and slows down transverse particle oscillations. Equation 4.4 shows that Q is proportional to $\frac{1}{\gamma^3}$ and $\frac{1}{\beta^2}$, so the effects of space charge are much more pronounced in the front end, where the average beam energy is 12 keV/u, compared to even just after the RFQ, where the average beam energy is 500 keV/u.

Longitudinally, the beam is a DC beam until reaching the MHB, where it is bunched to form a small longitudinal emittance, as described in Section 2.1. It then travels a short distance before being accelerated by the RFQ. It is difficult to decouple longitudinal space charge effects with the effects of MHB bunching because the drift space between the MHB and RFQ is so small (under 1 m). Such a problem can be solved numerically, for example, by using Particle-in-Cell codes. TRACK is one of these codes. All of the front end simulations described in this chapter include space charge effects.

4.1.1 2q Acceleration in RFQ and LS1 to Double Beam Power

For heavier beams, ranging from xenon through uranium, the FRIB ECR ion source is currently not capable of producing enough beam current for 400 kW beam power on target. Therefore, an essential step of the FRIB beam power ramp up is two-charge-state acceleration through the RFQ and LS1. This will instantly double the beam power. To achieve this in LS1, the dynamics will be similar to multi-charge-state acceleration in LS2. We will need to develop cavities' settings to control the phase oscillations of both charge states and to make them arrive at the stripper simultaneously. Additionally, two-charge-state injection into the RFQ becomes slightly more complicated. It will require the installation of a resonant cavity between the MHB and the RFQ entrance known as the velocity equalizer.

4.2 Development of Velocity Equalizer

In the case of single-charge-state acceleration, the beam is extracted from the ECR ion source into the LEBT and accelerated in a DC column to an energy of 12 keV/u. For two-charge-state acceleration of a $^{238}U^{33+,34+}$ beam, the lower charge state would be accelerated to 11.8 keV/u and the higher charge state to 12.2 keV/u. After longitudinal bunching at the MHB, each charge state will drift at different mean velocities to the entrance of the RFQ. Because the bunches will not be separated by 360° at the RFQ frequency of 80.5 MHz and they have different energies, many particles will not be accelerated in the RFQ, leading to a decrease in beam transmission compared to the single-charge-state case. A 40.25 MHz RF cavity has been designed to equalize the velocity of both charge states, as well as a biased, high-voltage drift tube to make the time-of-flight difference of 12.4 ns or 1/80.5 MHz between the bunches. This will allow for maximum transmission through the RFQ of two-charge-state-beams. Figure 4.1 shows snapshots of longitudinal phase space of a ^{238}U two-charge state beam simulated in TRACK from the MHB to the RFQ entrance including the biased tube and velocity equalizer.

4.2.1 Biased Drift Tube

To ensure the charge states are properly separated in time at the velocity equalizer and RFQ entrance, a high-voltage biased drift tube is required in between the MHB and the velocity equalizer. First, the length of this drift tube that will minimize the necessary voltage had to be determined. The distance between the MHB and velocity equalizer is 1.16 m, and the maximum length of the tube is 0.86 m, as there is a 0.15 m distance between the MHB and its flange and another 0.15 m between the velocity equalizer and its flange. The time-of-flight difference, Δt between charge states q_1 and q_2 is described by this equation:

$$\Delta t = L\left(\frac{1}{v_2} - \frac{1}{v_1}\right) \tag{4.6}$$

where L is the drift length and v_1, v_2 are the velocities of q_1, q_2 respectively. Outside the tube, the kinetic energies of the charge states are:

$$\begin{aligned} W_{1,out} &= q_1 e U_0 \\ W_{2,out} &= q_2 e U_0 \end{aligned} \tag{4.7}$$

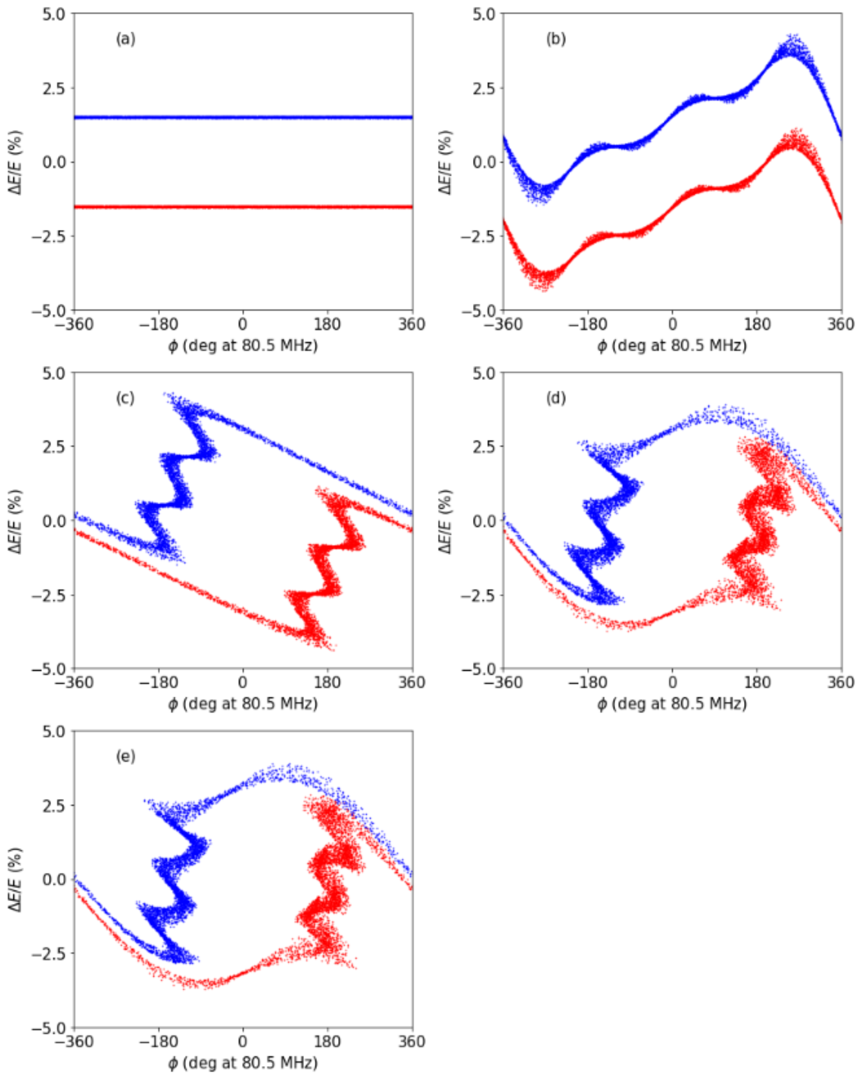

Figure 4.1: Longitudinal phase space of a ^{238}U two-charge-state beam (33+ in blue and 34+ in red): (a) before the MHB, (b) after the MHB, (c) before the velocity equalizer, (d) after the velocity equalizer, (e) at the RFQ entrance.

where U_0 is the total accelerating voltage from the ion source and e is the elementary charge.

Inside the tube, the kinetic energies are:

$$\begin{aligned} W_{1,in} &= q_1 e(U_0 - U_{tube}) \\ W_{2,in} &= q_2 e(U_0 - U_{tube}) \end{aligned} \tag{4.8}$$

where U_{tube} is the voltage on the tube. As the beam energy is very low, kinetic energy can be converted to velocity non-relativistically using:

$$v = c\sqrt{\frac{2W}{m}} \tag{4.9}$$

where c is the speed of light and m is the average mass of a nucleon (931.5 MeV) multiplied by the mass number of the ion species in the beam. For the time difference inside the tube, Eqns. 4.6 and 4.9 are used, then:

$$\Delta t_{tube} = \frac{L_{tube}}{c}\left(\sqrt{\frac{m}{2q_2e(U_0 - U_{tube})}} - \sqrt{\frac{m}{2q_1e(U_0 - U_{tube})}}\right) \tag{4.10}$$

and after solving for U_{tube}:

$$U_{tube} = U_0 + \left(\frac{mL_{tube}^2}{2ec^2\Delta t_{tube}^2}\right) \cdot \left(\frac{2}{\sqrt{q_1q_2}} - \frac{1}{q_2} - \frac{1}{q_1}\right) \tag{4.11}$$

Then, to solve for Δt_{tube}:

$$\Delta t_{tube} = \Delta t_{total} - \Delta t_{gaps} \tag{4.12}$$

where Δt_{total} is 12.4 ns or 1/80.5 MHz. Equations 4.6, 4.7, and 4.9 can be used to solve for Δt_{gaps}.

$$\Delta t_{gaps} = \frac{L_{gaps}}{c}\sqrt{\frac{m}{2eU_0}}\left(\frac{1}{\sqrt{q_2}} - \frac{1}{\sqrt{q_1}}\right) \tag{4.13}$$

Using Eqns. 4.11, 4.12, and 4.13, the required tube voltage for a range of tube lengths ranging from 0.3 m to the maximum 0.86 m were calculated for four different beam species. The results are shown in Fig. 4.2. It is clear that a longer tube reduces the amount of voltage necessary, so the length of the biased tube was set at 0.86 m, the maximum amount of space available. The voltage required at this length for multiple beam species are described in Table 4.1.

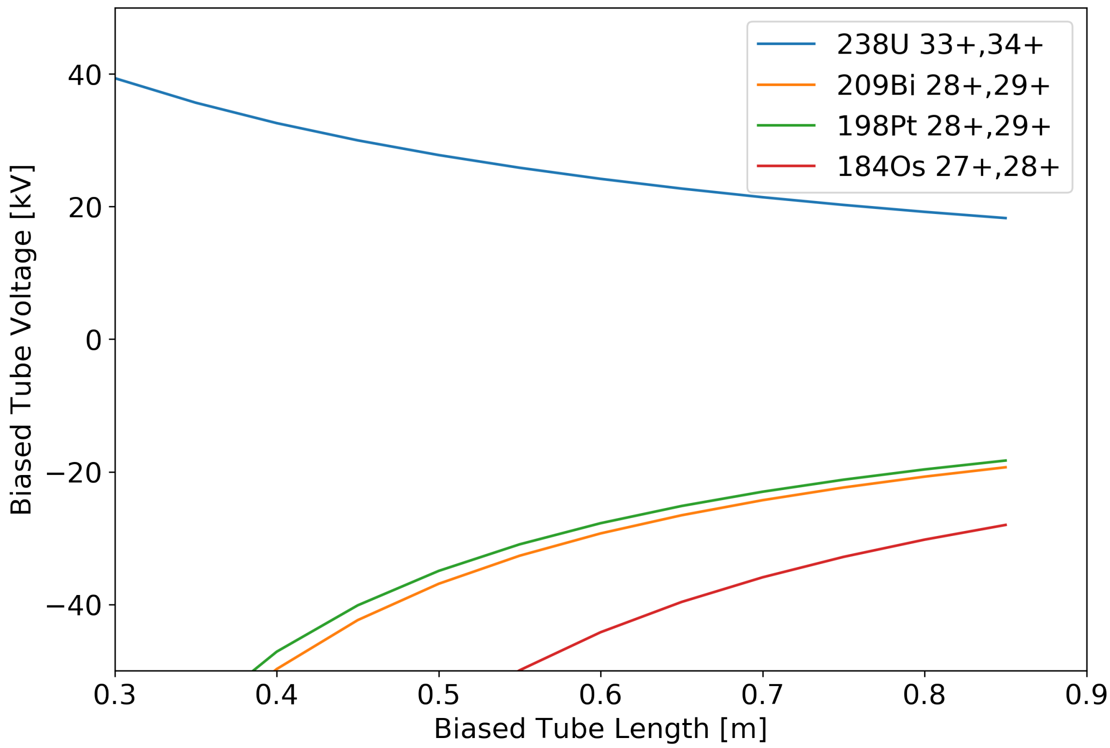

Figure 4.2: Length of biased tube versus biased tube voltage required to produce charge state separation of 12.4 ns.

Table 4.1: Required Voltage for Biased Tube

Element	Mass Number	Charge States	Tube Voltage [kV]
Os	184	27,28	-27.6
Pt	198	28,29	-18.1
Hg	204	27,28	-30.6
Pb	208	27,28	-31.2
Bi	209	28,29	-19.0
U	238	33,34	18.0

4.2.2 Resonator Design

The velocity equalizer will be a quarter wave resonator with a frequency of 40.25 MHz. At the resonator, the charge states will be separated by 80.5 MHz, as shown in Fig. 4.1 (c), so the resonant frequency of the velocity equalizer is half of that so the lower charge state will be accelerated and the higher charge state will be decelerated, bringing them both to an average energy of 12 keV/u for injection to the RFQ, as shown in Fig. 4.1 (d).

Directly upstream of the RFQ entrance is a diagnostic box with a Faraday cup and a profile monitor. The velocity equalizer was designed to fit in an available port of this diagnostic box, closest to the RFQ entrance. A layout of this area is shown in Fig. 4.3, including the biased tube.

The resonator will provide an effective voltage of 1.5 kV, which corresponds to an input RF power of 200 W. Because of the relatively low frequency, the resonator will have a spring inductive load. The center-to-center distance between the two gaps is 18.9 mm. Other

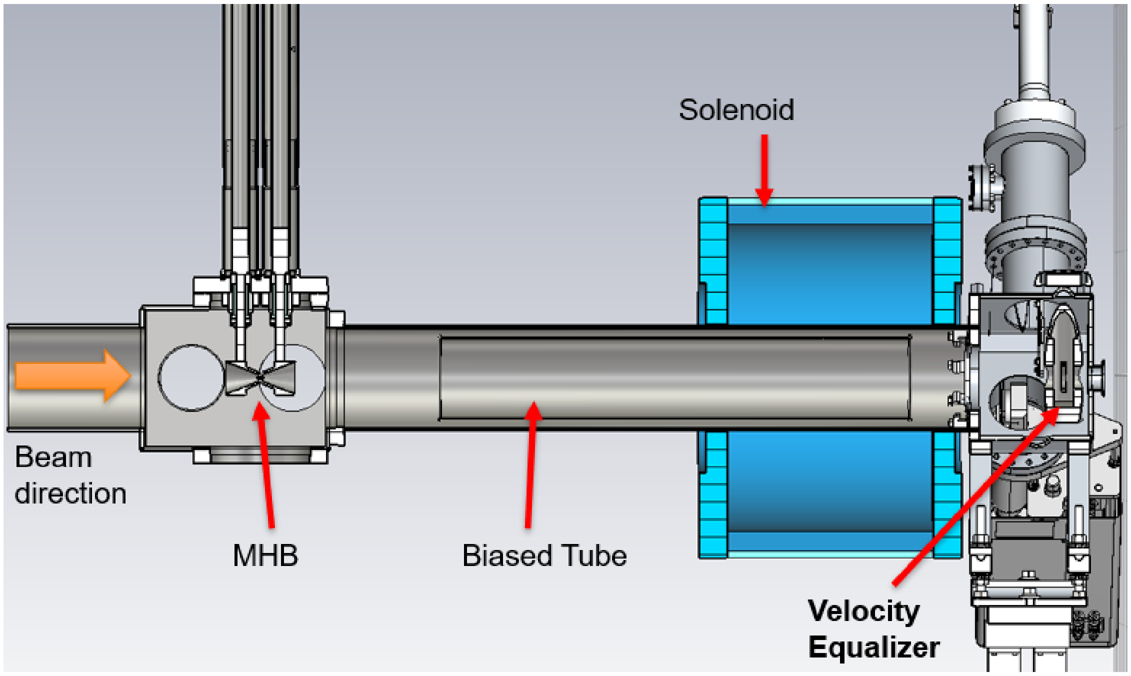

Figure 4.3: Cross-section view of the area between the MHB and the RFQ entrance.

relevant dimensions are shown in Fig. 4.4.

According to the TRACK simulations from Fig. 4.1, transmission of two charge states through the RFQ without the velocity equalizer and the biased drift tube is around 40%. With the velocity equalizer and biased tube, the transmission increases to 80%, which is equal to the transmission for single-charge-state beams.

4.3 Beam Losses in Post-Stripper Linac

The liquid lithium stripper is superior to the traditional carbon foil stripper, which is damaged at high power densities. Although the beam is transversely focused on the stripping film, inherent non-uniformity of the film thickness within the beam spot [17] introduces extra energy spread in the beam via the energy loss mechanism, in addition to energy straggling [19, 29, 30]. To minimize the longitudinal emittance growth due to these effects, the beam is

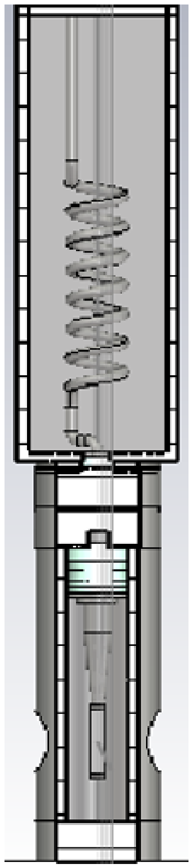

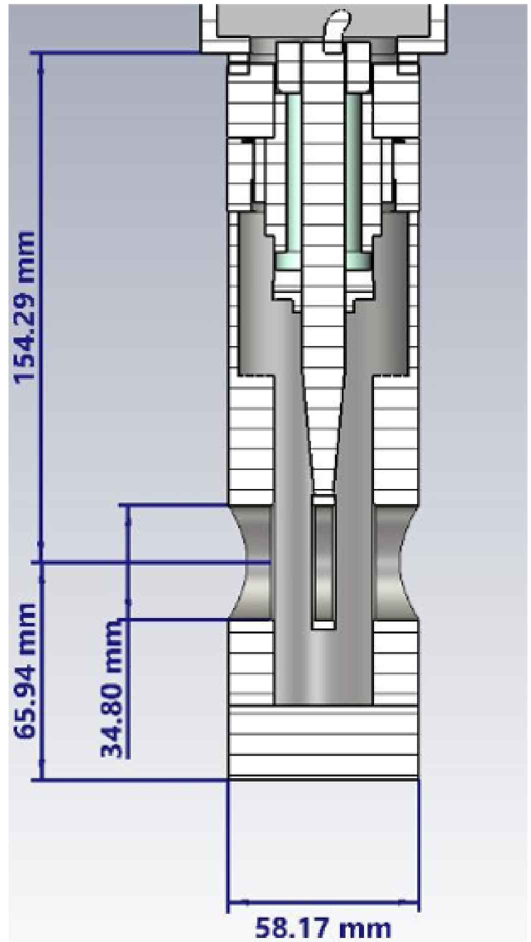

Figure 4.4: Full cross-section view of the velocity equalizer resonator (left) and zoomed-in view with relevant dimensions (right).

also focused longitudinally (see Fig. 4.5). Long drift space of the 180-deg bend, as well as the beam focusing on the lithium film, require longitudinal matching between superconducting linac segments. This is done by two 161 MHz Multi-Gap Bunchers (MGBs) [31] to keep the beam longitudinally rms bunched before entering the second accelerating segment (LS2). The longitudinal beam size of a 16.5 MeV/u $^{238}U^{75+}$ beam is displayed in Fig. 4.5 from the stripper to the entrance to LS2. Figure 5.1 shows a zoomed-in view of the layout between the stripper and the entrance to LS2.

A comprehensive numerical study of the beam losses in a high-intensity heavy ion linac [29] showed that in stripped beams one should expect an energy distribution with a "tail"

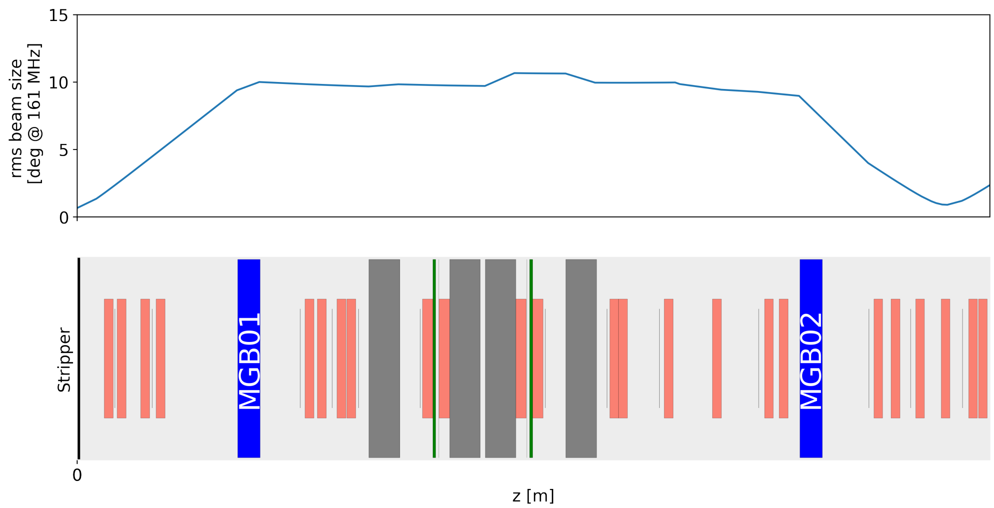

Figure 4.5: Longitudinal rms beam size in FS1 from the stripper to the entrance of LS2. The blue boxes represent cavities, the red are quadrupoles, the thick grey boxes are dipoles and the thin greys are sextupoles.

extending toward lower energies. The "tail" may extend by several hundreds of keV/u and contain up to 0.1% of the beam intensity. This fraction is difficult to observe at low beam power, but at the FRIB intensities, it starts playing an important role in the beam loss distribution. The bunch focused to the lithium film, elongates very quickly after passing through the stripper. The large longitudinal beam size leads to non-linear "tails" in the longitudinal phase space distribution after the beam experiences the sinusoidal 161 MHz effective bunching voltage at MGB01. According to the beam dynamics analysis, particles in these "tails" are lost in the LS2 cryomodules. The lost fraction of the beam in the LS2 cryomodules does not exceed 10^{-4}, which corresponds to a temperature increase of up to 0.3 K in the beam pipe during 10 kW beam power on target operation [14]. As beam power ramps up to our ultimate goal of 400 kW [32], the temperature increase in the cryomodules will also grow, which may lead to degradation of SRF cavities due to enhancement of field emission. Therefore, it is necessary to mitigate these losses.

4.3.1 Losses due to Sudden Thickness Changes

Occasionally during operation, the lithium film stripper thickness will suddenly change, causing a change in average energy loss through the stripper. This means the beam is longitudinally mismatched to LS2 where losses can be observed.

On July 1, 2024, the stripper thickness suddenly changed at 12:50 am and the beam continued to run for 20 minutes until the loss monitors tripped at 1:10 am. At the moment of this sudden change, the beam energy after the stripper changed from 16.52 MeV/u to 16.43 MeV/u. In LS2, to detect losses, there are neutron detectors located on the outside of every other cryomodule and two X-ray monitors located outside each cryomodule. In the LS2 CC cryomodules, (the first 12 cryomodules of LS2) there are temperature sensors located on the beam pipe. Data from all these monitors was analyzed to determine the location of the losses in LS2 caused by the sudden change in stripper film thickness. Figure 4.6 shows measured increase in temperature before and after this sudden change in stripper thickness. The reference temperatures for each cryomodule were measured on the day before when the beam had been off for multiple hours. The blue bars in Fig. 4.6 show the loss profile of the beam during "normal" operation, with over 0.5 K temperature increase observed in CC05, with CC07 and CC03 having the next highest increases. However, when the film thickness changes, and the input energy to LS2 changes, we see the highest temperature increase in CC03. After the thickness change, there is a significant increase in temperature in all cryomodules except for CC01. To further support this data, X-ray monitor and neutron detector readings in all 24 cryomodules in LS2 were checked before and after the thickness change. The change in X-ray monitor readings is shown in Fig. 4.7 and the neutron detector readings are shown in Fig. 4.8. All three histograms support a large increase in losses from

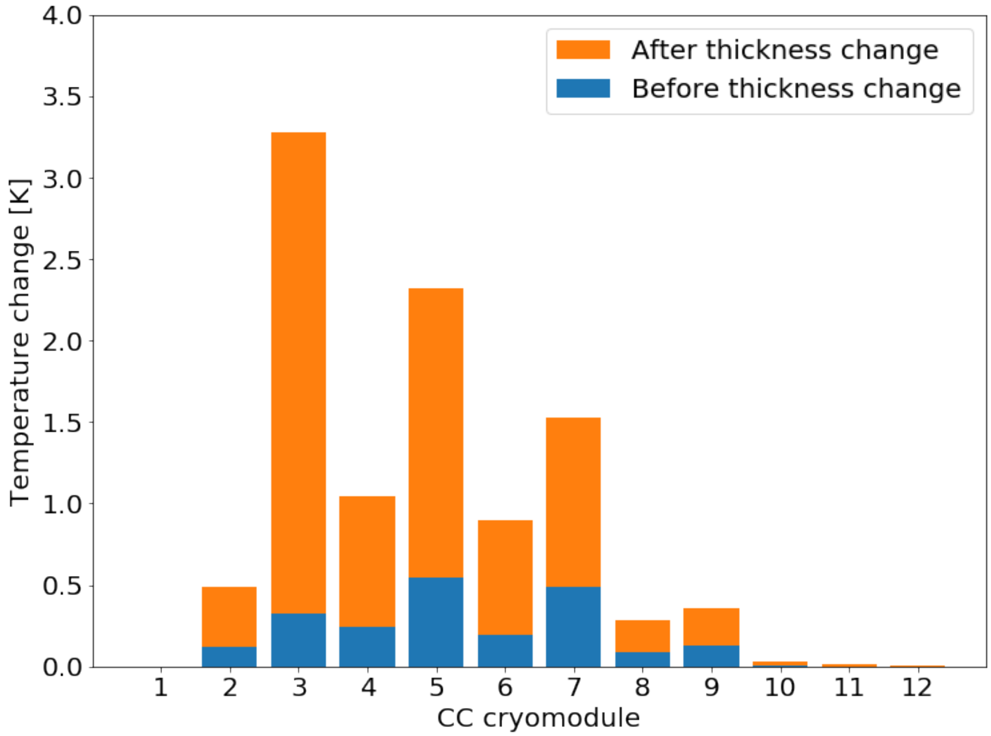

Figure 4.6: Measured temperature increase in LS2 CC cryomodules before and after sudden change of lithium stripper film thickness on July 1, 2024.

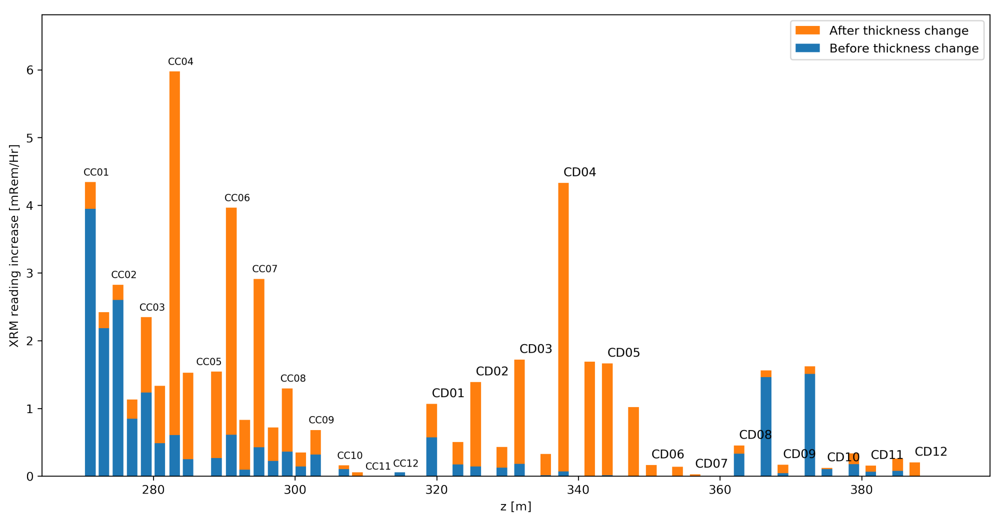

Figure 4.7: Measured X-ray monitor increase in LS2 cryomodules before and after sudden change of lithium stripper film thickness on July 1, 2024.

CC03 to CC09 after the stripper thickness changed. There are no temperature sensors in the CD cryomodules, but from the X-ray monitors and neutron detector readings, a large

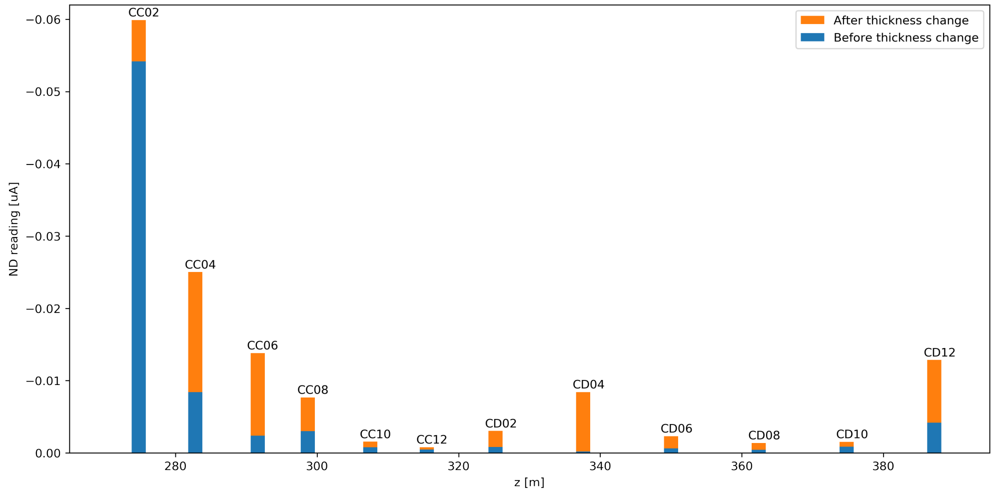

Figure 4.8: Measured neutron detector readings in LS2 CC cryomodules before and after sudden change of lithium stripper film thickness on July 1, 2024.

increase in losses between CD02 and CD05 can be inferred. To mitigate these losses due to sudden changes in stripper thickness, two feedback systems have recently been implemented. One changes the phase of the last cavity in LS1 and one bunching CH cavity to keep the bunch arrival time to the stripper and the energy of the beam after the stripper unchanged with 0.1 s time constant. The other system moves the stripper film in the vertical direction to compensate for a change in stripper thickness within one to two minutes. However, due to the limited time constant, both feedback systems do not completely compensate for the sudden change of the stripper film thickness.

Chapter 5. Development of Second Harmonic Cavity

5.1 Multi-physics design

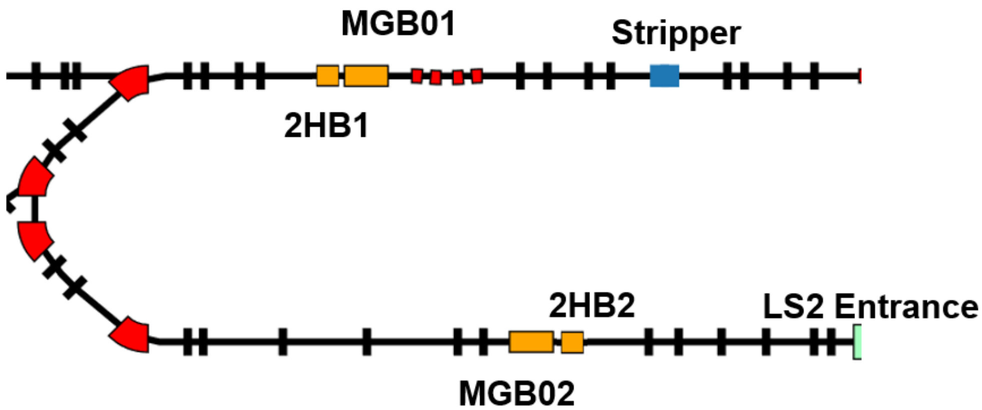

Figure 5.1: Folding Segment 1 (FS1) layout.

We propose to eliminate the LS2 beam losses discussed in the previous section by linearizing the effective voltage of the MGB. To do this, a Second Harmonic Buncher (2HB) cavity has been designed to be installed downstream of each MGB as seen in Fig. 5.1 [33, 34]. This new cavity will have a resonant frequency of 322 MHz, which is twice the resonant frequency of the MGBs. The effect of this second harmonic is shown in Fig. 5.2. In the case of the two combined harmonics (orange), the amplitude of the first harmonic is increased by a factor of 1.3 compared to the original case (blue) and the ratio of the second harmonic amplitude to the first harmonic amplitude is -0.115 to keep the slope of the linear regions of both cases equal. The effective bunching voltage waveform of the combined harmonics has a significantly longer linear region than the waveform of the 161 MHz MGB only.

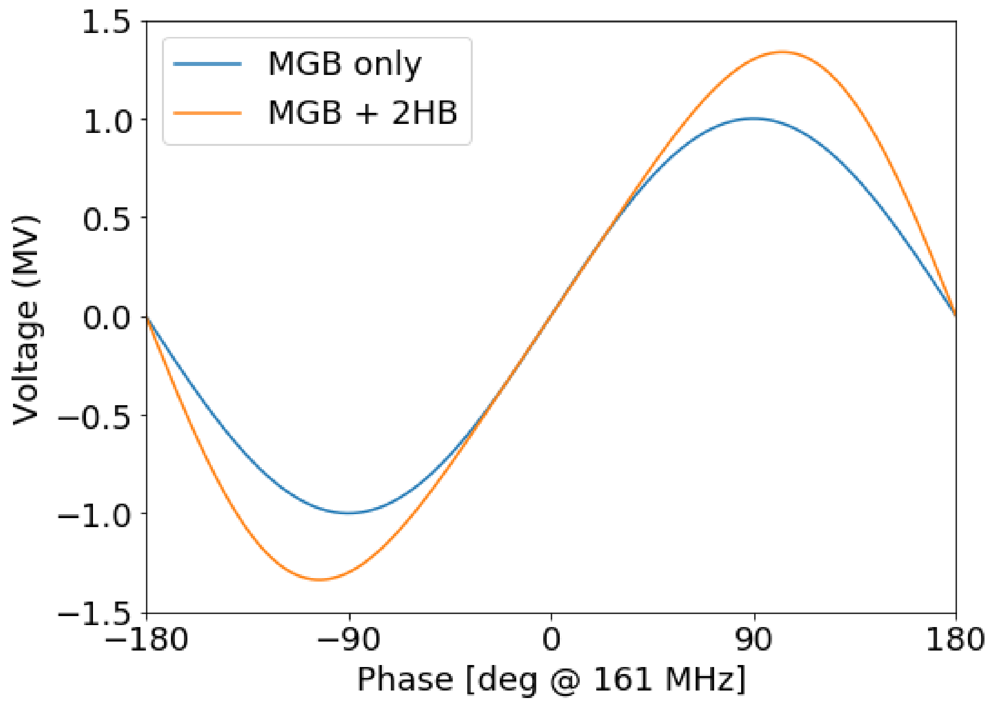

Figure 5.2: Effective bunching voltage waveforms.

5.1.1 Relative Locations

To reach the expected linearization, the 2HB has to be placed next to the MGB, either upstream or downstream of it. Approximating each cavity as an RF gap, two cases have been analyzed, one where the 2HB is located downstream of the MGB, called Configuration A, and one where the 2HB is located upstream of the MGB, called Configuration B. In both cases, the position of the MGB is the same.

Assume z_1 is the distance between a given beam particle and the beam reference particle and $z_1' = \frac{\Delta p}{p}$ is the relative momentum difference between them at the first cavity entrance.

In the case of configuration A, the particle coordinates are:

$$\begin{aligned} z_2 &= z_1 \\ \phi_2 &= -\frac{\omega z_2}{v} \\ z_2' &= k_{MGB} \cdot \sin(\phi_2) + z_1' \end{aligned} \tag{5.1}$$

where k_{MGB} depends on the effective voltage of the MGB, $\omega = 2\pi f_{RF}$, f_{RF} is 161 MHz, and v is the velocity of the particle. Next, L_1 is taken into account, the distance between the MGB and 2HB, which means at the 2HB entrance, the particle coordinates are:

$$\begin{aligned} z_3 &= z_2 + \frac{L_1}{\gamma^2} \cdot z_2' \\ z_3' &= z_2' \end{aligned} \tag{5.2}$$

where γ is the relativistic factor of the particle. After debunching by the 2HB, the longitudinal coordinates look like:

$$\begin{aligned} z_4 &= z_3 \\ \phi_4 &= -\frac{\omega z_4}{v} \\ z_4' &= k_{2HB} \cdot \sin(-2 \cdot \phi_4) + z_3' \end{aligned} \tag{5.3}$$

where k_{2HB} depends on the effective voltage of the 2HB. Now if ϕ_1 and z_1' are substituted into Eqn. 5.3, then:

$$\begin{aligned} z_4 &= z_1 + \frac{L_1}{\gamma^2} \cdot (z_1' + k_{MGB} \cdot \sin\left(\frac{-\omega z_1}{v}\right)) \\ z_4' &= k_{MGB} \cdot \sin\left(\frac{-\omega z_1}{v}\right) + z_1' + k_{2HB} \cdot \sin\left(\frac{2\omega}{v} z_4\right) \end{aligned} \tag{5.4}$$

For Configuration B, where the 2HB is located upstream of the MGB, the longitudinal coordinates of a particle after debunching by the 2HB are:

$$
\begin{aligned}
z_2 &= z_1 \\
\phi_2 &= -\frac{\omega z_2}{v} \\
z_2' &= k_{2HB} \cdot \sin\left(-2 \cdot \phi_2\right) + z_1'
\end{aligned} \tag{5.5}
$$

Next, at the MGB entrance:

$$
\begin{aligned}
z_3 &= z_2 + \frac{L_1}{\gamma^2} \cdot z_2' \\
z_3' &= z_2'
\end{aligned} \tag{5.6}
$$

Then, after bunching by the MGB:

$$
\begin{aligned}
z_4 &= z_3 \\
\phi_4 &= -\frac{\omega z_4}{v} \\
z_4' &= k_{MGB} \cdot \sin\left(\phi_4\right) + z_3'
\end{aligned} \tag{5.7}
$$

Finally, after substituting initial coordinates:

$$
\begin{aligned}
z_4 &= z_1 + \frac{L_1}{\gamma^2} \cdot (k_{2HB} \cdot \sin\left(\frac{2\omega z_1}{v}\right) + z_1') \\
z_4' &= k_{2HB} \cdot \sin\left(\frac{2\omega z_1}{v}\right) + z_1' + k_{MGB} \cdot \sin\left(\frac{-\omega}{v} z_4\right)
\end{aligned} \tag{5.8}
$$

Although, the coefficient of the Fourier series of the sawtooth wave may provide the basic estimate for the k_{2HB} to k_{MGB} effective voltage ratio, its optimal value depends on the bunch length or, more general, on the longitudinal density distribution of the bunch. For both configurations, the values of k_{2HB} and k_{MGB} are found that minimizes the root mean square (rms) value of z'_4 in the beam, which is calculated by this equation:

$$z'_{rms} = \sqrt{\frac{1}{N}\sum_{i}^{N} z'^2} \tag{5.9}$$

Since this optimization problem using Eq. 4 and 8 cannot be solved in a simple analytical form, a code has been created that uses the Nelder-Mead method to numerically minimize rms z'_4 and return the optimum ratio of k_{2HB} to k_{MGB} for a given macroparticle distribution. Although minimization of Eqn. 5.9 does not cover all possible matching conditions to the following accelerating segment, the requirement of minimized momentum spread is common for most of the tunes.

For the model, a beam energy of 16.5 MeV/u and varying initial beam sizes are assumed for two cases: one where the longitudinal distribution of the beam is assumed as a simple line representing the dp/p axis of the CS ellipse of the beam focused on the stripper, and one with a two dimensional Gaussian distribution and the results were compared and shown in Fig. 5.3.

The optimal voltage ratio increases similarly with both line and Gaussian distributions. When the initial rms dW/W is greater than 0.004, the voltage ratio increases at a higher rate for the line model in both configurations. This is because there are more particles located in the "tails" in the line models, so more voltage is required for the 2HB to linearize the distribution. The Gaussian model has a higher fraction of particles in the "core" of the distribution and less particles in the tails.

For both beam distributions, the fields of both cavities are higher in the case where the 2HB is located upstream of the MGB because of time-of-flight effects in the drift space between the cavities. If the beam enters the MGB first, it is bunched longitudinally, then the

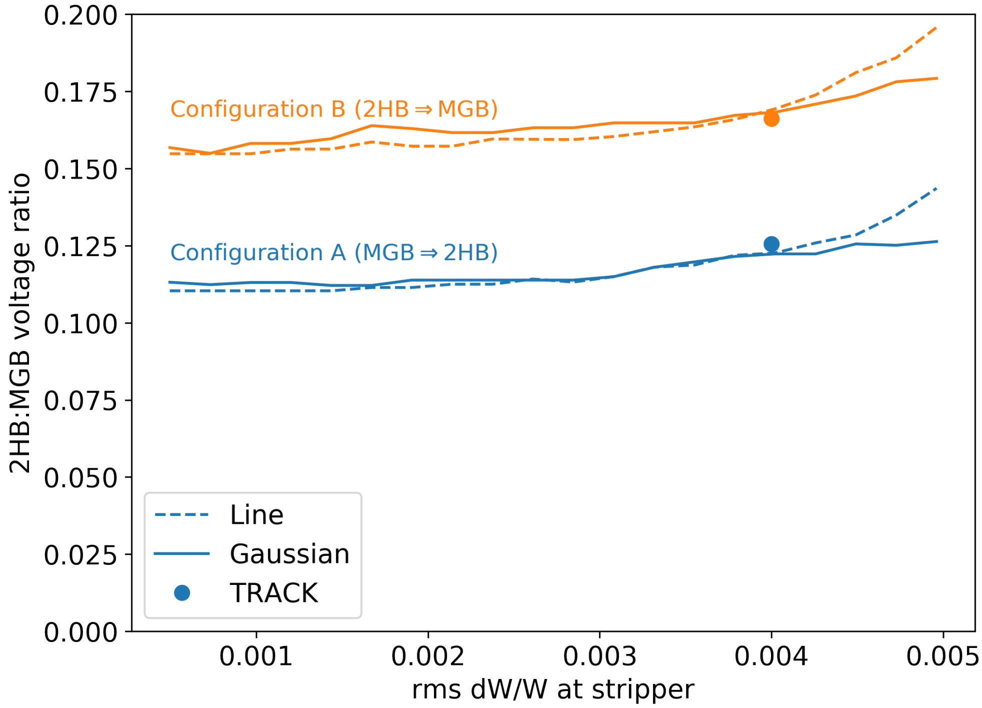

Figure 5.3: Ratio of 2HB voltage to MGB voltage that minimizes rms energy spread for various initial beam energy spreads.

beam size continues to decrease between the MGB and 2HB. However, if the beam enters the 2HB first, it is de-bunched longitudinally because the 2HB is phased opposite to the MGB, then the beam size increases before reaching the MGB, thus requiring higher voltages in both cavities to make the beam "flat" in longitudinal phase space.

Figure 5.4 shows the relative increase in MGB effective voltage for the Gaussian beam simulations for both configurations compared to the current configuration with the MGB only. The addition of the second harmonic means the effective voltage on the MGB must be increased to extend the linear region of the total effective bunching voltage waveform. It can be seen from Fig. 5.4 that Configuration B requires a larger MGB effective voltage compared to Configuration A, due to the time-of-flight effects described previously, which means that the beam size is larger at the MGB for Configuration B compared to Configuration A.

These results were compared to simulations with the particle tracking code TRACK [12]

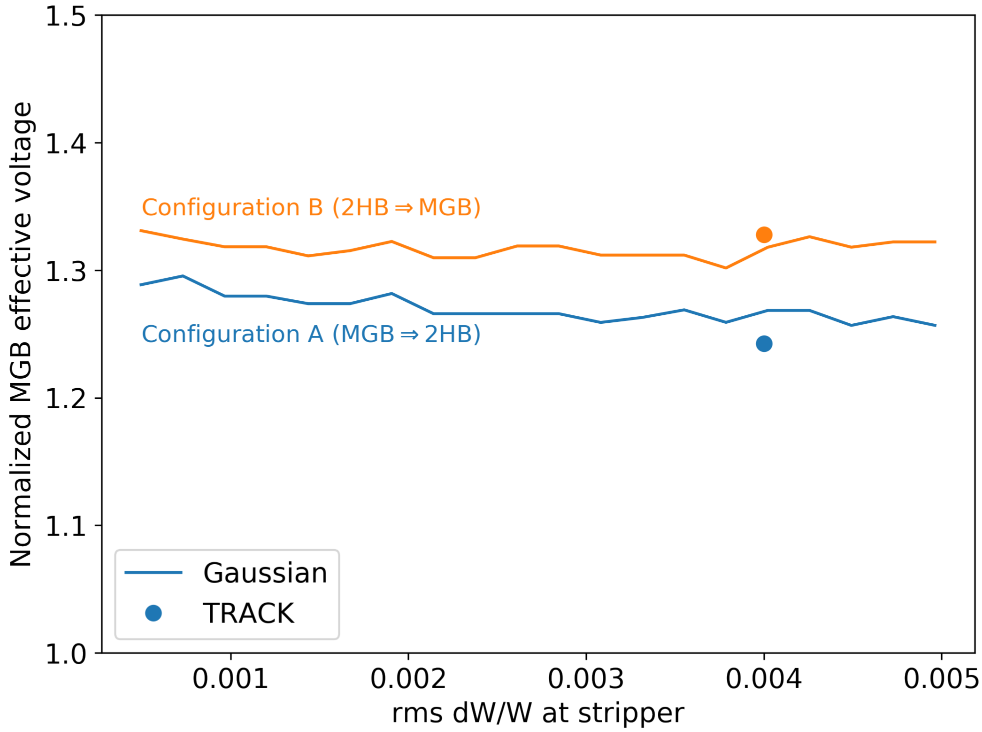

Figure 5.4: MGB effective voltages from calculations in Fig. 5.3 normalized to simulation using only MGB to minimize rms energy spread.

for a realistic case of a 16.5 MeV/u $^{238}U^{75+}$ beam. The MGB and 2HB effective voltages calculated by TRACK are described in Table 5.1. As shown in Table 5.1, when the 2HBs are upstream of each MGB, the 2HBs require 40 % more voltage and the MGBs require 7 % more voltage compared to the case when the 2HBs are located downstream of each MGB. These results, displayed as dots in Figs. 5.3 and 5.4, match the results calculated with the numerical RF gap model. The optimum layout of the MGB and 2HB can be seen in Fig. 5.5.

Table 5.1: Voltages for a $^{238}U^{75+}$ beam at 16.5 MeV/u

Cavity	2HB Downstream Voltage (kV)	2HB Upstream Voltage (kV)
MGB01	1019	1089
2HB1	128	181
MGB02	608	652
2HB2	76	105

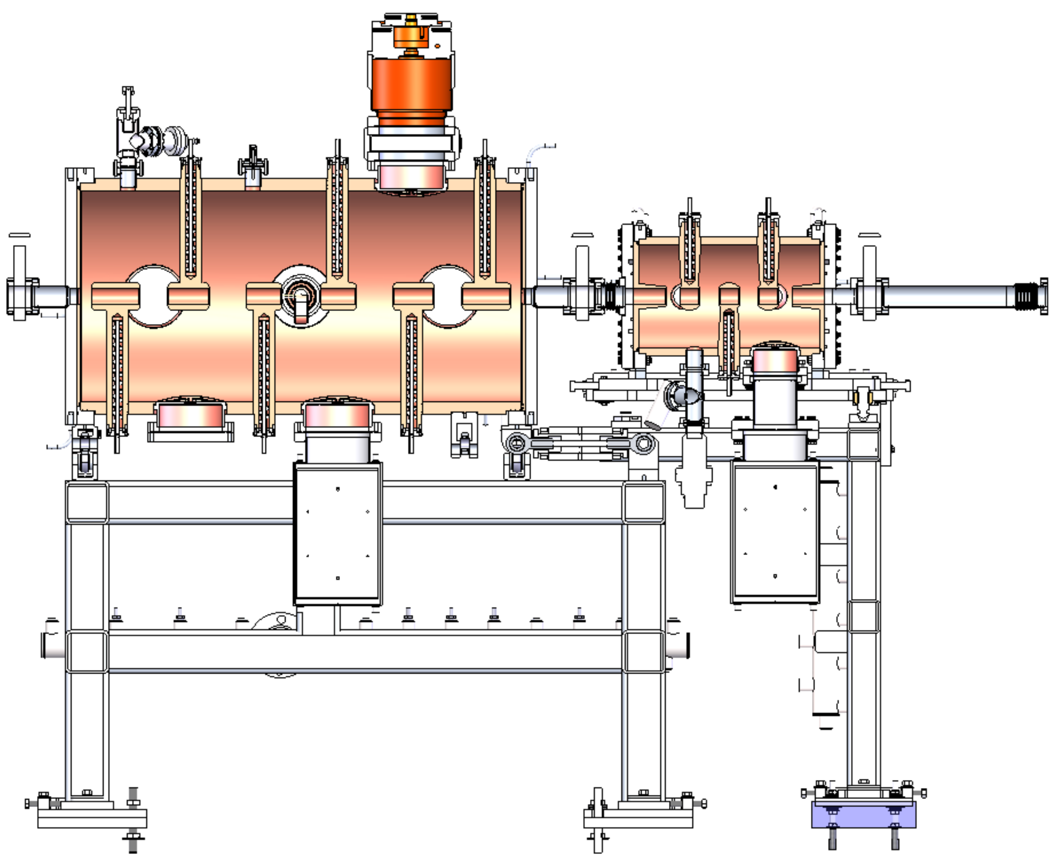

Figure 5.5: Cross-section view of MGB (left) and 2HB (right).

5.1.2 Number of 2HBs

We examined the effect of building only one 2HB and installing it downstream of MGB01 versus the effect of building two 2HBs and installing them downstream of each MGB. TRACK was used to simulate the longitudinal acceptance from the lithium stripper to the end of LS2 for three cases: no 2HBs added, one 2HB added downstream of MGB01, and two 2HBs added: one downstream of MGB01 and the other downstream of MGB02. The results can be seen in Fig. 5.6. From these plots, it is apparent that while installing one 2HB leads to a significant increase in energy acceptance, the highest energy acceptance is achieved when two 2HBs are installed.

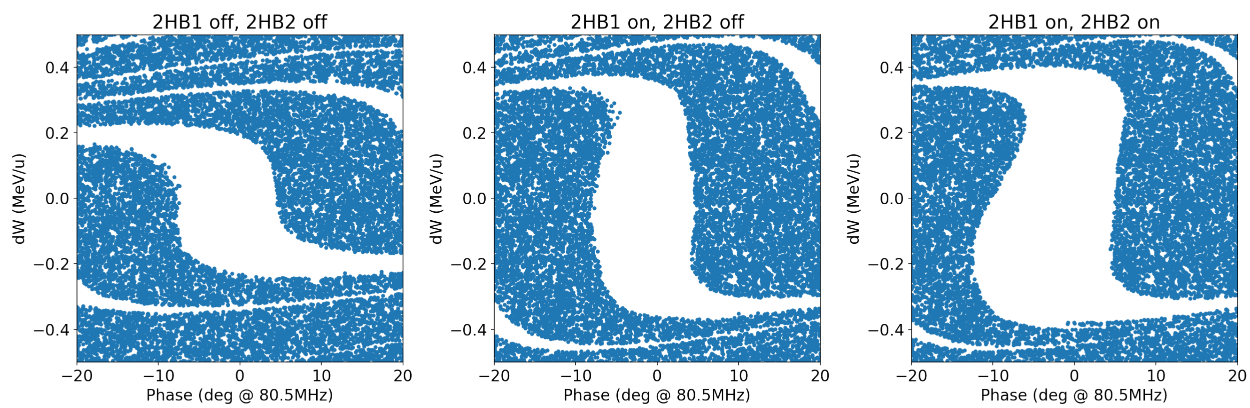

Figure 5.6: Longitudinal acceptance from stripper to end of LS2.

The linearizing effect of the second harmonic can be directly seen in Fig. 5.7. To clearly demonstrate the effects of the new cavities, an artificial beam distribution with an exaggerated energy spread was created at the stripper and simulated with TRACK from the stripper to the entrance of LS2, with snapshots of the longitudinal distribution taken at the exit of 2HB1 and 2HB2. In the left plot, when 2HB1 is on, there are much fewer particles in the non-linear "tails" on the edges of the beam distribution compared to the case when 2HB1 is off. In the right plot, the distribution with the largest linear region is when both second harmonic bunchers are activated. In Fig. 5.8, it can be seen that when both 2HBs are activated, all macroparticles in the simulation fit inside the longitudinal acceptance of LS2, whereas some macroparticles are lost in the other cases. This further validates the decision to build and install two 2HBs.

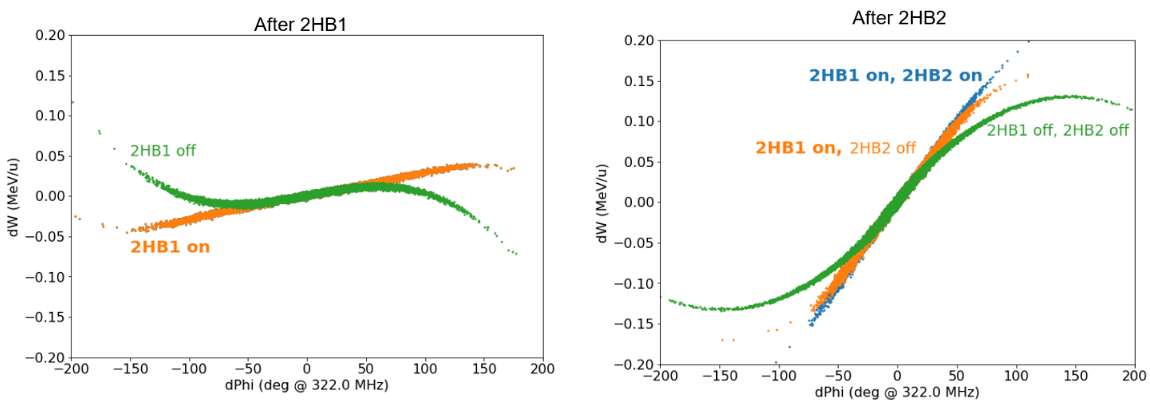

Figure 5.7: Longitudinal beam distribution with exaggerated energy spread after 2HB1 (left) and 2HB2 (right).

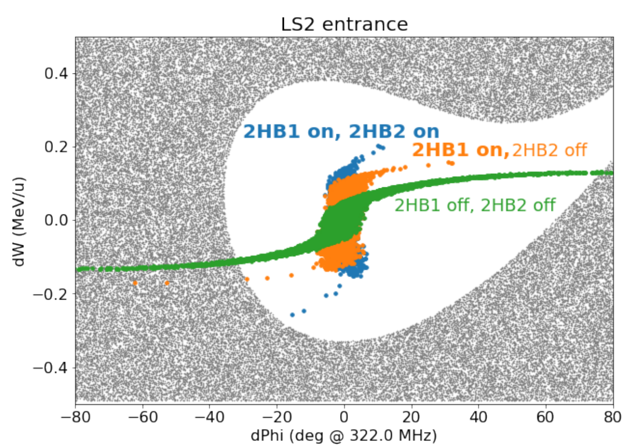

Figure 5.8: Longitudinal beam distribution with exaggerated energy spread at LS2 entrance and LS2 longitudinal acceptance.

5.2 RF Design

The cavity design process was started by using CST Studio [35] to design six different types of room temperature 322 MHz cavities, including Half-Wave Resonator (HWR), Quarter-Wave Resonator (QWR), and Spoke. Ultimately, a 4-gap Interdigital H-type (IH) cavity [36] was chosen because of the low RF power consumption and the fact that we have experience building IH-type cavities, as the MGBs are 7-gap IH-type cavities [31]. During the design process, electromagnetic, thermal, and mechanical simulations were performed to optimize RF power consumption, temperature change, and mechanical stress.

The design effective voltage of the 2HB cavity was determined from TRACK simulations of a $^{238}U^{78+}$ beam because it is the heaviest beam used at FRIB. Beam energies of 16.5 and 20.0 MeV/u were used for studies because those cover the range of realistic beam energies between the stripper and the LS2 entrance for all beam species. For each beam energy, the voltages of MGB01 and 2HB1 were adjusted to minimize the rms energy spread of the beam after 2HB1. Then the voltages of MGB02 and 2HB2 were adjusted to longitudinally focus the beam at the entrance of LS2. We added a margin of 10% higher than the highest voltage calculated to get a design effective voltage of 260 kV.

Table 5.2: 2HB Cavity Dimensions

Parameter	Value (mm)
Aperture diameter	36
Resonator inner length	423
Resonator inner diameter	24
Distance between stem centers	92
Tuner diameter	60

5.2.1 Electromagnetic Design

The length and radius of the cavity were chosen to reduce power consumption while keeping a resonant frequency of 322 MHz. There are three stems and drift tubes brazed to the tank. The length of the drift tubes and the gap between them were chosen to optimize power consumption. Relevant dimensions of the cavity are listed in Table 5.2. For ease of manufacturing, all three drift tubes and stems are identical. To further optimize power consumption, there will be a conical drift tube brazed to each end wall of the cavity. The edges of the drift tubes are rounded to reduce the peak surface electric field. The distribution of the surface electric field is shown in Fig. 5.9. The peak value is 8.27 MV/m which corresponds to 0.46 Kilpatrick and it is located at the edges of each drift tube. There are two tuners on the side wall of the cavity, one fixed and one motorized, and one coupler on the other side. The tuner and coupler design is the same as in the ReA buncher cavity [37]. Electromagnetic parameters of the cavity are listed in Table 5.3 and the longitudinal electric field along the beam axis is shown in Fig. 5.10.

Table 5.3: 2HB Cavity RF Parameters

Parameter	Value
Q factor	13000
Effective voltage (uranium beam)	260 kV
RF power (uranium beam)	4.6 kW
Peak surface E-field	0.46 Kilpatrick

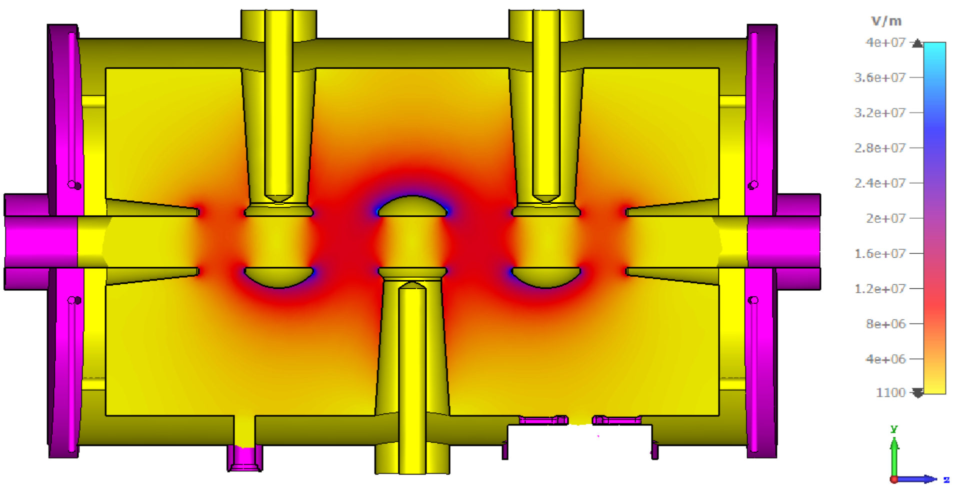

Figure 5.9: Cross-section view of the surface electric field distribution in the cavity.

As described in [31], the transit-time factor of the cavity can be calculated by Eqn. 1.13. The longitudinal electric field on axis is shown in Fig. 5.10. The transit time factor as a function of the beam energy can be seen in Fig. 5.11. The maximum transit time factor of 0.833 happens when the beam energy is 18.85 MeV/u. This is in between 16.5 and 20 MeV/u, the two most common beam energies at this cavity. It is closer to 20 MeV/u to optimize the RF power consumption for both energies, as the beam rigidity is higher at 20 MeV/u compared to 16.5 MeV/u.

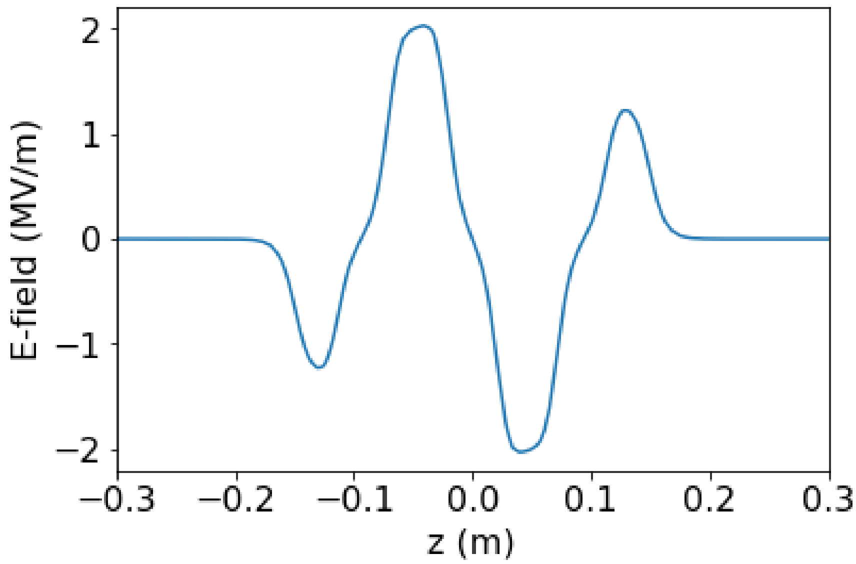

Figure 5.10: Longitudinal electric field distribution on the z-axis of the cavity.

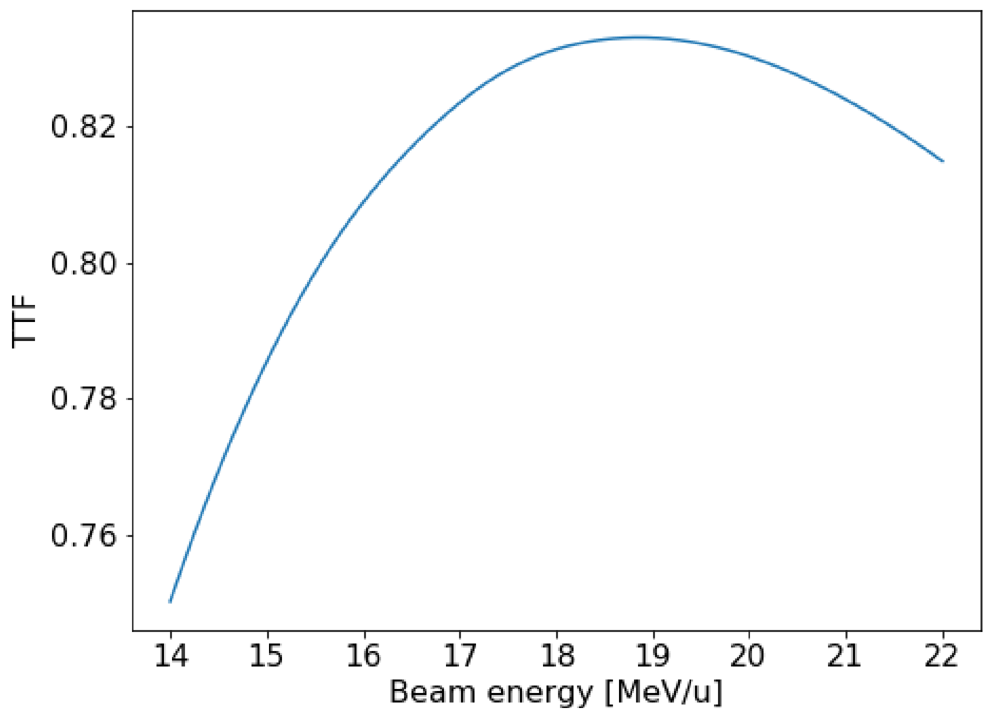

Figure 5.11: Transit time factor as a function of beam energy.

5.2.2 Thermomechanical Design

The tank, end walls, drift tube stems, tuners, and coupler are water-cooled. The stems are cooled with a threaded cooling channel. The temperature of the water is 20°C. Figure 5.12 shows the inside of the cavity along with the temperature change when the cavity is at design voltage of 260 kV. The highest temperature change inside the cavity is 38 K located on the central drift tube because of the high electric fields in both central gaps as seen in Fig. 5.9.

The mechanical stress on each component of the cavity was analyzed as shown in Fig. 5.13. The maximum stress inside the cavity is located at the intersection of the stem of the central drift tube and the cavity body, with a value of 10 MPa, well under the yield strength of 63 MPa [38]. Although difficult to see in Fig. 5.12, there exists a temperature gradient up to 15 K around this brazing zone of the central drift stem. This causes the mechanical stress shown in Fig. 5.13 in that area. In the brazing zones of the two outer drift tubes, there exists mechanical stress with half the magnitude of the central drift tube caused by a temperature gradient that is half of that in the central drift tube brazing zone. The radii of the drift tube stems were increased to reduce mechanical stress.

5.3 Design Finalization

Figure 5.14 shows the results of an analysis performed in CST, where both tuners were moved at once and the change in the resonant frequency of the cavity was checked. Next, a sensitivity analysis was performed, where 13 different parameters of the cavity were independently changed and the sensitivity of the cavity frequency to each of these parameters

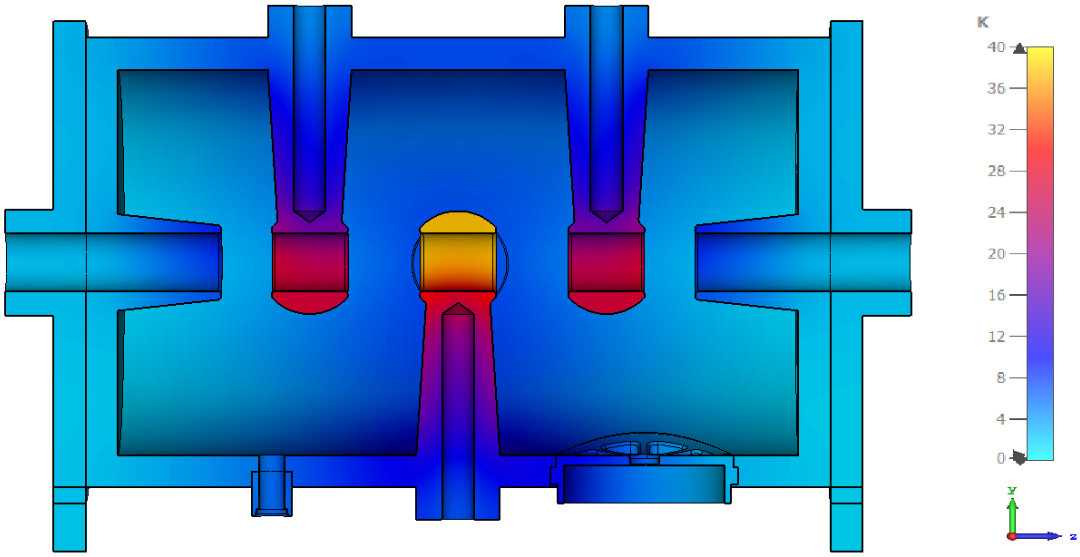

Figure 5.12: Cross-section view of the cavity with dimensions and temperature change at design voltage.

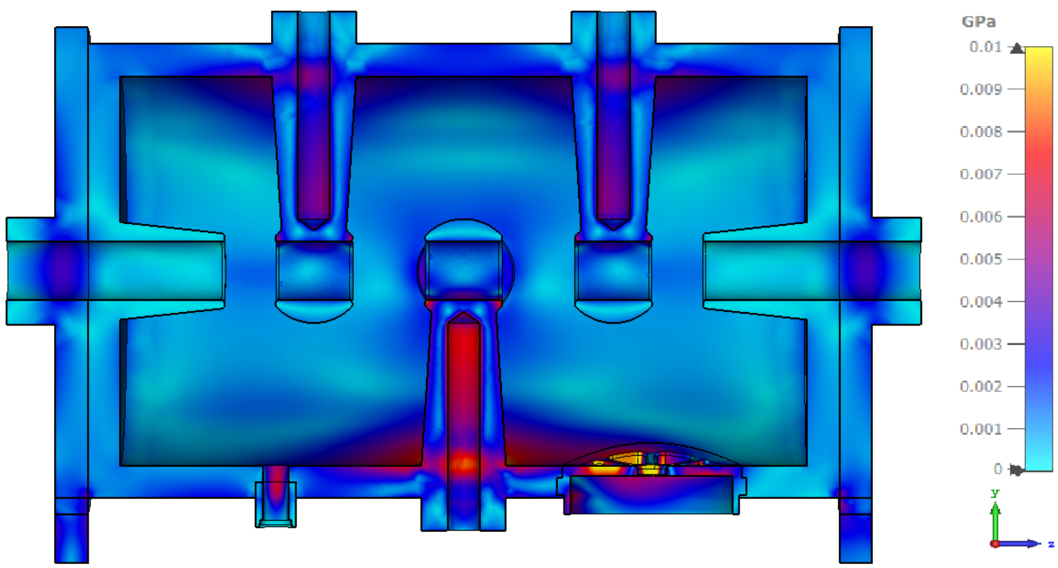

Figure 5.13: Cross-section view of the cavity with mechanical stress at design voltage.

was calculated. Those results are shown in Table 5.4.

Using these numbers, a Monte Carlo simulation was performed to ensure the frequency range of the tuners could cover the combined errors. In each error calculation, a random relative error for each parameter listed in Table 5.4 was generated from a Gaussian distribution assuming a mean of 0 and a standard deviation of 0.001. The frequency change

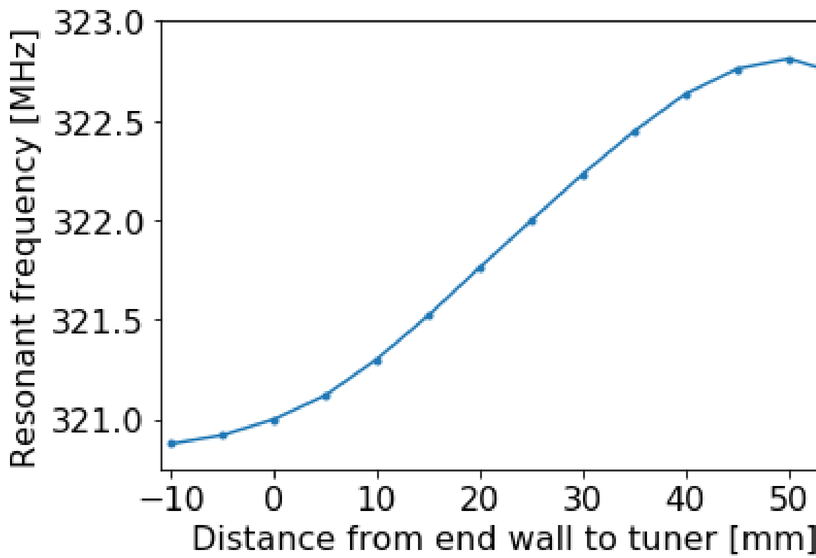

Figure 5.14: Cross-section view of the cavity with mechanical stress at design voltage.

corresponding to each parameter error was then calculated and summed up to calculate a total frequency shift. After 100,000 simulations, the total frequency shift of each one is displayed as a histogram in Fig. 5.15 The standard deviation of the frequency shift is 250 kHz.

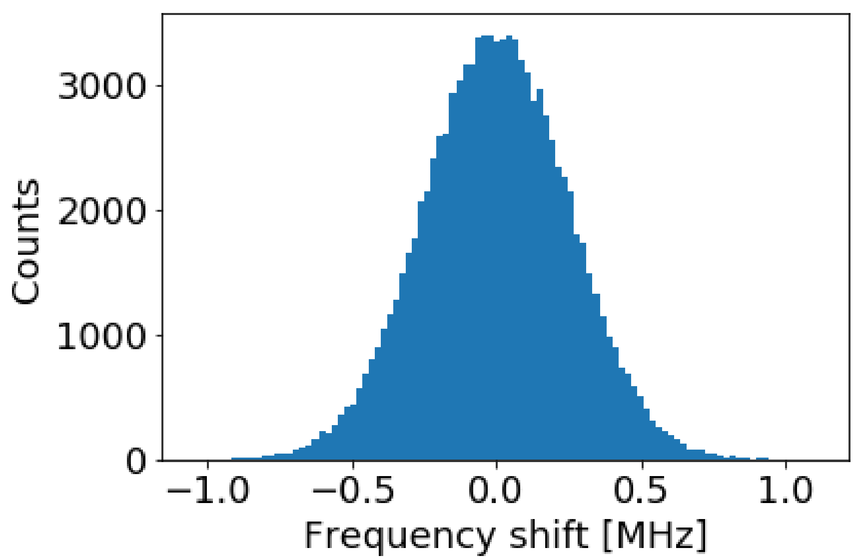

Figure 5.15: Total frequency shift due to mechanical errors in the dimensions of the 2HB cavity.

The tuning range is 1.8 MHz or 0.9 MHz on each side, so it can compensate ±3 standard

Table 5.4: 2HB Sensitivity Analysis

Parameter	Sensitivity (MHz/mm)
Middle drift tube radius	-5.75
Bore concentricity	2.34
Cavity inner diameter	-1.28
Stem outer diameter	1.18
Gap length	0.86
Stem angle	0.68
End drift tube length	-0.24
Bore inner diameter	0.23
Middle drift tube length	-0.14
Cavity length	-0.07
End drift tube outer diameter	-0.05
Tuner outer diameter	0.04
End drift tube angle	0.02

deviations of the frequency shift calculated by these simulations.

The construction and installation of this cavity has been designated as high priority in the FRIB Accelerator Improvement Plan. Our goal is to install the cavity in Summer 2026. We have been working with FRIB mechanical engineers to finalize the mechanical design of the cavity and begin the procurement process.

Chapter 6. Extension of Scientific Reach of ReA

As described in Section 1.1.2.2, ReA is a SRF linear accelerator that was commissioned in 2015 as ReA3. ReA “re-accelerates” stopped rare isotopes produced in the FRIB high-power target or in a batch-mode ion source [7]. An electron beam ion trap [8] strips stopped rare isotopes from the charge state of 1+ to a charge state acceptable for ReA3, which can accelerate beams with an A/Q ratio between 2 and 5.

6.1 Time Structure of ReA Beams

ReA users request a clean 16.1 MHz beam structure for time-of-flight experiments. The 16.1 MHz multi-harmonic buncher combined with the 80.5 MHz RFQ produces a beam with four low-intensity (”satellite”) bunches with an 80.5 MHz structure in between each intense (”main”) bunch separated by 16.1 MHz. An RF chopper system has been designed that will vertically deflect the satellite bunches to be cleaned out by an aperture while keeping the main bunches on axis, as shown in Fig. 6.1.

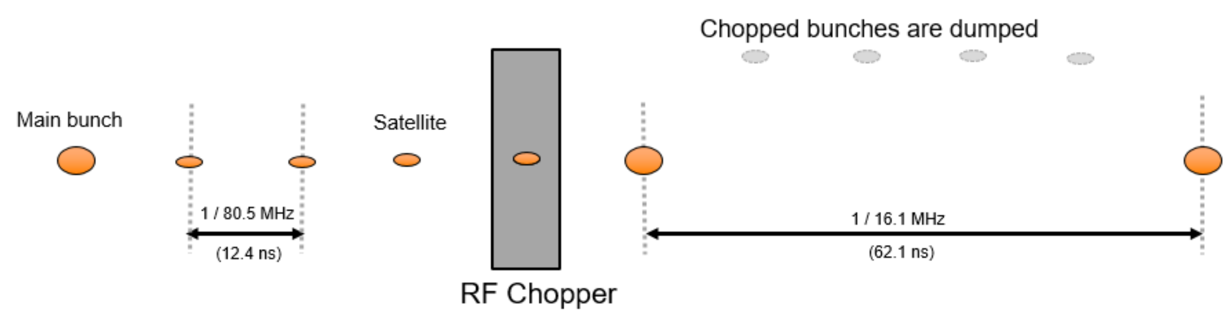

Figure 6.1: Bunch time structure of ReA.

6.2 Development of RF Chopper for ReA

Separator systems for CW beams typically solely rely on an RF electric field to split the beam [39]. Our proposed chopper system uses a combination of an RF electric field and a static magnetic field to deflect the satellite bunches while keeping the main bunches on axis in a similar way as was earlier proposed for an FRIB MEBT chopper system[40, 41]. The possibility of using only an RF electric field and phasing the cavity so the main bunches experience zero net deflection, similar to the CEBAF RF separator system [42] was explored. In this case, the chopper system would require double the voltage and four times the RF power to produce the same deflection compared to our design where the magnetic and electric fields contribute equally to the deflection of the bunches. Therefore, our approach is considered more efficient.

Two potential locations were considered for the chopper system. The first location, between the RFQ and the first ReA3 cryomodule (see Fig. 6.2), has a lower beam energy (0.5 MeV/u), but was not chosen because there is very limited space for the chopper system. The second location, shown in Fig. 6.2, is between the ReA3 cryomodules and the ReA6 cryomodule. The beam energy at this location is around 3 MeV/u. This location was chosen because there is plenty of space for both the chopper and a beam dump for the deflected satellite bunches. The beam dump will be located about 1.4 meters downstream of the chopper.

6.2.1 RF Design

The RF chopper design is based on a quarter-wave resonator cavity (QWR) with deflecting plates that kicks the beam bunches in a vertical direction [43, 44]. Other types of

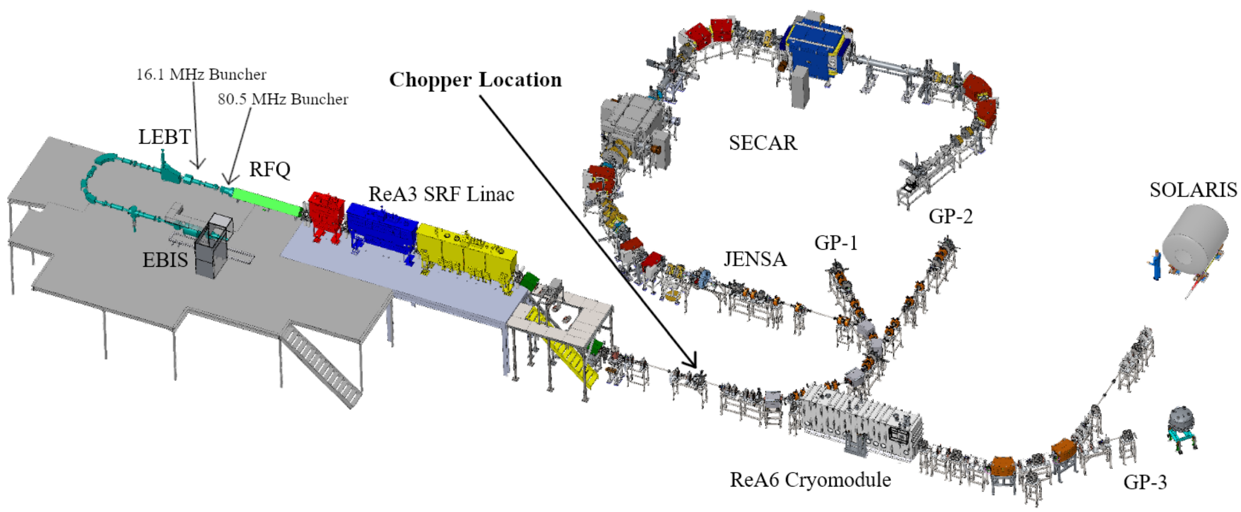

Figure 6.2: ReA layout.

cavities used for deflectors include a half-wave resonator and an H-type deflector[45]. QWR was chosen because it is the most compact of the deflector options. At FRIB, we are also familiar with the QWR mechanical design, as it is used as the design for the FRIB MEBT bunchers [46] and the ReA buncher [7].

The chopper design is shown in Fig. 6.3. The resonant frequency of the cavity is 64.4 MHz, which in combination with the bunch frequency of 80.5 MHz (driven by the RFQ frequency) produces a 16.1 MHz deflection waveform, see the bunches' pattern in Fig. 6.4. Indeed, the cavity resonates at the beat frequency of the actual bunch frequency and the desired 16.1 MHz bunch repetition rate. At 64.4 MHz, the QWR is a 1.1-meter-high cavity with a straight rigid inner conductor, whereas a 16.1 MHz resonator would require a coil inductor [47] and completely different mechanical design.

The optimum length of the plates is 168 mm, which corresponds to $L = 0.9 \cdot \beta\lambda/2$. This length was chosen to optimize RF power consumption by the cavity and is a trade-off between the gap capacitance and the deflection strength, as the largest deflection occurs when the length of the plates is equal to $\beta\lambda/2$. The vertical component of the electric field along the beam axis is shown in Fig. 6.5 and the electric field distribution inside the cavity is shown in Fig. 6.6.

To ensure all particles of the satellite bunches are intercepted by an aperture of 1 cm in radius located 1.4 m downstream of the chopper, the minimum required deflection of the satellite bunches is 14 mrad. The distance was chosen based on available space in the beamline. To reach the required kick, the amplitude of bunch deflection provided by the RF electric field must correspond to 21 mrad (see Fig. 6.4 and Fig. 6.7). These equations from Bongardt [48] were used to calculate the electric field amplitude required to produce this deflection:

$$x'_c(L) = x'_c(0) + f(L) \tag{6.1}$$

with

$$f(L) = \frac{-QeE}{Am\gamma\omega v_c}[\cos\left(\frac{\omega L}{v_c} + \phi\right) - \cos(\phi)] \tag{6.2}$$

$x'_c(L)$ is the vertical angle of the beam trajectory after passing through the deflector plates and $x'_c(0)$ is the initial vertical angle of the beam which is 0 in our case because all bunches are on the beam axis prior to the chopper. In Eq. 6.2: Q is the charge state of the ions in the beam, e is the elementary charge, A is the mass number of the ions in the beam, m is the atomic unit mass, γ is the Lorentz factor of the beam, v_c is the beam velocity, $\omega = 2\pi f$ where f is the cavity frequency, ϕ is the cavity phase with $\phi = 0$ producing the largest deflection, and E is the effective electric field strength. In our calculations and simulations, a beam with a charge-to-mass ratio of 1/4 and an energy of 3.0 MeV/u was used. ReA3 can accelerate beams with a charge-to-mass ratio of 1/5, but to a slightly lower energy [49], giving them about the same rigidity as our design beam.

By rearranging Eqns. 6.1 and 6.2, the electric field amplitude to produce a minimum required kick of 21 mrad can be calculated with

$$E = \frac{-x_c'(L)Am\gamma\omega v_c}{Qe}[\cos\left(\frac{\omega L}{v_c} + \phi\right) - \cos(\phi)]^{-1} \tag{6.3}$$

From this calculation, it was determined that the RF chopper requires an effective electric field strength of 4.7 MV/m. This field strength can be achieved with 10 kW of power. Figure 6.4 shows the kick waveform at this power level. The peak electric field inside an RF cavity is limited by electric breakdown. The Kilpatrick limit [9] at 64.4 MHz is 9.7 MV/m, and the peak electric field in the chopper system is 7.9 MV/m, which is 80% of this limit.

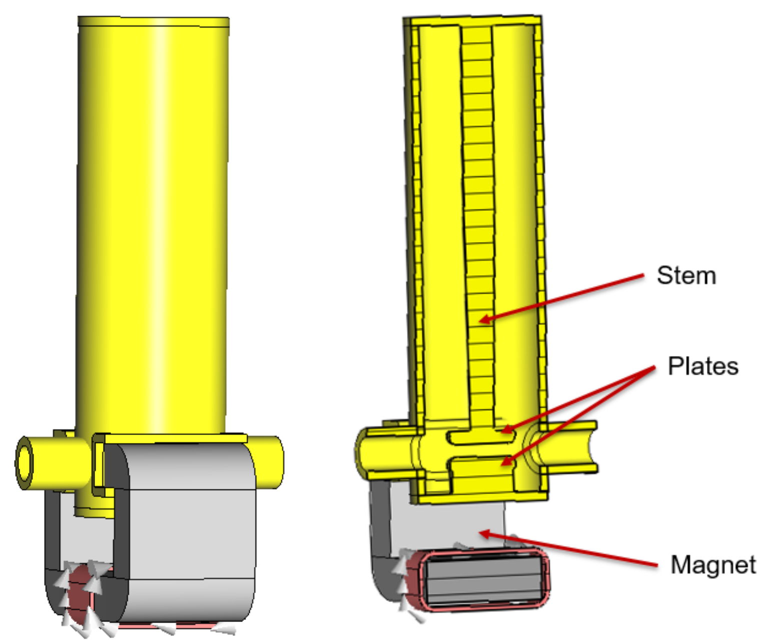

Figure 6.3: Full and cross-section views of the RF chopper cavity model designed in CST Studio (dimensions shown in Table 6.1).

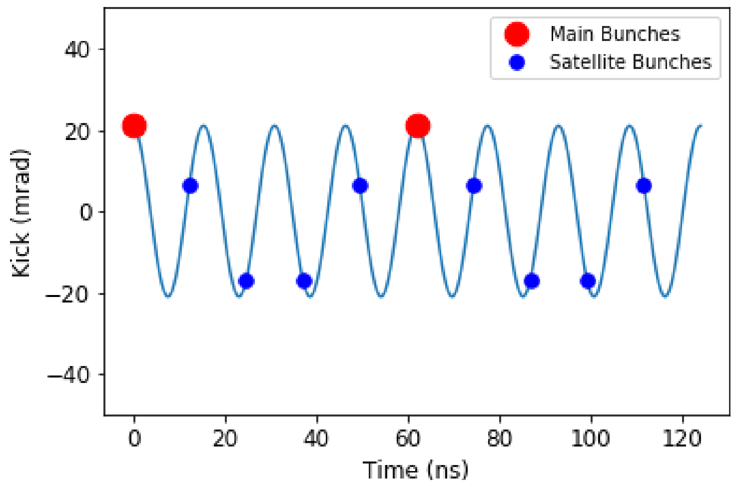

Figure 6.4: Average bunch deflection in the chopper due to the RF electric field overlaid onto a 64.4 MHz waveform with no magnetic bias.

6.2.2 Magnetic Bias

To keep the main bunches on axis, a static magnetic bias is needed to cancel out the deflection the main bunches feel from the RF electric field inside the cavity. The magnetic bias comes from an iron-dominated, C-shaped dipole.

To calculate the necessary magnetic field integral, the rigidity of the beam at the chopper is determined using Eqn. 1.14. Using a beam energy of 3 MeV/u and a charge-to-mass ratio of 1/4, the rigidity is calculated to be 1.0 T · m. To find the bending radius of the magnet, Eqn. 6.4 is used:

$$\rho = \frac{L_{eff}}{\theta} \tag{6.4}$$

where L_{eff} is the effective length of the magnet and θ is the deflection angle provided by the magnet, which must be 21 mrad to cancel out the peak deflection provided by the RF electric field. After combining Eqns. 4 and 5, the required magnetic field integral can be

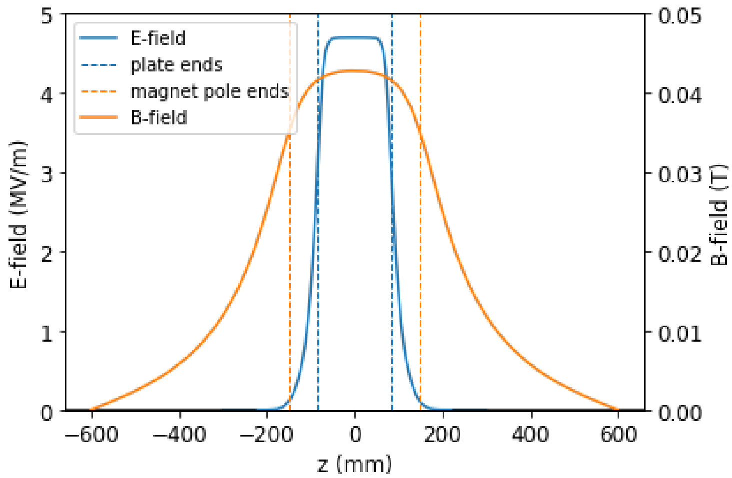

Figure 6.5: Chopper electric and magnetic fields along beam axis.

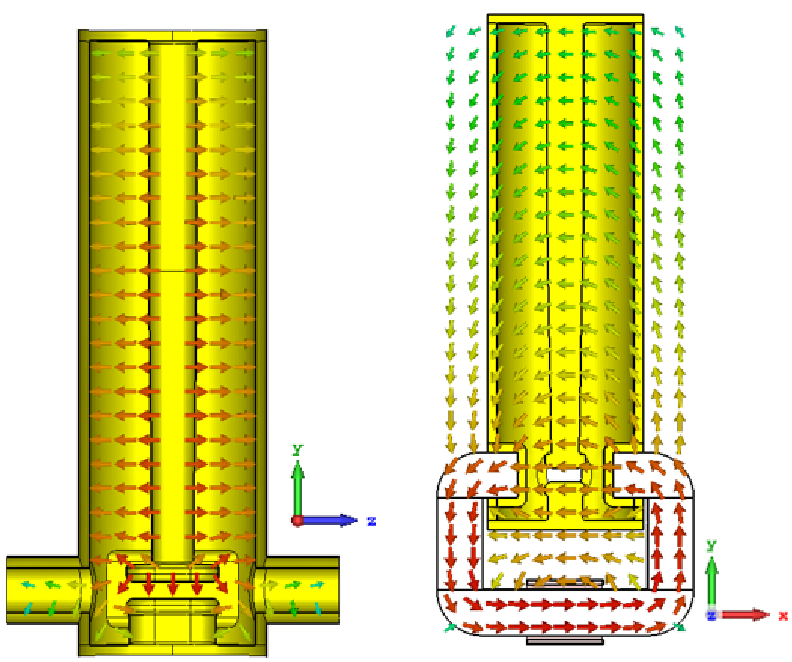

Figure 6.6: Chopper electric (left) and magnetic (right) field distributions.

found with Eqn. 6.5.

$$B_0 \cdot L_{eff} = \theta(B\rho) \tag{6.5}$$

This gives us a required magnetic field integral of 0.021 $\mathrm{T \cdot m}$. CST Studio [35] was used to design and simulate our magnet, varying current and number of turns in the coil until the required magnetic field integral was obtained. From these simulations, B_0, the field strength in the center of the magnet, was found to be 41.7 mT. The effective length of the magnet can then be calculated using Eqn. 6.6:

$$L_{eff} = \frac{\int B\, dl}{B_0} \tag{6.6}$$

This equation gives an effective length of 50.3 cm, compared to the geometrical length of 30 cm, which was chosen to fit on the diameter of the cavity.

The magnet is not very different from steering magnets used in accelerators [50]. It was designed assuming a coil current density of 10 $\mathrm{A/mm^2}$, which is common for water-cooled magnets. It uses 5 mm by 5 mm hollow copper wire with a hole diameter of 3 mm. It requires 65 turns with 195 A of current, which corresponds to a power of about 900 W. The magnetic field distribution inside the cavity and magnet is shown in Fig. 6.6.

The magnet is located on the cavity so the bunches can experience both the electric and magnetic deflections in the same space. If one magnet upstream and one magnet downstream of the cavity were used, then the bunches would enter the cavity already deflected off the beam axis, which requires a larger gap and higher voltage to achieve the required field strength. One magnet after the cavity would not work either because it cannot cancel out both offset and angle of the beam trajectory.

Figure 6.7 shows the effect of the magnetic field on the deflection of the bunches. The intense bunches are on the peak of the waveform and biased to zero kick, compared to the pure RF deflection case where they experience a deflection of 21 mrad. The trajectory angles of the satellite bunches are 14 mrad and 37 mrad and meet the required minimum deflection to be cleanly intercepted by the beam dump aperture.

Table 6.1: Important Design Parameters of the RF Chopper System

Parameter	Value	Unit
Cavity Height	1130	mm
Cavity Diameter	340	mm
Plate Length	168	mm
Gap Between Plates	30	mm
Electric Field in Gap	4.6	MV/m
Voltage in Gap	137	kV
Peak Electric Field	7.9	MV/m
RF Power	10	kW
Magnet Pole Tip Length	300	mm
Magnet Gap Length	184	mm
Magnetic Field Integral	0.021	$T \cdot m$
Peak Magnetic Field on axis	0.042	T
Magnet Power	900	W

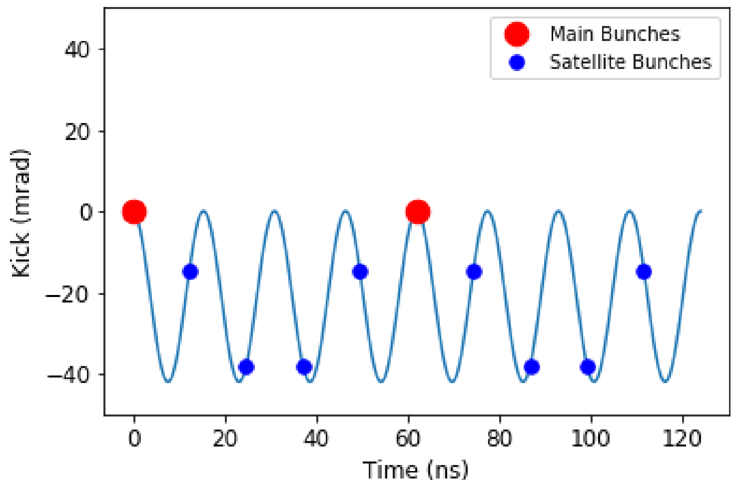

Figure 6.7: Average bunch deflection in the chopper due to the RF electric field combined with the static magnetic field provided by the chopper dipole overlaid onto a 64.4 MHz waveform.

6.2.3 Beam Dump

The satellite bunches are dumped on the beam pipe and on a circular aperture 1.4 meters downstream from the chopper. This distance was chosen because it is in between magnets on the beamline and also provides sufficient drift space for the satellite bunches to be deflected away from the main bunch. The aperture has a diameter of 2.0 cm, which allows all the particles in the main bunches to pass through and intercept the satellites before they reach the ReA6 cryomodule as shown in Fig. 6.8.

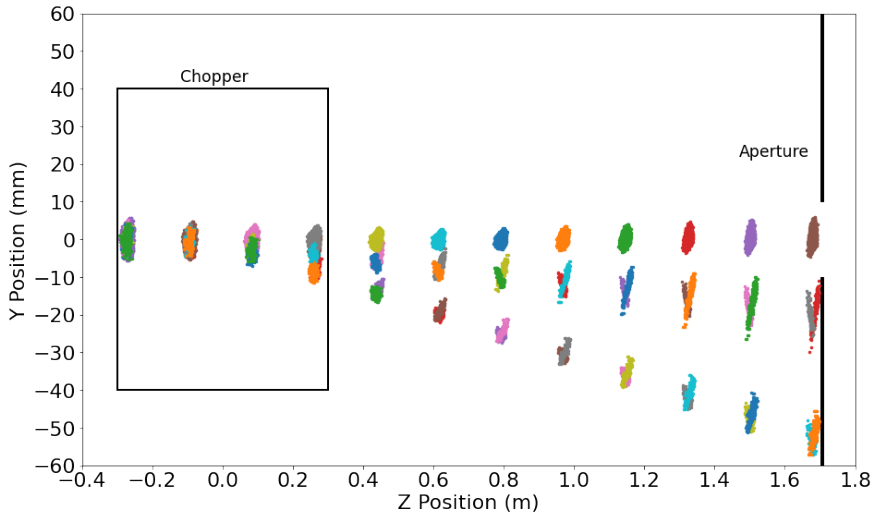

Figure 6.8: Snapshots of the simulated beam motion through the chopper, drift space, and the aperture. The time between each snapshot is one-half of an 80.5 MHz RF period (6.2 ns).

6.3 Beam Dynamics with and without RF Chopper

6.3.1 CST Studio

The 3D model of the chopper was constructed in CST Studio for the realistic simulation of beam motion in superimposed RF and magnetic fields. The initial particle distribution was exported from the beam dynamics model for the TRACK code [12] of the ReA beamline and imported into the CST PIC solver. The electric field inside the cavity was scaled to a level corresponding to 10 kW of input RF power and the magnetic field was adjusted to provide zero deflection for the main bunches. A snapshot of the bunches produced in CST can be seen in Fig. 6.8.

6.3.2 TRACK

In the ReA linac, TRACK [12] is the main code used to simulate beam dynamics from the ion source to the user stations. Currently, TRACK cannot simulate an RF electric field and a static magnetic field in the same element. To simulate the chopper system, the 3D RF electric field map of the chopper was imported from CST and then two zero-length dipole corrector elements on each side of the cavity were used to simulate the magnetic bias produced in the chopper. The results from these simulations are shown in Fig. 6.9. It can be seen in the y-y' plot after the chopper that the average kick of each bunch is the same as in the design waveform in Fig. 6.7 which results in a clean 16.1 MHz beam structure.

The satellite bunches are deflected downwards because in this case the longitudinal component of the electric field bunches the beam. If the electric field were reversed, deflecting the bunches upward, there would be a de-bunching effect on the beam. The longitudinal phase space plot after the chopper shows the effect of this longitudinal component of the electric field, which is located between the deflecting plates and the edges of the cavity. The average energy of the main bunch is unaffected, while the satellite bunches are decelerated or accelerated.

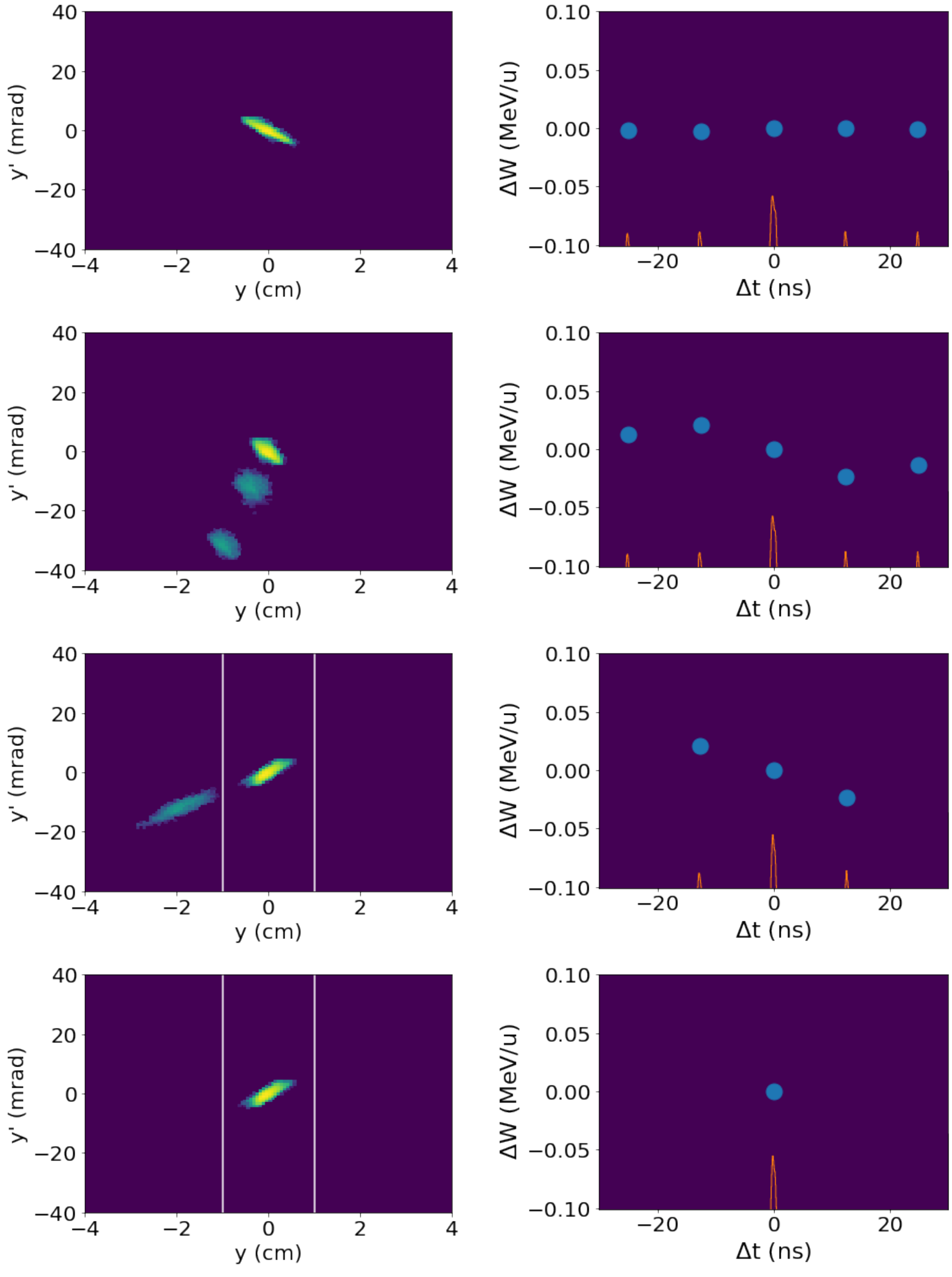

Figure 6.9: Y-Y' beam snapshots (left) and longitudinal bunch centroid positions (right) simulated by TRACK: before the chopper, after the chopper, before the beam dump, and after the beam dump (vertical lines represent the beam dump aperture size).

Chapter 7. Conclusion

These studies expand the scientific capabilities of both SRF linear accelerators at FRIB.

The development of an application to calculate synchronous phases of cavities helps FRIB accelerator physicists identify and fix changes in the RF calibration of cavities. IPS reliably works to set longitudinal tunes, but it relies on accurate and stable RF phase and amplitude calibrations, which can change due to a loose connector. The new application is much faster than the conventional 360-degree phasing of cavities and does not require downstream cavities to be off.

The multi-charge-state beam transport studies improved the accuracy of the FLAME model used to develop transverse tunes in the accelerator. The new, more accurate model will improve CS parameter matching and prevent losses at higher beam intensities. The improved model will also reduce beam tuning time if matching will not be necessary, as measuring CS parameters with quadrupole scans is one of the most time-intensive parts of the primary beam development process.

The velocity equalizer will increase transmission through the RFQ for two-charge-state beams. The 40.25 MHz resonator is designed to kick both charge states to an equal average velocity. The biased drift tube will separate them in time by one RF period at the RFQ entrance. This will double beam intensity for heavy-ion beams, making it a key component of the FRIB power ramp-up process.

The 322 MHz room-temperature buncher cavity will help to mitigate beam losses caused by energy straggling and non-uniformities in the liquid lithium charge stripper. The design of the cavity is feasible and similar to the FRIB Multi-Gap Buncher design. The construction and installation of this cavity has been designated as high priority in the FRIB Accelerator

Improvement Plan.

The ReA chopper uses a combination of an RF electric field and a static magnetic field to vertically deflect low-intensity satellite bunches, while keeping the main 16.1 MHz bunches on the beam axis. A similar design could be used to create a 20.125 MHz bunch structure in the FRIB driver linac. The design was validated by simulations in both TRACK and CST Studio. The ReA chopper will provide users the ability to perform time-of-flight measurements with a 16.1 MHz beam bunch structure.

The research presented in this thesis contributes to FRIB reaching its full potential as a world-class nuclear physics research facility.

BIBLIOGRAPHY

[1] A. Gade, C. K. Gelbke, and T. Glasmacher, "NSCL and the Facility for Rare Isotope Beams (FRIB) project," *Nuclear Physics News*, vol. 24, no. 1, pp. 28–30, 2014.

[2] T. Glasmacher, A. Gade, G. Bollen, and J. Wei, "The Facility for Rare Isotope Beams: Providing new opportunities for science," *Nuclear Physics News*, vol. 34, no. 3, pp. 5–12, 2024.

[3] P. N. Ostroumov and J. Wei, "First two years of FRIB operation," in *Proc. LINAC'24*, no. 32 in Linear Accelerator Conference, pp. 278–283, JACoW Publishing, Geneva, Switzerland, Aug. 2024.

[4] G. Machicoane, M. Doleans, O. Kester, E. Pozdeyev, T. Ropponen, L. Sun, E. Tanke, X. Wu, and D. Leitner, "ECR Ion Sources for the Facility for Rare Isotope Beams (FRIB) Project at Michigan State University," in *Proc. ECRIS'10*, pp. 14–16, JACoW Publishing, Geneva, Switzerland, 2010.

[5] J. P. Holzbauer, W. Hartung, F. Marti, Q. Zhao, and E. Pozdeyev, "Electromagnetic Design of a Multi-harmonic Buncher for the FRIB Driver Linac," in *Proc. PAC'11*, no. 24 in Particle Accelerator Conference, pp. 1000–1002, JACoW Publishing, Geneva, Switzerland, Sept. 2011.

[6] N. Bultman, E. Pozdeyev, G. Morgan, Q. Zhao, Y. Yamazaki, L. M. Young, and J. Stovall, "Design of the FRIB RFQ," in *Proc. IPAC'13*, pp. 2866–2868, JACoW Publishing, Geneva, Switzerland, May 2013.

[7] A. C. C. Villari, B. Arend, G. Bollen, D. B. Crisp, K. D. Davidson, K. Fukushima, A. I. Henriques, K. Holland, S.-H. Kim, A. Lapierre, *et al.*, "ReAccelerator Upgrade, Commissioning and First Experiments at the National Superconducting Cyclotron Laboratory (NSCL) / Facility for Rare Isotope Beams (FRIB)," in *Proc. 13th International Particle Accelerator Conf. (IPAC '22)*, 2022.

[8] A. Lapierre, G. Bollen, D. Crisp, S. W. Krause, L. E. Linhardt, K. Lund, S. Nash, R. Rencsok, R. Ringle, S. Schwarz, *et al.*, "First two operational years of the electron-beam ion trap charge breeder at the National Superconducting Cyclotron Laboratory"," *Physical Review Accelerators and Beams*, vol. 21, p. 053401, 2018.

[9] T. P. Wangler, *RF Linear Accelerators.* Wiley, 2007.

[10] E. Courant and H. Snyder, "Theory of the alternating-gradient synchrotron," *Annals of Physics*, vol. 281, no. 1, pp. 360–408, 2000.

[11] F. Plassard, *Optics optimization of longer L* Beam Delivery System designs for CLIC and tuning of the ATF2 final focus system at ultra-low β* using octupoles.* Theses, Université Paris Saclay (COmUE), Jul 2018.

[12] P. N. Ostroumov, V. Aseev, and B. Mustapha, "TRACK – a code for beam dynamics simulation in accelerators and transport lines with 3D electric and magnetic fields." http://www.phy.anl.gov/atlas/TRACK, 2006.

[13] Z. He, Y. Zhang, J. Wei, Z. Liu, and R. M. Talman, "Linear envelope model for multicharge state linac," *Phys. Rev. ST Accel. Beams*, vol. 17, p. 034001, Mar 2014.

[14] P. N. Ostroumov, O. B. Tarasov, N. Bultman, F. Casagrande, Y. Choi, S. Cogan, M. Cortesi, K. Fukushima, A. Gonzalez, J. Guo, *et al.*, "Acceleration of uranium beam to record power of 10.4 kW and observation of new isotopes at Facility for Rare Isotope Beams," *Phys. Rev. Accel. Beams*, vol. 27, 2024.

[15] P. N. Ostroumov, K. Fukushima, T. Maruta, A. S. Plastun, J. Wei, T. Zhang, and Q. Zhao, "First simultaneous acceleration of multiple charge states of heavy ion beams in a large-scale superconducting linear accelerator," *Phys. Rev. Lett.*, vol. 126, p. 114801, Mar 2021.

[16] P. N. Ostroumov, R. C. Pardo, G. P. Zinkann, K. W. Shepard, and J. A. Nolen, "Simultaneous acceleration of multiply charged ions through a superconducting linac," *Phys. Rev. Lett.*, vol. 86, pp. 2798–2801, Mar 2001.

[17] T. Kanemura, M. LaVere, R. Madenorp, F. Marti, T. Maruta, Y. Momozaki, P. N. Ostroumov, A. S. Plastun, J. Wei, and Q. Zhao, "Experimental demonstration of the thin-film liquid-metal jet as a charge stripper," *Phys. Rev. Lett.*, vol. 128, 2022.

[18] T. Kanemura, N. Bultman, M. LaVere, R. Madendorp, F. Marti, T. Maruta, Y. Momozaki, J. A. Nolen, P. N. Ostroumov, A. S. Plastun, *et al.*, "R&D of Liquid Lithium Stripper at FRIB," in *Proc. LINAC'22*, no. 31 in International Linear Accelerator Conference, pp. 668–672, JACoW Publishing, Geneva, Switzerland, Oct. 2022.

[19] E. Segre, *Nuclei and Particles.* W. A. Benjamin, Inc., 1965.

[20] R. Evans, *The Atomic Nucleus.* McGraw-Hill, 1955.

[21] J. F. Ziegler, M. Ziegler, and J. Biersack, "Srim the stopping and range of ions in matter (2010)," *Nuclear Instruments and Methods in Physics Research Section B: Beam Interactions with Materials and Atoms*, vol. 268, no. 11, pp. 1818–1823, 2010.

[22] A. S. Plastun, P. N. Ostroumov, A. C. C. Villari, and Q. Zhao, "Longitudinal Beam Dynamics in FRIB and ReA Linacs," in *Proc. ICAP'18*, pp. 330–334, JACoW Publishing, Geneva, Switzerland, Oct. 2018.

[23] P. N. Ostroumov, S. Cogan, K. Fukushima, S. Lidia, T. Maruta, A. S. Plastun, J. Wei, J. Wong, T. Yoshimoto, and Q. Zhao, "Heavy ion beam acceleration in the first three cryomodules at the facility for rare isotope beams at michigan state university," *Phys. Rev. Accel. Beams*, vol. 22, p. 040101, Apr 2019.

[24] A. S. Plastun and P. N. Ostroumov, "Instant Phase Setting in a Large Superconducting Linac," in *Proc. NAPAC'22*, North American Particle Accelerator Conference, pp. 885–890, JACoW Publishing, Geneva, Switzerland, Nov. 2022.

[25] A. Gonzalez, K. Fukushima, T. Maruta, P. N. Ostroumov, and A. Plastun, "Multi-q beam studies at FRIB: simulations and measurements," in *Proc. HIAT '25*, 2025. [Abstract].

[26] K. L. Brown, "A First and Second Order Matrix Theory for the Design of Beam Transport Systems and Charged Particle Spectrometers," *Adv. Part. Phys.*, vol. 1, pp. 71–134, 1968.

[27] K. L. Brown, F. Rothacker, D. C. Carey, and F. C. Iselin, "Transport: A Computer Program for Designing Charged Particle Beam Transport Systems," 1983.

[28] A. Septier and H. Enge, *Focusing of Charged Particle Beams*, ch. 4.2, pp. 203–265. Academic Press, 1967.

[29] P. N. Ostroumov, V. N. Aseev, and B. Mustapha, "Beam loss studies in high-intensity heavy-ion linacs," *Phys. Rev. Accel. Beams*, vol. 7, 2004.

[30] D. Gorelov and F. Marti, "Ion charge stripper foil model for beam dynamics simulation," in *Proc. Linac 2006*, 2006.

[31] P. N. Ostroumov, A. S. Plastun, N. Bultman, D. Morris, X. Rao, Q. Zhao, and S. Zhao, "Efficient continuous wave accelerating structure for ion beams," *Phys. Rev. Accel. Beams*, vol. 23, 2020.

[32] P. N. Ostroumov, K. Fukushima, A. Gonzalez, K. Hwang, T. Kanemura, T. Maruta, A. Plastun, J. Wei, T. Zhang, and Q. Zhao, "FRIB from commissioning to operation," in *Proc. HB '23*, 2023.

[33] A. Gonzalez, A. Plastun, P. N. Ostroumov, and X. Rao, "Suppression of high-intensity stripped heavy-ion beam losses," *Physical Review Accelerators and Beams*, 2025. Submitted.

[34] A. Gonzalez, A. Plastun, and P. N. Ostroumov, "Mitigation of longitudinal beam losses in the FRIB linac," in *Proc. LINAC '24*, 2024.

[35] “CST Studio Suite.” `https://www.3ds.com/products-services/simulia/products/cst-studio-suite/`.

[36] M. Bres, A. Chabert, F. Foret, D. T. Trant, and G. Voisin, “The interdigital H-type (IH) structure, an accelerating structure for low energy beams,” *Part. Accel.*, vol. 2, 1971.

[37] A. C. C. Villari, B. Arend, G. Bollen, D. B. Crisp, K. D. Davidson, K. Fukushima, A. I. Henriques, K. Holland, S.-H. Kim, A. Lapierre, *et al.*, “Upgrade of the FRIB ReAccelerator,” in *Proc. NAPAC ’22*, 2022.

[38] N. J. Simon, E. S. Drexler, and R. P. Reed, *Properties of Copper and Copper Alloys at Cryogenic Temperatures*. National Insititute of Standards and Technology, 1992.

[39] L. Doolittle, M. Placidi, P. Emma, A. Ratti, S. U. De Silva, R. G. Olave, and J. R. Delayen, “Cascading RF deflectors in compact beam spreader schemes,” *Nucl. Instrum. Methods Phys. Res. A*, vol. 899, pp. 32–42, 2018.

[40] A. C. Araujo Martinez, R. Agustsson, Y. Chen, S. V. Kutsaev, A. Plastun, and X. Rao, “Electromagnetic Design of a Compact RF Chopper for Heavy-Ion Beam Separation at FRIB,” in *Proc. NAPAC ’22*, 2022.

[41] A. S. Plastun and P. N. Ostroumov, “Linear Accelerator for a Next Generation Rare Isotope Facility,” in *Proc. 13th International Particle Accelerator Conf. (IPAC ’23)*, 2023.

[42] C. Hovater, G. Arnold, J. Fugitt, L. Harwood, R. Kazimi, G. Lahti, J. Mammosser, R. Nelson, C. Piller, and L. Turlington, “The CEBAF RF Separator System,” in *Proc. LINAC ’96*, 1996.

[43] A. Gonzalez, A. Plastun, and P. N. Ostroumov, “Rf chopper for prebunched radioactive ion beams,” *Physical Review Accelerators and Beams*, vol. 27, 2024.

[44] A. Gonzalez and A. Plastun, “Rf chopper for prebunched radioactive ion beams,” in *Proc. HIAT ’22*, 2022.

[45] Y. Senichev, O. Belyaev, W. Brautigam, Y. Budanov, R. Maier, V. Stepanov, V. Teplyakov, A. Zherebtsov, and Z. I., “Novel H-type rf deflector,” *Physical Review Special Topics-Accelerators and Beams*, vol. 9.1, p. 012001, 2006.

[46] E. Pozdeyev, N. Bultman, G. Machicoane, G. Morgan, X. Rao, and Q. Zhao, “FRIB Front End Design Status,” in *Proceedings of LINAC 2012, Tel Aviv, Israel*, 2012.

[47] E. W. Blackmore, “An RF Separator for Cloud Muons at TRIUMF,” *Nucl. Instrum. Methods Phys. Res. A*, vol. 234.2, pp. 235–243, 1985.

[48] K. Bongardt, “Funneling of Heavy Ion Beams,” in *Proceedings of the 1981 Linear Accelerator Conference*, 1981.

[49] D. Leitner, D. Alt, T. M. Baumann, C. Benatti, K. Cooper, B. Durickovich, K. Kittimanapun, S. Krause, A. Lapierre, L. Ling-Ying, *et al.*, “Status of the Rare Isotope ReAccelerator Facility ReA,” in *Proceedings of PAC2013, Pasadena, CA, USA*, 2013.

[50] S. V. Badea, N. Tsoupas, J. Tuozzolo, and A. J., “Building a Family of Corrector Magnets for SNS Facility,” in *Proc. of the 2003 Particle Accelerator Conference*, 2003.